High-performance liquid chromatography with packed microchips

Dissertation

zur
Erlangung des Doktorgrades
der Naturwissenschaften

(Dr. rer. nat.)

dem

Fachbereich Chemie
der Philipps-Universität Marburg

vorgelegt von

Steffen Ehlert

aus Magdeburg (SACHSEN-ANHALT)

Marburg/Lahn, September 2010

Die vorliegende Dissertation wurde in der Zeit von Januar 2006 bis September 2010 am Institut für Verfahrenstechnik der Otto-von-Guericke Universität Magdeburg und am Fachbereich Chemie der Philipps-Universität Marburg unter der Leitung von Herrn Prof. Dr. Ulrich Tallarek angefertigt.

Vom Fachbereich Chemie
der Philipps-Universität Marburg als Dissertation am 12.10.2010
angenommen

Erstgutachter: Prof. Dr. U. Tallarek
Zweitgutachter: Prof. Dr. A. Seubert

Tag der mündlichen Verteidigung: 12.11.2010

Acknowledgement

I would like to thank Prof. Dr. Ulrich Tallarek for the great opportunity to prepare this work under his supervision. His mentorship was paramount in providing a well rounded experience consistent with my long-term career goals. He encouraged me to not only grow as an experimentalist and an analytical chemist but also as an instructor and an independent scientist.

I want to thank Prof. Dr. Andreas Seubert for the acceptance of revision of this thesis.

I would like to thank the members of the examining committee for the evaluation of my thesis.

I want to express my gratitude to Dr. Monika Dittmann from Agilent Technologies (Waldbronn, Germany) for the supervision of my thesis and all projects included, and all colleagues that accompanied my work over the last 4 years, especially Jose-Angel Mora and Karsten Kraiczek who were providing me with numerous chips.

I want express my deepest appreciation to Dr. Alexandra Höltzel who was an indispensable help during the preparation of the published manuscripts.

I am also indebted to my colleges of the Group of Prof. Tallarek for the fruitful discussions and for providing an excellent working atmosphere.

I want to dedicate a special thanks to my girlfriend, brother and parents in having supported me over the past years.

Zusammenfassung

Die Arbeit beschäftigt sich mit dem Einfluss der Packungsporosität zylindrischer Kapillaren und nicht-zylindrischen Kanalgeometrien von Mikrochips auf die Trenneffizienz. Die Reduzierung der Peakdispersion einhergehend mit einer Verbesserung der chromatographischen Trenneffizienz ist das größte Problem was bei Mikro- und Nanotrennsystemen gelöst werden muss, damit alle positiven Einträge die durch die Miniaturisierung erreicht werden auch vollständig ausgenutzt werden können. Hierzu wurden zylindrische Kapillaren mit einem Durchmesser von 30 bis 250 µm mit 5 µm Partikeln gepackt und diese hinsichtlich ihrer Porosität in Abhängigkeit von der Kanalquerschnittsfläche bei konstantem Partikeldurchmesser untersucht (*Kapitel 2*). Zusätzlich wurden zwei individuelle Messmethoden evaluiert die erste basierend auf der inversen Grössenausschlusschromatographie und die zweite auf der Donnan-Ausschluss-Chromatographie, die es ermöglichten die Porosität der gepackten Strukturen sicher zu bestimmen (*Kapitel 3*). *Kapitel 4* beschäftigt sich mit der Weiterentwicklung eines HPLC (high performance liquid chromatography) Mikrochips von Agilent Technologies (Waldbronn, Germany). Hierzu wurden systematische Studien der Trenneffizienz in Abhängigkeit von der Porosität der nicht-zylindrichen Kanalgeometrie der Chips erstellt und mittels UV-Detektion vermessen. Dazu wurden verschiedene Packprozesse evaluiert (Variation der Packdrücke und die Implementierung von Ultraschall in den Packprozess) und die sich daraus ergebenden Packungsporositäten und Trennleistungen unter isokratischen Bedingungen untersucht. Die Daten zeigten klar, dass sich mit optimierter Packungsporosität die isokratischen Trennleistungen durch die optimierten Dispersions- und Massentransfereigenschaften der gepackten nicht-zylindrischen Trennkanäle deutlich erhöhen ließen. In *Kapitel 5* wurden die Ergebnisse der Untersuchungen aus *Kapitel 4* auf die kommerziell erhältlichen HPLC/MS-Chips übertragen und unter isokratischen Bedingungen evaluiert und verglichen. Wie nicht anders zu erwarten, konnte eine sehr hohe Übereinstimmung der Trenneffizienzen in Abhängigkeit von der Packungsporosität zwischen den beiden Systemen (HPLC/UV und HPLC/MS-Chips) festgestellt werden. *Kapitel 5 und 6* beschäftigen sich mit der Evaluierung der Trenneffizienzsteigerung unter Gradientenelutionsbedingungen. Dafür wurden kleine pharmazeutische Moleküle und etwas komplexere biologische Proben (BSA und Cohn Fraktion IV-4) chromatographisch vermessen. Die Daten zeigten, dass selbst unter der Verwendung von steilen Gradienten sich die Trenneffizienz deutlich erhöhte, einhergehend mit einer gesteigerten Peptididentifikationsrate und Peakkapazität für die untersuchten Analytzusammensetzungen. Dieses liegt begründet in den reduzierten

Dispersionseigenschaften der optimiert gepackten Festbetten, die zu deutlich schmäleren Peaks (reduzierte Peakbreiten) führte.

Die Arbeit zeigt im Detail in Kapitel 2 *(Packing density of slurry-packed capillaries at low aspect ratios)* den Einfluss des geometrischen Wandeffektes in polyimid-ummantelte Glaskapillaren (fused silica) in Abhängigkeit vom Partikeldurchmesser (d_P) zu Säulenquerschnitt (d_C) Verhältnis von $5 < d_C/d_P < 50$. Hierzu wurden die Kapillaren (30 µm - 250 µm Durchmesser) mittels einer Suspension aus chromatographischem Packmaterial (5 µm Partikel) gepackt und hinsichtlich ihrer Porosität des generierten Packungsbettes untersucht. Die Bestimmung der Packungsdichten beruhte dabei auf dem Größenausschluss von Polystyrolstandards definierter Masse, die sich im verwendeten Laufmittel Dichlormethan in Abhängigkeit ihrer Molmasse zu definierten Kugeln knäulen und somit vom intrapartikulären Porenraum der Packungsmaterialien sterisch ausgeschlossen werden [1, 2]. Die Elutionszeit der ausgeschlossenen Polystyrole kann somit zur Bestimmung des sogenannten Zwischenkornvolumen oder auch interpartikulären Porosität (ε_{inter}) herangezogen werden. Zunächst konnte festgestellt werden, dass die intrapartikuläre Porosität (ε_{intra}) der Partikel erwatungsgemäß unabhängig vom d_C/d_P-Verhältnis ist ($\varepsilon_{intra} \approx 0{,}29$), da die Porosität der Partikel als unabhängige konstante Größe angenommen werden konnten. Im Gegensatz dazu nahmen die Packungsporositäten von $\varepsilon_{inter} \approx 0{,}47$ bei $d_C/d_P = 5$ bis hin zu $\varepsilon_{inter} = 0{,}36\text{-}0{,}37$ bei $d_C/d_P = 40\text{-}50$ ab. Die systematische Zunahme von ε_{inter} und ε_{total} (totale Porosität) mit abnehmendem Säulendurchmesser, also mit abnehmendem d_C/d_P-Verhältnis, ist abhängig vom geometrischen Wandeffekt, der die realisierbaren Porositäten stark beeinflusst. An der starren Wandregion kann nur eine sehr viel höhere Porosität erzielt werden (direkt an der Wand ist die Porosität 1). Die Anordnung der Partikel und die sich daraus ableitende ortsgebundene Porosität verteilt sich statistisch in einer gedämpften Schwingung über einen Bereich von 4-5 Partikeldurchmessern bis hin zu einer zufälligen (random) Anordnung in der Mitte des Kanalquerschnittes, wenn diese Region überhaupt erreicht wird. Es ist daher nicht verwunderlich, dass bei sehr kleinen Kanalquerschnitten und daraus resultierenden geringen d_C/d_P-Verhältnissen der Einfluss der höheren Porosität in der Wandregion auf die Porosität über gesamten Kanalquerschnitt steigt. Dieses Zusammenspiel zwischen Wand- und Kernregion ist entscheidend für die Homogenität der Verteilung einer Packungsstruktur über den Kanalquerschnitt. Es sollte das d_C/d_P-Verhältnis entweder so groß gewählt werden, dass der relative Einfluss der Wandregion zurückgedrängt wird, oder so klein das er vorherrschend ist. Es ist daher nicht verwunderlich, das in den Arbeiten von Jorgenson [3, 4] die Trenneffizienz der 5 µm Partikel basierten Packungen bei einer Reduzierung des Kanalquerschnitts von 50 auf 12 µm ansteigt. Bei so kleinen d_C/d_P-Verhältnissen dominiert die „lose“ gepackte Wandregion, was aber zu einer effektiv höheren

Homogenität der Packung führt und somit das dispersive Verhalten der Analyten innerhalb der Packungsstruktur angleicht (homogenisiert).

Kapitel 3 *(Determination of the interparticle void volume in packed beds via intraparticle Donnan exclusion)* stellt einen sehr einfachen und vertrauenswürdigen Alternativansatz zur inversen Größenausschlusschromatographie (ISEC) zur Bestimmung der Packungsporositäten in zylindrischen Kapillaren vor. Basierend auf dem elektrostatischen Ausschluss (Donnan-Ausschluss) eines geladenen (nicht retardierenden) Analyten (Nitrat-Ionen) ist es möglich das interpartikuläre Volumen (V_{inter}) und somit die interpartikulare Porosität (ε_{inter}) zu bestimmen. Dazu wurden Kapillaren mit einem Durchmesser von 75 µm mit verschiedenen Partikelgrößen, Porengrößen und unterschiedlichen Oberflächenmodifikationen in Abhängigkeit der Pufferzusammensetzung (Tris-HCl-Puffer) evaluiert. Die Theorie des elektrostatischen Ausschlusses liefert eine klare und eindeutige Abgrenzung der Grenzflächenphänomene der ladungsselektiven Mesoporen (Porenraum innerhalb der Partikel) und der nicht-ladungsselektiven Makroporen (Porenraum zwischen den Partikeln). Dieser Ansatz erlaubt es den Donnan-Ausschluss geladener Analyten in Abhängigkeit der etablierten elektrischen Doppelschichtüberlappung (EDL overlap) unter den gegebenen physikalischen Bedingungen (Porengröße, Partikeldurchmesser und Pufferstärke) zu etablieren. Die dabei bestimmten Porositäten stimmten sehr gut mit den durch die ISEC-Methode erzielten überein. Die Limitierungen der beiden Methoden (ISEC-und Donnan-Ausschluss) basieren auf denselben Bedingungen. Sind die Partikel zu klein (< 3 µm), kann es zu einem Größenausschluss der Polystyrole vom Außenraum kommen, genau wie es zu einem elektrostatischen Ausschluss der Nitrat-Ionen kommen kann, wenn die Doppelschichtdicken sich zwischen den Partikeln zu überlappen beginnen. Zudem ist es schwierig die Ausschlussbedingungen für sehr große Porengrößen (1000 Å) zu erzielen, da unter diesen Bedingungen die Polystyrole so groß und die Pufferstärken so niedrig gewählt werden müssen, dass es auch zu einem zwischenpartikulären Ausschluss der Analyten kommen kann und somit eine genaue Bestimmung der Porosität nicht ohne weiteres möglich ist.

Basierend auf den Untersuchungen die mit Hilfe der zylindrischen Glaskapillaren ausgearbeitet wurden (*Kapitel 2 und 3*), bestand die Hauptaufgabe der Arbeit darin, den Einfluss der Packungsporosität des HPLC-Chips Systems von Agilent Technologies (Waldbronn, Germany), das eine nicht-zylindrische Kanalgeometrie (trapezförmig) aufwies, in Abhängigkeit des Packprozesses zu untersuchen (*Kapitel 4 - Separation Efficiency of Particle-Packed HPLC-Microchips*). Simulationen in unserer Gruppe haben deutlich gezeigt, dass die dispersiven Eigenschaften eines Analyten und die daraus resultierenden Trenneffizienzen stark von der Porosität und der Kanalgeometrie abhängen [5]. Diese Arbeiten zeigen, dass mit abnehmender Symmetrie der Kanalquerschnittsfläche (Zylinder →

Quadrat → Rechteck → Halbkreis) und hohen Packungsporositäten (ε_{inter} = 0,48) der Einfluss der „Ecken“ auf die Homogenität des Flussfeldes der mobilen Phase (und somit auch der sich darin befindlichen Analyten) abnimmt. Dies geht einher mit der Zunahme der Dispersion und einer reduzierten Trenneffizienz. Ist es jedoch möglich, die nicht-zylindrichen Kanalgeometrien effektiv und dicht zu Packen (vor allem die „Ecken“), reduziert sich der zusätzlich dispersive Eintrag dieser, bis hin zu äquivalenten dispersiven Eigenschaften zwischen zylindrischen und nicht-zylindrischen Trennkanälen. Somit ist eine annähernd gleiche Trenneffizienz zwischen den verschiedenen Kanalgeometrien realisierbar, wenn die interpartikuläre Porosität hin zu optimieren Packungsstrukturen reduziert werden kann ($\varepsilon_{inter} \leq$ 0,40).

Zur Bestimmung der Packungsdichten musste jedoch zuerst ein Prototyp HPLC-Chips Design entwickelt werden, da die zur Bestimmung der Packungsporositäten verwendete ISEC-Methode auf die kommerziell erhältlichen HPLC/MS-Chips nicht anwendbar war (*Kapitel 4*). Hierzu wurde ein Chip neu erstellt, der eine on-Chip UV Detektion ermöglichte, um die UV-aktiven Polystyrole als auch die zur Trenneffizienz verwendeten Analyten untersuchen und detektieren zu können. Beide Chipsysteme wiesen eine hohe Übereinstimmung im Verhältnis zwischen Trennkanalvolumen zu on-Chip Totvolumen auf (110 für den HPLC/UV Chip und 150 für den HPLC/MS Chip), was einen späteren Vergleich der Trenneffizienzen erst ermöglichte.

Im Einzelnen ist in *Kapitel 4* beschrieben, dass die Packungsporosität für die HPLC/UV Chips mit zunehmendem Packdruck und der Implementierung von Ultraschall in den Packprozess systematisch reduziert werden kann. Dazu wurden folgende Packzyklen miteinander Verglichen: 150 bar ohne Ultraschall, 150 bar mit Ultraschall, 300 bar ohne Ultraschall und 300 bar mit Ultraschall. In Abhängigkeit der applizierten Packprozesse konnte eine stetige Abnahme der Porositäten von ε_{inter} = 0,475, ε_{inter} = 0,46, ε_{inter} = 0,45, bis hin zu ε_{inter} = 0,42 beobachtet werden. Die erzielen Porositäten für den Packprozess mit 300 bar und Ultraschall waren vergleichbar zu denen, die mit kommerziell erhältlichen zylindrischen Glaskapillaren mit vergleichbaren Kanalquerschnitt und den gleichen Packungsmaterialen (ε_{inter} = 0,42) erhalten wurden. Wie nicht anders zu erwarten, wurden die chromatographischen Trenneffizienzen mit abnehmender Porosität verbessert. Dies zeigte sich in der Darstellung von Bodenhöhenkurven die mit den einzelnen Chips vermessen wurden. Mit abnehmender Porosität reduzierten sich die zusätzlichen dispersiven Einträge innerhalb des Trennkanals und die generierten Packungen waren homogener. Die Mimima der Bodenhöhenkurven wurden zu höheren linearen Geschwindigkeiten verschoben und der Anstieg vor allem im C-Term wurde deutlich reduziert [6]. Dies bedeutet, dass der Massentransferwiderstand deutlich reduziert werden konnte auf Grund der Reduzierung des Einflusses des geometrischen Wandeffektes, einhergehend mit dem Zurückdrängen des

dispersiven Eintrages der „Ecken“ durch eine dichtere Packung der nicht-zylindrischen Kanalgeometrie.

Für den abschließenden Vergleich der Ergebnisse, die mit den HPLC/UV Chips erzielt werden konnten, wurden die kommerziellen HPLC/MS-Chips mit den gleichen Packprozessen gepackt und hinsichtlich ihrer Trenneigenschaften unter isokratischen und Gradientenelutionsbedingungen evaluiert (*Kapitel 5 - Performance of HPLC/MS microchips in isocratic and gradient elution modes*). Hierzu wurden basierend auf den Permeabilitätsdaten der HPLC/UV Chips die Porositäten der HPLC/MS Chips abgeschätzt (basierend auf deren Permeabilitäten). Es war festzustellen, dass die HPLC/MS Chips noch einmal eine etwas geringere Porosität innerhalb der Trennkanäle aufwiesen (5 µm Partikel, 150 bar ohne Ultraschall, $\varepsilon_{inter} \approx 0{,}46$; 5 µm Partikel, 300 bar und Ultraschall, $\varepsilon_{inter} \approx 0{,}41$; und für 3.5 µm Partikel 300 bar und Ultraschall, $\varepsilon_{inter} \approx 0{,}39$). Dieses lag darin begründet, dass die Trennkanäle der HPLC/MS Chips mit 43 mm etwas kürzer waren als die der HPLC/UV Chips (73 mm) und somit bei gleichem applizierten Druck während des Packprozesses, sich ein steilerer Druckgradient über die Kanallänge etablierte, der die kürzere Kanalstrecke begünstigte. Es war jedoch festzustellen, dass die HPLC/MS Chips bei niedrigen Retentionsfaktoren (k’) der Analyten trotzdem eine schlechtere Trennleistung aufwiesen. Diese konnte darauf zurückgeführt werden, dass es bei den MS Chips, operativ bedingt (auf Grund der MS-Detektion), zusätzliche externe Volumenbeiträge (externe Banden-verbreiterungsbeiträge) durch die Überführung der ionisierten Analyten in das Massenspektrometer gab. Um diesen absoluten Beitrag zur Bandenverbreiterung zu minimieren, wurden die Analysen bei sehr hohen k’-Werten durchgeführt, da dort der relative Beitrag zur Gesamtdispersion vernachlässigt werden kann [7]. Daher wurde der Vergleich der Trenneffizienzen der beiden Chipsysteme bei k’ = 35 (UV) und k’ = 28 durchgeführt. Der Unterschied in den Retentionsfaktoren, trotz gleicher Laufmittelzusammensetzung (50/50 Acetonitril/Wasser (v/v)), beruhte auf den unterschiedlichen Temperaturen während der Messungen (298 K ± 1 UV; Raumtemperatur und 313 K ± 1 MS; Temperatur im MS-System). Die höheren Temperaturen während der massenspektrometrischen Untersuchungen reduzieren die Viskosität und Dichte des Laufmittels und sorgen zusätzlich für einen erhöhten Massentransfer der Analyten im Trennkanal, was Retentionsverhalten der zu trennenden Substanzen beeinflusst und zu geringeren Retentionsfaktoren führt [7]. Die erzielten reduzierten minimalen Bodenhöhen (h_{min}) für die optimierten Packungsbetten der HPLC/UV Chips lagen somit bei $h_{min} = 2{,}5$ und für die HPLC/MS Chips bei $h_{min} = 2{,}1$. Diese Werte zeigten deutlich die Konkurrenzfähigkeit der optimierten Packungsstrukturen des HPLC/MS Chipsystems im Vergleich zu anderen kommerziell erhältlichen nano-Säulen.

Der Trend der erhöhten Trenneffizienzen in Abhängigkeit der Packungsstruktur wurde dann in der Anwendung mittels kleiner pharmazeutischer und komplexer biologischer

Analyten vervollständigt (*Kapitel 5 - Performance of HPLC/MS microchips in isocratic and gradient elution modes*). Dazu wurden 11 pharmazeutische Analyten mit den HPLC/MS Chips untersucht unter Verwendung verschiedener Gradientensteilheiten. Dabei beschränkte sich die Evaluierung der Effekte auf die Chips gepackt mit 5 µm 150 bar ohne Ultraschall, 5 µm 300 bar mit Ultraschall und 3,5 µm 300 bar und Ultraschall. Hierbei war deutlich festzustellen, relativ unabhängig vom verwendeten Gradienten, dass sich die Peakbreiten um ~ 15% verringerten und die Auflösung der Peaks um ~ 20% erhöht wurde, wenn man die beiden 5 µm Festbetten miteinander verglich. Dieselbe Peakbreitenverbesserung (~ 15%) und Auflösungserhöhung (~ 20%) war festzustellen zwischen den optimierten 5 µm und den optimierten 3,5 µm Packungsstrukturen. Diese Daten korrespondierten in sehr guter Übereinstimmung mit den bereits evaluierten isokratischen Messungen aus Kapitel 4.

In Kapitel 6 (*Improved particle-packed HPLC/MS microchips for proteomic analysis*) wurden abschließend ein tryptischer Verdau des wenig komplexen BSA und der hoch komplexen Cohn4-IV-Fraktion in die Bestimmung der chromatographischen Trenneffizienzen integriert. Hier zeigten sich vier deutliche Trends: 1. Die Reproduzierbarkeit der Messungen gerade bei sehr niedrigen injizierten Konzentrationen verbesserte sich mit zunehmender Packungsqualität, was eine Anwendung der Chips für Langzeitstabilitätsuntersuchungen begünstigt. 2. Es war möglich, die Nachweisgrenze hin zu geringeren Konzentrationen zu verschieben, was eine Anwendung in der Spurenanalytik weiter bevorteilt, und 3. war es möglich, die Identifikationsrate von Peptiden mit der Cohn-Fraktion mit verbesserter Packungsqualität zu erhöhen. So konnten mit der nicht optimierten 5 µm Packung nur 126, mit der optimierten 5 µm Packung 143 und mit der optimierten 3,5 µm sogar 175 Peptide identifiziert werden. Dies bedeutete einen Identifikationsgewinn in einem chromatographischen Lauf von fast 40%. Durch die verbesserten Peakbreiten und Auflösungen war es möglich, mehr diskret von einander getrennte Peaks in das MS zu überführen, was die Ionenverdrängung (ion suppression) herabsetzte. 4. Es konnten auch die Peakkapazitäten mit abnehmender Packungsporosität deutlich erhöht werden. Im Einzelnen konnten Verbesserungen der Peakkapazitäten für den BSA-Verdau von ca. 40% für die optimierten 5 µm (300 bar und Ultraschall) und zwischen 76-94% für die Packungen mit 3,5 µm (300 bar und Ultraschall) erzielt werden im Vergleich mit den 5 µm Packungsstrukturen die mit 150 bar ohne Ultraschall generiert wurden. Diesbezüglich wurden für den Cohn-Verdau eine Erhöhung der Peakkapazitäten von 58% und 94% im Vergleich erreicht.

Zusammenfassend kann man sagen, dass es von äußerster Wichtigkeit ist, mikrofluidische Trennsysteme mit einer effizienten und niedrigen Packungsporosität auszustatten. Dazu ist es wichtig, die Packprozesse für die Trennkanäle zu optimieren, was sowohl die Applikation von hohem Druck als auch Ultraschall während der

Packungsgenerierung beinhaltet. Nur so ist es möglich, effiziente chromatographische Trennungen durchzuführen und das Potenzial der Miniaturisierung und der damit einhergehenden Minimierung externer Bandenverbreiterungsbeiträge auch wirksam auszunutzen. Diese Verbesserungen führen gerade bei denen in der pharmazeutischen Industrie häufig angewendeten Gradientenelutionen zu einem Identifikationsgewinn vor allem bei komplexen Probenmatrizes, einer verbesserten Langzeitstabilität und zu einer hoch effizienten Trennung von kleinen und komplexen Analysenmolekülen. Es ist möglich auf mikrofluiden Trennsystemen Packungsporositäten zu erreichen die vergleichbar mit denen der weitverbreiteten zylindrischen Kapillaren sind. Grundvoraussetzung hierfür ist jedoch, dass die miniaturisierten Trennsysteme ausreichend druckstabil sind, um den erforderlichen Drücken und der Applikation von Ultraschall während des Packprozesses und den Drücken im Betrieb stand halten zu können. Gerade die Verwendung von Ultraschall ist bei geringen Säulenquerschnittsflächen-zu-Partikeldurchmesser-Verhältnissen essenziell, um eine hohe Packungsdichte und somit eine effiziente Trennung zu erreichen. Das als Basis nehmend, kann der Effekt der Miniaturisierung und Integration der Chromatographie auf ein einzelnes Gerät (miniaturisierte Gesamtanalysensysteme; μTAS) mit allen seinen Vorteilen hinsichtlich der Reduzierung von Analytkonzentrationen, Dispersion und Wegstrecken der Analyten durch das System voll zum tragen kommen und verspricht die best mögliche Trennleistung in der Chromatographie im Nanomaßstab.

Literatur

[1] Ehlert, S.; Rösler, T.; Tallarek U. *J. Sep. Sci.* **2008,** *31,* 1719-1728.

[2] Halász, I.; Martin, K. *Angew Chem. Int. Ed.* **1978**, *17,* 901-908.

[3] Kennedy, R. T.; Jorgenson, J. W. *Anal. Chem.* **1989**, *61,* 1128-1135.

[4] Hsieh, S.; Jorgenson, J.W. *Anal. Chem.* **1996***, 68,* 1212-1217.

[5] Khirevich, S.; Höltzel, A.; Hlushkou, D.; Tallarek, U., *Anal. Chem.* **2007**, *79*, 9340-9349.

[6] Ehlert, S.; Kraiczek, K.; Mora, J.-A.; Dittmann, M.; Rozing, G. P.; Tallarek, U. *Anal. Chem.* **2008**, *80*, 5945-5950.

[7] Guiochon, G. *J. Chromatogr. A* **2006**, *1126,* 6-49.

Introduction

In the beginning of the 20th century, chemistry was an established and growing science. The synthesis of organic molecules, like pharmaceutical drugs, fertilizer and pigments was of growing interest in the economic system. The separation and purification of synthetical and natural products was usually done by means of recrystallization, extraction and distillation. But these techniques were time consuming and expensive, because they had to be repeated several times to achieve adequate pure products. The development of liquid chromatographic techniques was highly beneficial to the application of a multitude of separation and purification problems.

The chromatography is based on the separation of different analytes due to their differential affinity to the fixed stationary and moving mobile phase. Tswett invented chromatography many years ago [1, 2]. For this purpose, he packed long tubes with ~ 50 µm particles of a porous adsorbent, making the first chromatographic columns. He separated the dyes of plant extracts by injecting the solved analytes to a glass tube packed with fine powdery calcium carbonate. This basic approach of a packed cylindrical column with a liquid mobile phase as carrier was further developed in the following. The application of porous particles is favored over these of non-porous packing materials, due to the increased surface of the stationary phase and therefore the enhanced separation efficiency. The development of many different surface modified stationary phases (e.g., C8, C18 or SO_3^- chemically bonded onto silica based porous packing materials) enhanced the application possibilities due to the increased requirements of more complex and challenging separations needed in chemistry. Tswett also recognized that better results were obtained with finer particles or in other words by reducing the particle diameters. However, the lack of suitable pumps permitting the percolation of the mobile phase through the column at a sufficiently large flow rate and the availability of very small particle commonly used today (< 5 µm) limited the performance of the method.

Remarkable progress was made in the second part of the last century, leading to the development of chromatographic implementations known as high pressure or high performance liquid chromatography (HPLC). Pressurization of the liquid phase and control of its flow rate accompanied by the effort toward the use of finer particles and with the development of on-line detection using a variety of principles were the main features of this new approach [3–6]. In spite of this progress, the separation efficiency of current HPLC columns appears insufficient for the solution of important analytical problems. Because most of the important modern separation problems cannot be solved by gas chromatography due to insufficient volatility of the sample components, it is becoming critical to push column liquid

chromatography to its limits. The performance can be improved in four different ways: The designing and building of more efficient columns by increasing their lengths [8], decreasing the particle diameter [9], replacing their packed beds by suitable monolithic beds [10, 11] and miniaturization of the separation conduit and the integration to micro total analyzing systems (μTAS) to avoid unmeant external band broadening that is degrading the separation efficiency. Hence, the implementation of gradient elution techniques instead of isocratic elution modes improved the separation and economic efficiency by decreasing the separation times and enhancement of the resolution [12-14].

The miniaturization of HPLC concerning the column inner diameter (i.d.) and volumetric flow rates is an ongoing trend that is mainly driven by the need to handle small volumes of complex sample, e.g., for the elucidation of physiological processes and identification of successful drug candidates, particularly in the context of high throughput screening technologies. While typical dimensions in narrow-bore and analytical LC include 2.1- to 4.6-mm-i.d. columns and packed beds of 3 to 10 μm-sized spherical porous particles, the further miniaturization towards nano-LC with a column i.d. of < 150 μm, sub-microliter flow rates, and sample loadings of < 1 μg offers many advantages. (1) It is increasing mass sensitivity (in combination with concentration-sensitive detection) owing to a reduced chromatographic dilution. (2) The use of smaller particle sizes (< 3 μm) for the preparation of packed beds (at a constant average flow velocity) is reducing intraparticle stagnant mobile phase mass transfer resistance and therefore increasing the chromatographic efficiency. (3) The reduction of stationary phase, solvent, and sample volume consumption which facilitates the use of exotic liquids, expensive adsorbents, and/or long columns (if pressure drop is not a limiting factor), and (4) the compatibility with flow rate requirements of a nanoelectrospray interface for on-line coupling to mass spectrometry (MS) are also very beneficial. In fact, the development of nano-LC has been driven in part by the need for high-sensitivity LC-MS/MS analyses. Today, the use of 75 μm i.d. packed capillaries and 200 nL/min flow rates is typical for many applications.

Lab-on-a-chip devices, as investigated in this work, offer attractive features such as the fabrication of highly multiplexed systems with zero-dead volume interconnections, automation, and amenability to mass production. For example, some bottlenecks in high throughput screening are the serial configuration of current two-dimensional LC-MS systems and the often tedious sample preparation. Compared to electrokinetic techniques, LC-based separations are more robust and reproducible, while the wealth of stationary phase chemistries provides great flexibility. By realizing high-pressure LC in microchip format, more sophisticated low-volume analyses become possible, because a variety of chip morphologies can be designed to enable chemical reaction, mixing, and multidimensional separations. Recent progress towards high-pressure LC in lab-on-a-chip devices includes the integration

of individual operations (e.g., reaction, pre-concentration, and separation) in mass-produced, low-cost devices; automation; the reproducible preparation of packed beds and monoliths as stationary adsorbent phase in small noncylindrical channels; and high pressure actuation and sample injection [13–24]. Performance and challenges in microchip-LC are investigated with respect to band broadening, gradient elution, and packing microstructure, to ensure the possible comparability and replaceability of existing standard application in the LC.

While performance, integration, and automation make microchip-LC easier to use, more robust and reliable compared to nano-LC, a problem in high-throughput screening with gradient elution remains the gradient cycle time. Commercial pumping systems can generate accurate solvent gradients, but the systems are still enormous in terms of size relative to the generated flow rates [25]. For example, it typically takes around 15 min between the gradient formation and arrival at the end of a column. Thus, more attention should be given to the minimization of external volumes and delay times arising from mobile phase transfer and mixing. Compared to conventional nano-LC the chromatographic resolution with microfabricated devices is nearly as good, but the total cycle time can be significantly reduced to a several second gradient delays [15]. Although those devices still face several problems, e.g., short chromatographic beds, low operating pressures and flow rates (< 100 nl/min), they reveal the existence of massive space for improvement in gradient elution high-throughput screening by reducing the volume between liquid mixing and sample separation.

An important factor for chromatographic performance in microchip-LC that may be easily overlooked while focusing on process miniaturization, integration, and automation is the preparation of high-surface-area fixed beds in typical chip channels with, e.g., half-spherical, rectangular, or trapezoidal cross-section [17, 20, 22, 23, 26]. The inherent, but unfamiliar noncylindrical shapes require a closer look at engineering chromatographic beds in microchip format. While a significant impact of the channel geometry on solute dispersion in pressure-driven microfluidic systems is well documented [27], only little is known about flow nonuniformity and the associated dispersion in packed beds depending on the geometry of the confining channel [26]. This is further complicated by the fact that the aspect ratio of channel to adsorbent particle size in microchip-LC becomes very low compared to narrow-bore and analytical LC columns. For example, packing spheres against a hard wall results in systematic fluctuations of the interparticle porosity in the immediate vicinity to the wall, starting with a maximum value of unity, followed by a damped oscillation (being influenced by the particle size distribution) with a period close to a sphere diameter over a distance of 4–5 particles towards the center of the packing [28]. This purely geometrical wall effect originates in a decrease of packing order as the distance from the wall increases and is inherently present in packed beds. However, while it becomes unimportant for the relatively high aspect

ratios (column-to-particle diameter ratios) encountered, in narrow-bore LC, it gains strong impact on macroscopic flow heterogeneity and axial dispersion at low aspect ratios (below 50) when this critical wall region occupies a substantial volumetric fraction of the packing [29]. This addresses packed beds currently employed in microchip-LC where about 10 particle diameters over at least one channel dimension are common and is further complicated by the corners in noncylindrical chip channels compared to the classical cylinder format. Monoliths are certainly an attractive alternative with respect to analysis speed, separation efficiency, and adsorption capacity [30], but in any case it remains of utmost importance to pack/fill sufficiently well the corners introduced by microchip channels with a symmetry lower than that of the traditional cylindrical columns to keep additional flow heterogeneity and band spreading relatively small. However, for monoliths it is still challenging to attach them sufficiently to the wall without generating gaps which would cause an inhomogeneous flow distribution transcolumn velocity bias.

Indeed, high-pressure microchip-LC has the potential to become a more powerful tool than nano-LC for analyzing complex samples (e.g., in proteomes), mainly due to improved efficiency (e.g., reduced dead volumes, minimized unspecific sample adsorption, and negligible post-column peak dispersion) which results in a better MS/MS performance and more peptide identifications, as well as the ease and robustness of integrating functionality and automation. However, it seems that selected aspects of microchip-LC should be further improved by paying attention, e.g., to the reduction of cycle time in gradient elution (in view of high throughput screening) and the morphology of chromatographic beds in noncylindrical channels, in particular, to the effect of channel corners and associated structure-transport relations underlying hydrodynamic dispersion.

This work will provide a detailed look into the dependence of the packing structure of noncylindrical microfabricated chip devices and cylindrical nano-bore columns. In particular, the developed particle packed beds generated at different packing conditions (at different applied packing pressures and with or without the assistance of ultrasound) are investigated concerning their resulting packing qualities (porosities) and separation efficiencies under both isocratic and gradient elution modes. This work will show that with increased effort in generating packed beds with increased packing pressures and the assistance of ultrasound, the established bed porosities can be pushed closly to the random close packing limit with an external (interparticle) porosity of ~ 0.36. However, optimized packing porosities reduce the influence of the conduits' geometry and therefore the additional band broadening due to dispersion effects in inadequately packed corners of noncylindrical channels. This will lead to enhanced separation efficiency, a reduced dispersion and increased identification in complex bioanalytical and pharmaceutical problems.

References

[1] M.S. Tswett, Tr. Protok, Varshav. *Obshch. Estestvoistpyt., Otd. Biol. 14 (1903, publ. 1905) 20 (On the New Category of Adsorption Phenomenaand their Applications in Biochemical Analysis.* Reprinted and Translated in G. Hesse and H. Weil, Michael Tswett's erste chromatographische Schrift, Woelm, Eschwegen, Germany, **1954**).

[2] Tswett, M. S. *Ber. Deut. Bot. Ges.* **1906**, *24*, 384–393.

[3] Horvath, C.; Preiss, B.A.; Lipsky, S.R. *Anal. Chem.* **1967**, *39*, 1422–1428.

[4] Huber, J. F. K.; Van Vught, G. *Ber. Bunsenges.***1965**, *69*, 821–829.

[5] Halasz, I.; Gerlach, H. O.; Kroneisen, A.; Walkling, P. Z. Anal. Chem. 1968, 234, 97–103.

[6] Knox, J. H.; *Anal. Chem.* **1966**, *38*, 253–261.

[7] Desty, D. H.; Goldup, A.; Swanton, W. T.; Brenner, N.; Callen, J.E.; Weiss, M. D. *(Eds.), Gas Chromatography*, Academic Press, New York, NY,**1962**.

[8] Scott, R. P. W.; Kucera, P. *J. Chromatogr.* **1979**, *169*, 51–72.

[9] Neue, U. *HPLC Columns. Theory, Technology and Practice*, Wiley-VCH, New York, **1997**.

[10] Minakuchi, H., Nakanishi, K.; Soga, N.; Ishizuka, N.; Tanaka, N. *Anal. Chem.* **1996**, *68*, 3498–3501.

[11] Ishizuka, N., Kobayashi, H.; Minakushi, H.; Nakanishi, K.; Hirao, K.; Hosoya, K.; Itegami, T. Tanaka, N. *J. Chromatogr. A* **2002**, *960*, 85–96.

[12] Churacek, J.; Jandera, P*. Gradient Elution in Column Liquid Chromatography—Theory and Practice*, Elsevier, Amsterdam, The Netherlands, **1985**.

[13] Jandera, P. *Adv. Chromatogr.* **2005**, *43*, 1–108.

[14] Snyder, L.R.; Horvath C. (Eds.), *High-Performance Liquid Chromatography: Advances and Perspectives*, vol. 1, Academic Press, New York, NY, **1986**.

[15] Xie, J.; Miao, J.; Shih, J.; He, Q.; Liu, J.; Tai, Y.-C.; Lee, T.D. *Anal. Chem.* **2004***, 76*, 3756–3763.

[16] Reichmuth, D.S.; Shepodd, T.J.; Kirby, B.J. *Anal. Chem.* **2004**, *76*, 5063–5068

[17] Yin, H.; Killeen, K.; Brennen, R.; Sobek, D.; Werlich, M.; van de Goor, T. *Anal. Chem.* **2005**, *77*, 527–533.

[18] Fortier, M.-H.; Bonneil, E.; Goodley, P.; Thibault, P. *Anal. Chem.* **2005**, *77*, 1631–1640.

[19] Reichmuth, D. S.; Shepodd, T. J.; Kirby, B.J. *Anal. Chem.* **2005**, *77*, 2997–3000.

[20] Xie, J.; Miao, Y.; Shih, J.; Tai, Y.-C.; Lee, T.D. *Anal. Chem.* **2005**, *77*, 6947–6953.

[21] Carlier, J.; Arscott, S.; Thomy, V.; Camart, J.-C.; Cren-Olivé, C.; Le Gac, S. *J. Chromatogr. A* **2005**, *1071*, 213–222.

[22] Lazar, I.M.; Trisiripisal, P.; Sarvaiya, H. A. *Anal. Chem.* **2006**, *78*, 5513–5524.

[23] Ishida, A.; Yoshikawa, T.; Natsume, M.; Kamidate, T. *J. Chromatogr. A* **2006**, *1132*, 90–98.

[24] Mair, D.A.; Geiger, E.; Pisano, A. P.; Fréchet, J. M. J.; Svec, F. *Lab Chip* **2006**, *6*, 1346–1354.

[25] Rapp, E.; Tallarek, U. *J. Sep. Sci.* **2003**, *26*, 453–470.

[26] Rozing, G.; van de Goor, T.; Yin, H.; Killeen, K.; Glatz, B.; Kraiczek, K.; Lauer, H. H. *J. Sep. Sci.* **2004**, *27*, 1391–1401.

[27] Dutta, D.; Ramachandran, A.; Leighton, D. T. *Microfluid. Nanofluid.* **2006**, *2*, 275–290.

[28] Hlushkou, D.; Seidel-Morgenstern, A.; Tallarek, U. *Langmuir* **2005**, *21*, 6097–6112.

[29] Maier, R. S.; Kroll, D. M.; Bernard, R.S.; Howington, S.E.; Peters, J.F.; Davis, H. T. *Phys. Fluids* **2003**, *15*, 3795–3815.

[30] Leinweber, F. C.; Tallarek, U. *J. Chromatogr. A* **2003**, *1006*, 207–228.

Chapter 1 - Important chromatographic parameters

1 Chromatographic Separation

The dynamic equilibrium in the distribution of an analyte A is a commonly used method in chromatography to describe the separation process. A dynamic equilibrium appears for a two phase system, if substances cross over the phase boundary reversibly [1].

$$A_M \rightleftharpoons A_S \tag{1}$$

A_M is the analyte present in the mobile phase, whereas A_S depicts the analyte in the stationary phase. Because the volume of the two phases is not equal, a characterization of the affinity of the analytes to the mobile or stationary phase is not possible only by the consideration of equilibrium. A_M and A_S are in direct dependence on the concentration of the analytes in the related phases. The ratio of the analyte concentration in these phases in state of equilibrium is described by the distribution constant K_C.

$$K_C = \frac{[A_S]}{[A_M]} \tag{2}$$

K_C, the fraction of the analytes' concentration in the different and immiscible phases is called the distribution constant and was defined by Nernst. K_C is at fixed conditions a constant due to the Nernst distribution law, while the mobile phase is moved along the stationary phase and the analyte mixture is continuously reequilibrated. Separation can be obtained whenever the distribution constants of the analytes differ significantly. The migration speed is different and it is possible to separate substances chromatographically, since the distance of the responding signals at the detector (peaks) increases with the length moved.

Being migrated over the chromatographic column, it was theoretically derived, that discrete equilibria will occur to analyte in series over a well dimensioned length. It is nowadays accepted that equilibrium states cannot be reached in the columns' dynamic state [2 ,3].

2 Retention and Elution

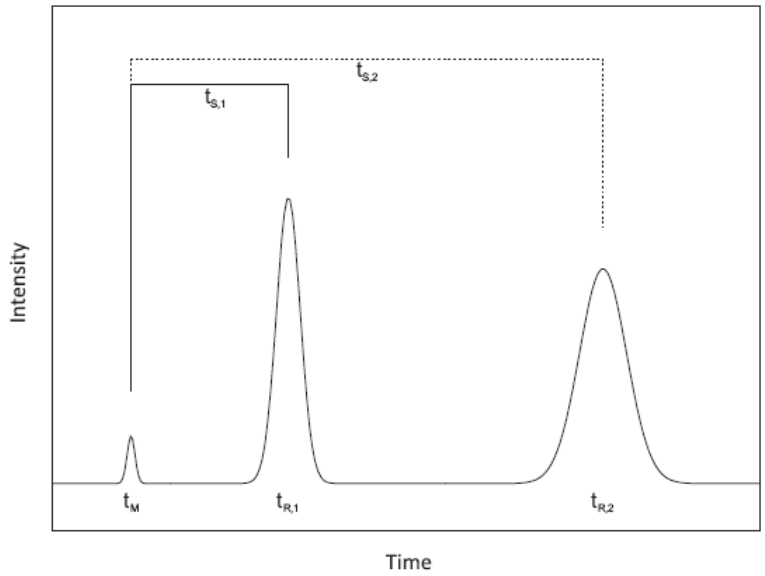

Figure 1: Schematic depiction of a chromatogram [1].

Figure 1 depicts schematically a separation of two analytes. The detected signals can be expressed with a Gaussian fit under ideal conditions. Fast eluting peaks are narrower than later eluting peaks due to the enhanced interactions of the analyte with the stationary phase.Due to the increasing band broadening related to the increased affinity to the stationary phase, which will be described in the chromatographic performance section. Another important parameter is the hydraulic retention time (t_0) or dead-time (t_M), which is defined as the time that is needed by the mobile phase or an analyte that shows no retention (dead-time marker) to pass the system from the injection to the detection. The dead-time marker is taken into account to determine the average linear mobile phase velocity (u_{av}).

$$u = \frac{L}{t_M} \tag{3}$$

If an analyte has a high value of K_C, its concentration in the stationary phase is high and the analyte will be considerably retained. If the value of K_C is decreased, the analytes concentration is high in the mobile phase and it will be eluted faster. If K_C equals zero, the substances will be eluted within the systems dead-time t_M. The time required for a retained analyte from the injection to the detection is described by the retention time (t_R). The difference of the retention and dead time describes the net retention time (t_S) of the analyte in the chromatographic system. It reflects the additional residence time of an analyte in the separation column compared to the dead-time marker.

$$t_{S,i} = t_{R,i} - t_M \tag{4}$$

The retention factor k'_i is given by the ratio of the net retention time and the dead time.

$$k'_i = \frac{t_{R,i} - t_M}{t_M} = \frac{t_{S,i}}{t_M} \tag{5}$$

The retention factor as a dimensionless parameter allows comparing chromatographic systems independent from the mobile phase velocity under specific physico-chemical conditions (constant mobile phase composition, temperature, particle size and surface chemistry of the stationary phase, etc.). It demonstrates how much longer an analyte stays inside the chromatographic column versus a non-retained (dead-time marker). The retention factor enables the user to compare different column lengths and new columns with respect to their reproducibility under constant physico-chemical conditions. In a complex mixture of analytes, small k'-values can lead to an insufficient resolution of the peaks and high values to an extended separation time. It is therefore of utmost importance to evaluate the separation of a given analytical problem concerning its separation and cost efficiency by adjusting the chromatographic conditions in an appropriated way.

3 Peak Shape

If an analyte is injected into a separation conduit and all molecules of an analyte would pass a packed bed of a chromatographic column with an equal velocity and reach the detector at the same time an infinitesimal narrow signal would occur. However, due to the occurrence of dispersive processes during separation, which will be explained in the following section, a Gaussian peak shape will be observed at the detector in a differential operation mode under ideal conditions (Figure 2). The peak basis is determined by the intersection points of the tangents at the inflection points with the baseline width (ω) and interrelated to the standard deviation,

$$\omega = 4 \cdot \sigma \tag{6}$$

The full width at half maximum (FWHM) is given by

$$\mathrm{FWHM} = \omega_h = 2\sigma \cdot \sqrt{2 \cdot \ln 2} \approx 2.355\sigma \tag{7}$$

and the peak width at the inflection points by

$$\omega_h = 2 \cdot \sigma \tag{8}$$

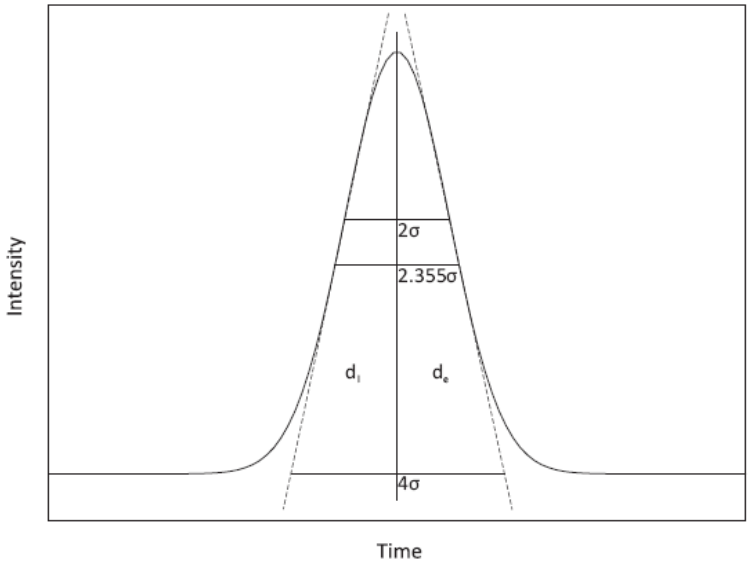

Figure 2: Symmetrical Gaussian peak [1].

In practice deviations from the ideal Gaussian profile can be quantified by the asymmetry factor (A_S) derived from the distance from the center line of the peak to the back slope (d_e) divided by the distance from the center line of the peak to the front slope (d_l), with all measurements made at 10% of the maximum peak height. For a symmetrical peak, A_S equals unity. A fast increasing and slowly decreasing peak is defined as a tailing peak ($A_S < 1$). A fronting peak shows contrary behavior ($A_S > 1$).

$$A_S = \frac{d_e}{d_l} \tag{9}$$

Peak symmetry depends basically on the shape of the adsorption isotherm for the distribution of the solute between the two phases. If the adsorption isotherm is linear over the concentration range concerned, the peak tends to be symmetrical. This indicates that the retention factor should be constant over the investigated concentration range. If the concentration is too high the retention factor and therefore the retention time will decrease due to the non-equilibrium of the analytes' concentration between the mobile and stationary phase. However, if the adsorption isotherm is not linear, the peak will become asymmetrical because of overloading which results in peak tailing. Adsorption in contradiction to partition will always result in asymmetric peaks (usually with tailing) unless the surface chemistry or packing quality is very carefully prepared.

4 Chromatographic performance

The historical origin of the use of the term “plate height” in chromatography is from the original publication of Martin and Synge [2]. In order to obtain an equation for the elution curve from a chromatographic column, the authors borrowed the plate concept from distillation theory and applied it to gas chromatography (GC). As well as providing an elution curve equation, the GC plate theory also allowed the number of theoretical plates in a column to be calculated. Theory shows that increased column efficiency leads to restrained peak dispersion. Packing efficiencies are therefore directly related to the number of theoretical plates of a column (the better the packing the more plates it provides). Plate height bridges the gap between rate and plate theory and is quantified by the height equivalent to one theoretical plate (HETP) and to the variance per unit length (ω). It can be estimated using the retention time (t_R) of an analyte and the width ($W_{1/2}$; FWHM) or the fraction of the height h_P divided by the area A_P of a peak.

$$N = 5.545\left(\frac{t_R}{FWHM}\right)^2 \tag{10}$$

$$N = 2\pi\left(\frac{t_R \cdot h_p}{A_p}\right)^2 \tag{11}$$

The plate height (H) is a quantitative measurement of column efficiency. It is given by the fraction of the columns length (L) over the number of theoretical plates.

$$H = \frac{L}{N} \tag{12}$$

The peak width is closely associated with the column efficiency. The interaction area is identified as the plate height and depending on the interaction time and flow rate. To operate at optimal efficiency the plate height has to be studied as a function of the linear average mobile phase velocity (u_{av}) using isocratic conditions [3].

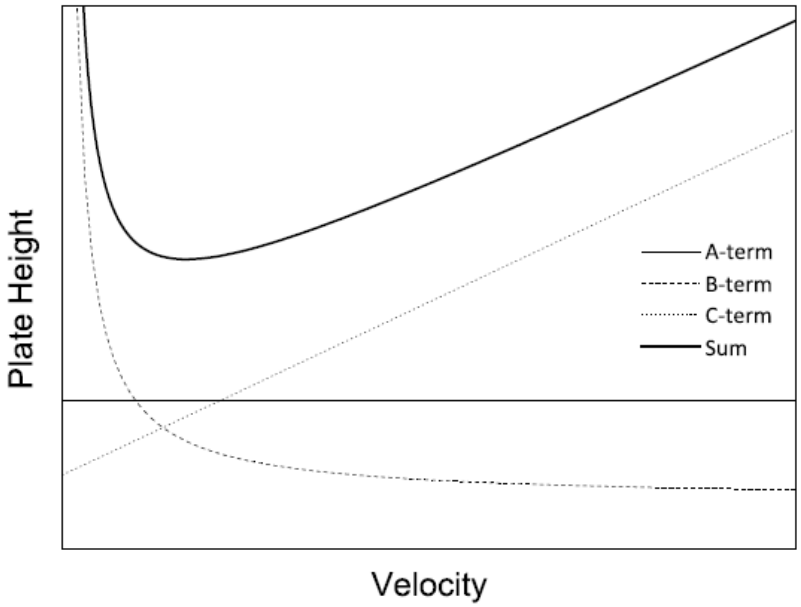

Figure 3: Theoretical depiction of the plate height versus average linear velocity curve (H-u_{av}-plot) [3].

The most frequently mentioned equation and the therefore resulting plot (Figure 3) describing the physico-chemical interplay of a molecule transported through a chromatographic system was reported by van Deemter et al. in 1956 [4].

$$H = A + \frac{B}{u_{av}} + C \cdot u_{av} \tag{13}$$

The van Deemter equation was the first rate equation to be developed. There exist, however, a number of alternative rate equations that have been reported but when subjected to experimental test, the Van Deemter equation has been shown to be the most appropriate equation for the accurate prediction of dispersion in chromatographic systems. The van Deemter equation is particularly pertinent at mobile phase velocities around the optimum velocity, where the plate height is minimal. Consequently, as all columns should be operated around the optimum velocity for maximum efficiency, the Van Deemter equation is particularly important in column design. In routine HPLC, columns are always operated at velocities above the optimum. The reduced column efficiency is less significant than the shorter analysis time at higher flow rates.

A, B and C are parameters that charactrize the broadness of peaks and the height of a theoretical plate. As advantage over the plate theory, the van Deemter model allows to predict changes in chromatographic efficiency, if parameters, e.g., the packing porosity, flow rate, column geometry, or physical properties are changed.

The A-term in the Van Deemter equation is called eddy diffusion term. Eddy diffusion occurs as a result of multiple flow paths through a particle packed column bed. Analyte molecules

cannot flow along a straight path through the column. Each analyte molecule follows a different flow path, which causes dispersion (different path lengths). Some molecules will travel a longer distance and will lag behind the peak center; others will follow shorter paths and are slightly ahead. This effect results in slight differences in retention. As depicted in figure 4 the red molecule (2) takes a shorter way between the layers a and b than the blue one (1). The homogeneity of the packed bed strongly affects the A-term. The probability of different path lengths due to radial movements is greater in a column having a poorly packed bed. However, particle size, column length and geometry and the therefore generated bed priorities (quality of the packed bed) contribute to the plate height due to the influence on axial heterogeneity of the flow velocity. Eddy diffusion is especially important for columns with internal diameters of 2 - 5 mm. However, the contribution from eddy diffusion in the van Deemter equation will be lowered when a column of this size is packed regularly with small, spherical particles with small deviations in particle size (narrow particle size distributions). Eddy diffusion is independent of the mobile phase velocity at high flow rates, but depends on the particle diameter (d_p) and the obstruction factor λ, which describes the tortuosity of a particulate bed [5].

$$A \propto \lambda \cdot d_P \tag{14}$$

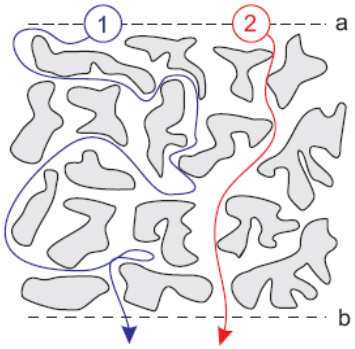

Figure 4: Peak broadening due to different pathways through a material [3].

Large and irregular shaped particles will have a stronger dispersion effect, while with regularly shaped particles (spherical) the path length distribution between the particles is smaller, which explains that spherical particles can more easily form a uniformly packed bed. Conversely, an irregularly packed bed consists of flow channels of different shapes and diameters, resulting in a broader velocity distribution radial to the column cross section.

The peak broadening due to longitudinal (axial) diffusion is contained in the B-term. The B-term in the van Deemter equation refers to the diffusion of individual analyte molecules in the mobile phase along the longitudinal direction of a column. This diffusion is proportional to

u_{av}^{-1} so that it contributes to peak broadening only at very low flow rates below the minimum (optimum) plate height. At very high flow rates the B-term becomes insignificant.

Molecular diffusion takes place independent of the longitudinal (axial) flow direction and is the result of concentration gradients in the mobile phase. In the center of the peak the concentration is at its maximum, whereas the concentration at the front and end of the peak is lower. The contribution to band broadening will be relatively strong at long residence times in the column, which is present at low flow rates. As the flow rate increases, the effect on total peak broadening will be diminished. In practice, it is best to select flow rates that minimize the effect of longitudinal diffusion on column efficiency. Longitudinal diffusion is proportional to the molecular diffusion coefficient (D_M), which is affected by viscosity, temperature and molecular size. Increased temperature and diffusion coefficient increase the B term, while increased viscosity decreases it [6].

$$B \propto \lambda \cdot D_M \tag{15}$$

The B-term is therefore dependent of the diffusion coefficient and the obstruction factor, λ. Diffusion coefficients for components in liquids are generally very small (usually 10000 times smaller than in gas phase). Because the high mobile phase velocity, the B-term is hardly significant in liquid chromatography and is typically neglected, due to the small diffusion coefficients of the analytes. But, if the C-term is very small (typically for packing with particles smaller than 2 µm) the importance raises, because the mass resistance factor looses its relative importance and the B-term is more pronounced in the overall efficiency determined.

The C-term refers to mass-transfer resistance induced peak broadening. The C-term in the van Deemter equation relates to the mass transfer of sample components between the stationary phase and the mobile phase during separation. The overall C-term is divided into two separate mass transfer terms: one considering the resistance of mass-transfer in the stationary phase (C_S) and one in the mobile phase (C_M) [3, 7, 8]. Analyte molecules present in the mobile phase diffuse towards the mobile/stationary phase interface, and enter into the stationary phase. To maintain partition equilibrium, some molecules will return to the mobile phase. After some time there will be a reverse process as the analytes move from the stationary phase the mobile phase. This results in a continuous mass transfer taking place between the mobile and the stagnant stationary phase during the whole separation process.

$$C = C_S + C_M \tag{16}$$

The C_S-term describes contributions to peak broadening in the stationary phase**.** The C_S-term is determined by the amount of stationary phase (a low term is advantageous for a good

efficiency) and the extent of interaction of the sample with the phase (represented by the retention factor) and the distances the sample molecules have to cover. If the stationary surface is solid, C_S will be proportional to the time that a species needs to ad- and desorb on the surface (Figure 5). The resistance to mass-transfer in the bulk solution depends on the solute ability to reach the solid surface from its position. The C_M-term is describing the contributions to peak broadening in the mobile phase. Because the linear velocity of the mobile phase is lower near the column wall (or the stationary phase particles) as in the center (or adjacent to the particles) the analyte molecules experience different velocities. This results in peak broadening in the mobile phase, which is described by the C_M term.

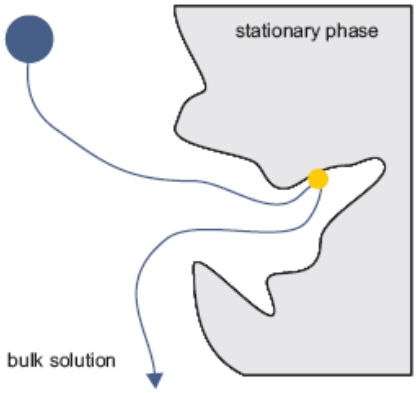

Figure 5: Peak broadening due to of mass-transfer resistance. Adsorption/Desorption taking place at the indicated yellow area [3].

Resistance to mass transfer is dependent on the speed with which the partition equilibrium between mobile and stationary phase is obtained. Since the resistance to mass transfer in the mobile phase is not the same for all molecules of one type of analyte which depends on the location in the column at a particular time and the distance they have to travel to partition between phases, this will also result in peak broadening of that analyte in the column.

When analyte molecules can move quickly between mobile and stationary phase, the column efficiency is remarkably improved. The speed with which analyte molecules cross between phases is related to the diffusion coefficient and the ad-/desorption behavior of the analyte molecule in a particular mobile phase. Analyte molecules with large diffusion coefficients in the mobile phase will need less time to move to the mobile/stationary phase interface. The same applies for the movement into and out of the stationary phase. Thus, the equilibrium is reached faster with a larger molecular diffusion coefficient for the mobile phase and with a smaller particle diameter. This means that the contribution of the C_M and C_S to plate height decreases and the separation is more efficient. The contribution of both C-terms

to the overall peak broadening appears to increase with the linear velocity of the mobile phase. As mobile phase velocity increases, the exchange of molecules between mobile phase and stationary phase has to be significantly fast to keep up the equilibrium between the phases. If equilibrium is not maintained, the peaks broaden and the efficiency and separation quality decrease. The C-terms' contribution to the H-u-curve is therefore considerable. A small C-term leads to a fairly flat ascending H-u-curve at higher mobile phase velocities. This means that the separation can be carried out at higher mobile phase velocities without sacrificing separation quality. Ideally, the ascent in the C-term should be close to zero. Column packings with smaller particle diameter reduce the C-term remarkably. To achieve a small plate height over a wide linear velocity range, by fabricating efficient columns with insignificant reduced separation efficiencies at higher linear, has been the driving force over the last years in particle and column design.

The retention factor influences both C-terms. The relative band broadening and thus the plate number appear to be dependent on the extent of interaction of a component with the stationary phase. Therefore, it becomes important to consider which peak is used to calculate an effective column plate number. Due to external instrument contributions, the overall column efficiency tends to increase with an increased retention factor, so that the dependence is strongest at the beginning of the chromatogram and decreases at higher retention factors. The external band broadening is not negligible in many cases but looses its relative importance with increased retention. Thus, plate numbers are best calculated from a peak somewhere at the end of the chromatogram (k' > 5). Therefore, it is suitable to derive the real column performance at higher k'-values. The goal in chromatography is to generate columns and analytical systems with less external contributions to achieve not only a high efficiency in separation over wider velocity ranges but also over (ideally) the whole retention range.

5 Definition of the particle size distribution

The behavior and properties of particulate materials are dependent on particle morphology, size and size distribution. Therefore proper measurement and interpretation are fundamental to an understanding of particle handling and properties during the application. The size of a spherical homogeneous particle is uniquely defined by its diameter. For regular, compact particles such as cubes or regular tetraeders, a single dimension can be sufficient to define the size. With some other regular shaped particles like cones or irregularly shaped particles it is necessary to specify more than one dimension. In this case three dimensions are needed.

The sample preparation is a crucial point when measuring particle size distribution (PSD). The particles have to be dispersed (perfectly) otherwise the particles tend to coagulate. The stability of a wetted system (used for the measurement of the PSD) in this work, depends on the forces between the particles. A random motion tends to decrease the distance of discrete particles and an agglomeration is possible. The occurrence of particle collisions depends on, e.g., the viscosity, temperature and the concentration of the particles itself. Whether two or more particles combine or not depend on the potential barrier between them. Two energy terms are related to this phenomenon; first, the attractive van der Waals force, and second the repulsive force due to the electrical double layer that surrounds every single particle. It is therefore of utmost importance to set the parameters in terms of sample preparation and sample measurement in a proper and scientific way, to ensure a highly dispersed slurry.

For the purpose of the description of a PSD different average diameters are possible to be determined. These averages represent a group of individual values in a simple and concise manner for a group of investigated particles. It is therefore very important, that the averages or means determined are representative for the investigated batch. Several definitions of the mean particle diameter are commonly used which, depending on the underlying size distribution, provide different values [9].

$$d_p = \frac{\sum d_{p,i} d_{p,i}^k n_i}{\sum d_{p,i}^k n_i} \tag{17}$$

For example, for k = 0 the number-averaged ($d_{p,\#}$), for k = 2 the surface-averaged ($d_{p,surf}$), and for k = 3 the volume-averaged ($d_{p,vol}$) particle diameter is obtained. The Sauter mean diameter (d_S) is the characteristic parameter for the specification for a bulk material and can be calculated from the volume-averaged and surface-averaged particle sizes

$$d_S = \frac{\sum d_{p,i}^3 n_i}{\sum d_{p,i}^2 n_i} \tag{18}$$

For symmetrical distributions all mean diameters are coinciding. For non-symmetrical distributions the determined values for the different diameters increase with k.

Specific surface area (S_v – surface-to-volume ratio) of a collection of spherical particles with a variable size is multiplied by the mean Sauter diameter and can be calculated by [9].

$$S_v = \frac{\sum \pi d_{p,i}^2 n_i}{\sum \left(\frac{\pi}{6}\right) d_{p,i}^3 n_i} = \frac{6}{d_S} \tag{19}$$

6 Hydraulic permeability

To sustain the percolation at a constant velocity of a stream of mobile phase along a column, a certain pressure must be maintained at the column inlet. Without any loss of generality, it can be assumed that the fluid is Newtonian and that the flow is laminar. Then, this pressure drop (Δp) is related to the characteristics of the column and of the mobile phase. The general physical law governing the resistance to flow of a Newtonian fluid with viscosity η through a packed bed is Darcy's law [10]. This is a linear relationship between the superficial velocity $u_{sf} = F_v/A$ (where F_v is the volumetric flow rate and A the cross-sectional area of the conduit) and pressure drop over the length of the packed bed $\Delta p/L_{bed}$ [11]. This term is multiplied by constant contribution due to κ_D/η where κ_D is representing the specific Darcy permeability.

$$u_{sf} = \frac{F_v}{A} = \frac{\kappa_D \Delta p}{\eta L} \tag{20}$$

This linear relationship is valid for the case of creeping flow (linear-laminar flow regime) and that both the Newtonian fluid and porous medium remain incompressible. Starting deviations from this law for packed beds at Reynolds numbers $Re = u_{inter}d_p/\nu$, calculated with d_p (particle diameter), $u_{inter} = u_{sf}/\varepsilon_{inter}$, (where u_{inter} is the interparticle velocity and ε_{inter} the interparticle porosity) and the kinematic viscosity ν, larger than 1 are attributed to inertial forces (nonlinear-laminar or viscous-intertial flow regime) [12]. As can be seen from Eq. (20) the specific permeability κ_D is simply defined as a proportionality constant which can be accurately observed experimentally, but it does not provide any insight into the physics of flow through the actual material.

The Kozeny-Carman equation represents the most successful and still widely used attempt to provide a simple, general expression for the permeability in terms of material properties, without the need to solve the actual, extremely complicated flow problem. It is based on the assumption that an irregular distribution of pore dimensions in a packed bed of particles can be replaced by a bundle of twisted, nonintersecting channels with similar diameter (d_{ch}) in which flow resistance is governed by the Hagen-Poiseuille law for laminar flow in open tubes. In analogy to Eq. (20) we can formulate [11]

$$u_{sf} = \frac{F_v}{A} = \frac{\varepsilon d_{ch}^2}{16 k_0 \mu} \frac{\Delta p}{\eta L} \tag{21}$$

where k_0 is a shape factor and μ is the hydraulic tortuosity factor, a geometrical parameter of the one-dimensional capillaric model. Thus, the specific permeability in the Kozeny-Carman approach is

$$\kappa_{KC} = \frac{\varepsilon d_{ch}^2}{16 k_0 \mu} \tag{22}$$

In analogy with the established practice in hydraulics, d_{ch} is assumed to be four times the hydraulic radius, defined as the flow cross-sectional area divided by the wetted perimeter. For a particle-packed bed it can be expressed as

$$d_{ch} = \frac{4\varepsilon_{inter}}{S_v(1-\varepsilon_{inter})} = \frac{4\varepsilon_{inter}}{\left(\frac{6}{d_S}\right)(1-\varepsilon_{inter})} \tag{23}$$

where S_v is the specific surface area given by the evaluated particle size distribution (see Eq. 19). The Sauter mean diameter is the defined characteristic parameter specifying the studied particles in the chromatographic bed.

After combining Eq. (22) and Eq. (23) the well-known form of the Kozeny-Carman equation is obtained

$$\kappa_{KC} = \frac{\varepsilon_{inter}^3}{k_0 \mu (1-\varepsilon_{inter})^2}\left(\frac{d_S}{6}\right)^2 = \frac{\varepsilon_{inter}^3}{(1-\varepsilon_{inter})^2}\frac{d_S^2}{f_{KC}} \tag{24}$$

According to Carman [13] the best value of the combined factor $k_0\mu$ to fit most experimental data on packed beds is equal to 5. Usually, the factors 6^2 and $k_0\mu = 5$ are combined to yield the Kozeny-Carman factor $f_{KC} = 180$.

The hydrodynamic permeability is a direct indicator for the packing quality (density of a particulate packed bed) under constant physico-chemical conditions. The higher the permeability of a confined bed the higher the porosity and the more band broadening can be expected, if considering particles of the same mean diameter. This will result in a reduced chromatographic separation efficiency.

References

[1] Cammann, K. *Instrumentelle Analytische Chemie*, Spektrum, Akad. Verl., **2001**.

[2] Martin, A. J. P.; Synge, R. L. M. *Biochem. J.* **1941**, *35*, 1358–1368.

[3] Skoog, D. A.; West, D. M.; Holler, F. J.; Crouch, S. R. *Fundamentals of Analytical Chemistry* 8th ed., Thompson Learning, London, **2004**.

[4] S. Jung, Experimentelle Untersuchungen zur hydraulischen Permeabilität und chromatographischen Effizienz gepackter Chipkanäle, Diploma Thesis - Philipps-University at Marburg, **2008**.

[5] van Deemter, J. J.; Zuiderweg, F. J.; Klinkenberg, A. *Chem. Eng. Sci.* **1956**, *5*, 271–289.

[6] Hawkes, S. J.; *J. Chem. Educ.* **1983**, *60*, 393–398.

[7] Scott, R.; Simpson, C. *Liquid Chromatography Column Theory*, Wiley India, New Delhi, **2009**.

[8] Siouffi, A.-M. *J. Chromatogr. A* **2006**, *1126*, 86–94.

[9] Allen, T *Powder sampling and particle size determination*, Elsevier, Amsterdam, The Netherlands, **2003**.

[10] Darcy, H. *Les Fontaines Publiques de la Ville de Dijon*, Victor Dalmont, Paris, **1856**.

[11] Dullien, F.A.L. *Porous Media – Fluid Transport and Pore* Structure, Academic Press, San Diego, **1991**.

[12] Hlushkou, D.; Tallarek, U. *J. Chromatogr. A* **2006**, *1126*, 70–85.

[13] Carman, P.C. *Flow of Gases Through Porous Media*, Academic Press, New York, **1956**.

Chapter 2 - Packing density of slurry-packed capillaries at low aspect ratios

1 Introduction

The nonuniform radial distribution of voidage in packed beds of spherical particles in the direct vicinity of the column wall has been studied intensively, particularly for small column diameter (d_c) to particle diameter (d_p) ratios, on the order of $d_c/d_p < 20$ [1, 2]. This importance stems from the influence of the aspect ratio d_c/d_p on pressure drop, bed permeability, liquid hold-up, linear velocity, and hydrodynamic dispersion [3-10] (and references therein). It has been shown by classical studies and for uniform spheres with a smooth surface that the interparticle voidage starts with a maximum value of nearly unity at the column wall and then displays damped oscillations (with a period close to d_p) over a distance of about 4-5 d_p into the bulk of the bed until the void fraction reaches values typical for random-close sphere packings [11-13]. Since these early studies, this unique behavior has been demonstrated consistently throughout the literature by involving either a variety of experimental approaches [14-21], or by direct simulation and analysis of the structure of confined sphere packings [22-27]. Figure 1 reflects these conclusive findings by the radial voidage distribution for a simulated cylindrical packing of uniform solid spheres with a cylinder-to-particle diameter ratio of $d_c/d_p = 10$ and an average interparticle porosity of $\varepsilon_{inter} = 0.42$ [28]. The first minimum and first maximum, respectively, of the voidage distribution are found at distances about $d_p/2$ and one d_p from the wall. This purely geometrical wall effect (cf. Figure 1) is explained by a decrease of packing order as the distance from the wall increases. It is a direct result of the inability of the particles to form a close packing against the hard surface of the column wall. The wall is flat, with a rugosity which is at least one order of magnitude smaller than the particle diameter. So, particles can touch the wall, they cannot penetrate it. The first particle layer of the bed in contact with the wall is not only highly ordered, but differs from subsequent layers, because the interstitial space between the wall and the first layer cannot be partially occupied by other particles. Subsequent particle layers towards the center of the column do not retain this level of order. The packing configuration determines the way in which these layers are packed, and the degree of randomness increases with the distance from the wall. The resulting voidage oscillations are influenced by the size distribution and shape of the particles, as well as by the roughness of the particle surface [29]. While for analytical HPLC practice $d_c/d_p \gg 100$, transport properties in packed

beds become strongly affected by the geometrical wall effect as d_c/d_p decreases towards 10 or even below, so that the critical wall region (a wall annulus, if cylindrical packings are studied) occupies a significant volumetric fraction of the bed. In particular, the analysis of dispersion in confined cylindrical packings at low aspect ratios (d_c/d_p < 20) is a topic with a long tradition in engineering [9], and it is generally accepted that the asymptotic axial dispersion coefficient under these conditions depends on the macroscopic flow heterogeneity due to the geometrical wall effect. The geometrical wall effect becomes important again for the fabrication of cylindrical nanobore HPLC columns where values of d_c/d_p between 10 and 20 are common. This is caused by the fact that the reduction of the column inner diameter (with respect to analytical HPLC columns) in nano-HPLC is not accompanied by a corresponding reduction of the particle size. In nano-HPLC typical values for d_c and d_p are 75 µm and 5 µm, respectively. There is a strong decrease from d_c/d_p » 100 in analytical HPLC to d_c/d_p ~ 10-20 in nano-HPLC.

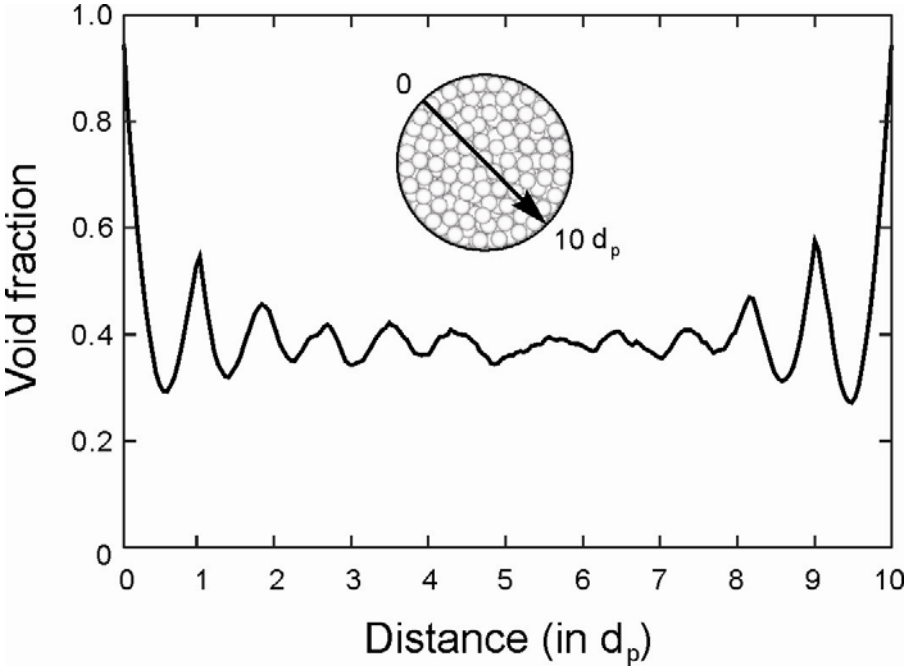

Figure 1: Distribution of the interparticle void fraction for a confined cylindrical packing of solid spheres with an average bed porosity of ε_{inter} = 0.42 and a cylinder-to-particle diameter ratio of d_c/d_p = 10. The porosity distribution is calculated along the indicated arrow over the whole length of the bed (L_{bed} = 300 d_p). Reprinted with permission from Khirevich et al. [28].

It is noted for clarity that this purely geometrical effect in immediate vicinity of the column wall is distinct from a second and more extended wall effect caused by friction between the bed and column wall [30-32]. Compared to the geometrical wall effect the latter is traditionally discussed in chromatography in connection with relatively large aspect ratios. The mobile phase velocity is lower in a region close to the wall, the stream being slowed by the low void fraction associated with a higher packing density near the wall caused by the

high radial stress applied by the bed to the wall as a consequence of friction between particles. This effect strongly depends on the packing procedure and operational characteristics. It is related to the relatively high compressibility of pulverulent materials and complex distribution of the axial and radial stress during the compression of the bed.

Thus, the wall can interact with the packed bed in two different ways which are simple to understand individually but whose consequences and interplay as a function of d_c/d_p are harder to figure out. The fractional volume of the column affected by this second wall effect is larger than that affected by the first (geometrical) one, by nearly two orders of magnitude for any column but microbore ones. Ultimately, for nanobore columns, with d_c/d_p on the order of 10, it is the geometrical wall effect which is expected to become dominating in view of the radial porosity distribution and average bed porosity. The geometrical wall effect may strongly influence the achievable (intrinsic) packing density in nano-HPLC which then can be expected to depend on the aspect ratio, but also on packing mode and, as mentioned before, on particle characteristics like the shape and size distribution functions, or surface roughness.

While the impact of the aspect ratio d_c/d_p in packed capillaries on flow resistance and separation efficiency has often been addressed [3-6, 8] (and references therein), one important parameter usually undetermined and consequently uncorrelated with the analyzed permeability and dispersion is the average interparticle bed porosity at a given value of d_c/d_p. On the other hand, this parameter contains information about a contribution of the geometrical wall effect to the overall bed density, and it is an important one for accurate simulations of packing microstructure and associated structure-transport relations. An improved radial bed porosity model which allows to predict radial voidage variations in relation to the average bed voidage is also available [1]. This complementary information would be helpful in comparing data which have been obtained for different aspect ratios. In this line we studied experimentally the influence of d_c/d_p in view of the geometrical wall effect (cf. Figure 1) on average bed porosity in cylindrical capillaries for $5 < d_c/d_p < 50$, covering a range of aspect ratios relevant to nano-HPLC. 5 µm-sized porous C18-silica particles were slurry-packed into fused-silica capillaries with inner diameters from 30 to 250 µm. Our data demonstrate a systematic dependence of packing densities on the aspect ratio. In addition to the operation of a geometrical wall effect we interpret this dependence with respect to particle characteristics like the size distribution, shape, and surface roughness.

2 Experimental Section

2.1 Chemicals and materials

Acetonitrile, methylene chloride, isopropanol, and acetone were purchased from Sigma-Aldrich (Taufkirchen, Germany). Benzene came from Carl Roth GmbH & Co. KG (Karlsruhe, Germany). Polystyrene standards with a molecular mass M_r of 2500, 5000, 9000, 17500, 30000, and 50000 g/mol were purchased from Supelco (Bellefonte, PA). Polystyrene standards with 20000, 100000, and 500000 g/mol came from Fluka Chemie GmbH (Buchs, Switzerland). In our studies we employed 5 µm-sized Zorbax SB-C18 particles with a mean intraparticle pore size of 80 Å (Agilent Technologies, Waldbronn, Germany). They were slurry-packed into cylindrical fused-silica capillaries (Polymicro Technologies, Phoenix, AZ) having different inner diameters (30-250 µm i.d.) and an outer diameter of 360 µm.

2.2 Hardware configuration

All measurements have been run on an Agilent 1100 liquid chromatograph consisting of a degasser and a nanopump, equipped with a diode-array UV detector (DAD) working at 210 nm. Manual sample injection was performed via a two-position injection valve with a 4 nl internal loop volume (Model CN4 from Vici AG Valco Europe, Schenkon, Switzerland). The loop was continuously flushed using a syringe installed on a syringe pump (Harvard Apparatus, Holliston, MA). Two 15 µm i.d., 900 mm long fused-silica restriction capillaries served as pre-columns to provide sufficient working pressure. Volumetric flow rates were determined by an additional flow sensor (Model SLG-1430-25, Sensirion, Staefa, Schwitzerland) installed behind the analytical system. Reproducibility of the measurements was guaranteed by the accuracy of the nanopump with an absolute error below 1%. Measurements were conducted at 298 ± 1 K.

2.3 Preparation of packed capillaries

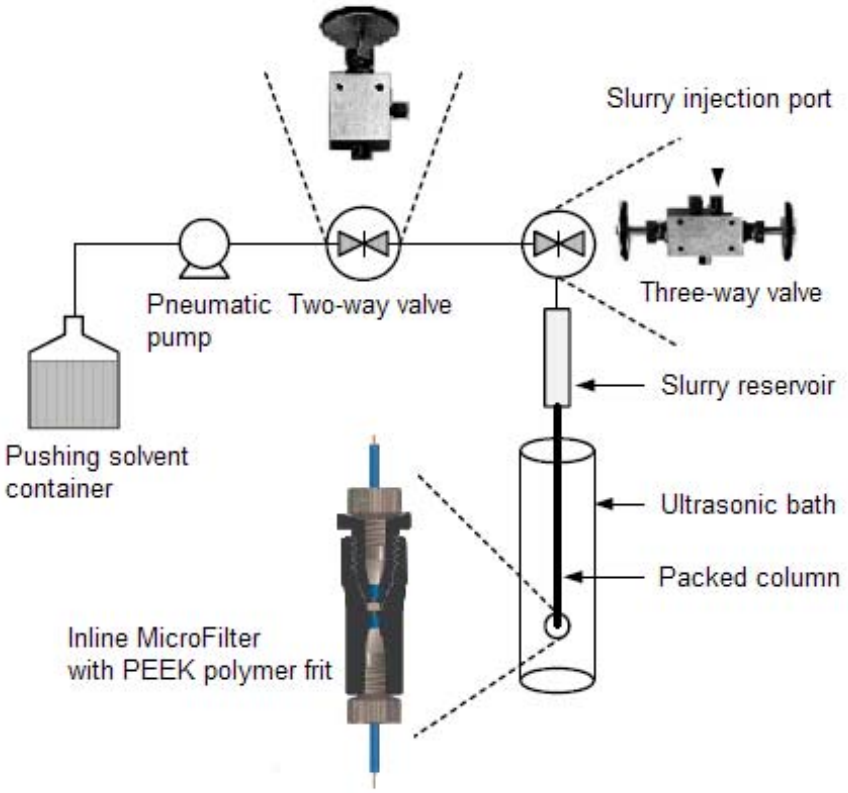

Figure 2: Schematic of a slurry packing device for silica-based capillry columns.

Fused-silica capillaries were slurry-packed using a WellChrom K-1900 pneumatic pump (Knauer GmbH, Berlin, Germany). A 500 µm i.d. glass-lined metal tubing was used as the slurry reservoir. SSI two-way and three-way valves (ERC, Riemerling, Germany) were placed between the pneumatic pump and slurry reservoir for pressure release and slurry injection, respectively [33] as depicted in Figure 2. An in-line MicroFilter with a PEEK polymer frit (Upchurch Scientific, Oak Harbor, WA) was connected to the capillary outlet before the packing process started. Slurries were prepared by suspending 20 to 100 mg (depending on capillary i.d.) of the dry particles in 1 ml acetone while applying ultrasound for 10 min.

Degassed 70/30 (v/v) acetonitrile/water was used as the pushing (packing) solvent for the consolidation of the particulate beds. Starting with 100 bar the packing pressure was increased to 500 bar and held at this level until a sufficient filling of the capillaries (~ 200 mm) was realized. Then, the packing process was stopped, pressure released slowly, and the slurry reservoir rinsed. Afterwards, the pressure was raised again up to 500 bar and the bed was further consolidated in an ultrasonic bath (Bandelin Electronic, Berlin, Germany) for 4 min. This procedure was repeated until the packing did not settle further, which took no longer than 30 min. As demonstrated by Figure 3 with a representative sample, the use of

ultrasound appeared to be critical for obtaining densely packed capillaries. Some of the beds were extruded after the packing process to verify whether this combination of ultrasound and high pressure lead to a disruption of particles which would cause an apparent settling during packing. However, no sign of particles which have been crashed during the packing process could be found when compared with the original appearance of the particles.

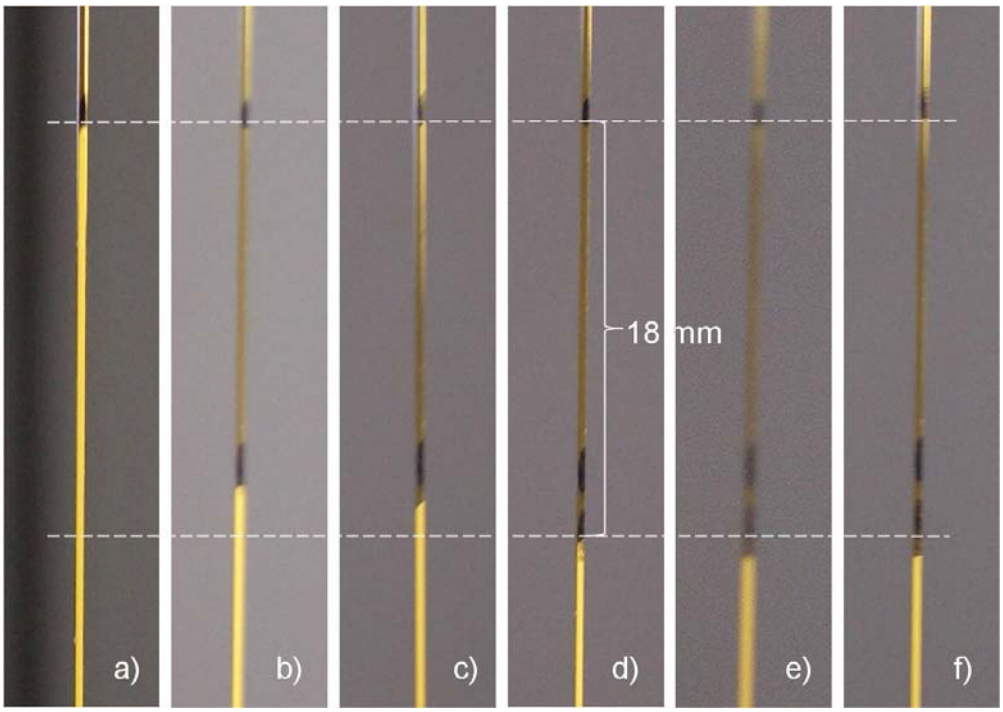

Figure 3: Influence of ultrasound on the bed length (L_{bed}) during slurry-packing of a 200 µm i.d. capillary. a) Start, L_{bed} = 220 mm, applied pressure: 450 bar; and after b) 3 min, c) 6 min, d) 10 min, e) 13 min, and f) 16 min of ultrasound application. The bed can be further consolidated by almost 2 cm.

After consolidation of the packing, the system was depressurized slowly and the capillary removed from the packing device. The pushing solvent was replaced by bidistilled, filtered, and degassed water containing 1 g/l NaCl which was needed for obtaining mechanically stable frits. The packed capillary was again fitted into the packing device and flushed for at least 30 min with 500 bar to ensure a complete exchange of packing solvent by the aqueous electrolyte solution. Afterwards, the packing was fixed by an inlet and an outlet frit, which were sintered using an arc fusion splicer (Model FSM-05SV from Fujikura, Tokyo, Japan). In all cases, the final total bed length was about 150 mm.

Subsequently, packing beyond the frits was flushed out by applying a pressure of 200 bar. This took at least 30 min and also demonstrated the stability of the sintered frits and packed bed. After microscopic examination of the frits and packing quality, the packed capillary was cut directly at the inlet frit and connected with a special fitting (VICI AG Valco Europe, Schenkon, Switzerland) to the injection valve. The detection window was prepared

immediately behind the outlet frit. In order to position the capillaries they were inserted into a capillary electrophoresis cell (colour code green) which was then fixed in the conventional DAD holder and assembled in the DAD.

2.4 Particle size distribution

Measurements of the particle size distribution were performed using a Mastersizer 2000 with a Hydro SM manual small volume sample dispersion unit (Malvern Instruments GmbH, Herrenberg, Germany). A spatula tip of the 5 µm-sized Zorbax SB-C18 particles was dispersed in 30 ml isopropanol and injected into the apparatus. Three measurments were performed and a Sauter mean diameter of 5.51 ± 0.12 µm has been determined. The actual size distribution of these particles is shown in Figure 4.

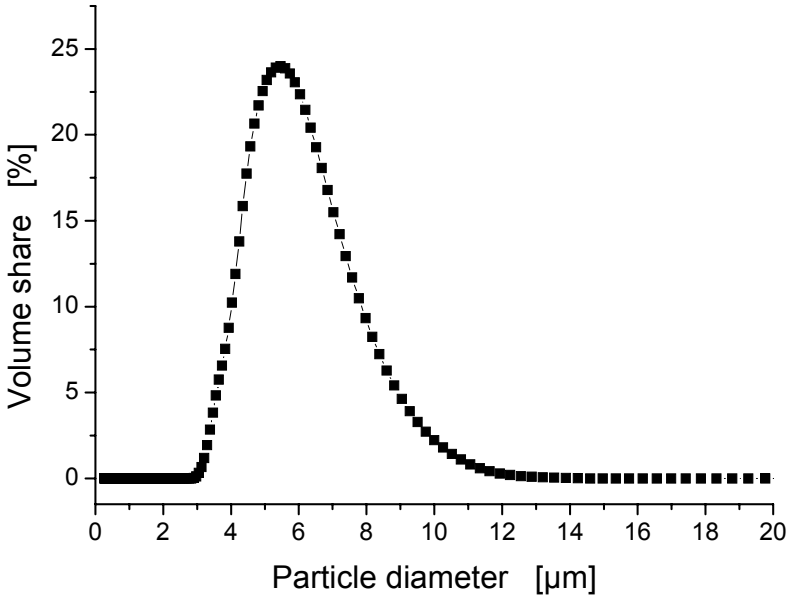

Figure 4: Size distribution of the 5 µm Zorbax SB-C18 particles.

3 Results and Discussion

3.1 Packing quality of the slurry-packed capillaries

In the present work we adapted a procedure for obtaining densely packed, fixed beds of reversed-phase silica particles in cylindrical fused-silica capillaries which is based on the results of Vissers et al. [34] in developing selection criteria for slurry packing techniques in micro-HPLC. We used acetone as the slurry liquid for the 5 µm-sized Zorbax SB-C18 particles and 70/30 (v/v) acetonitrile/water as the packing liquid. The data of Vissers et al. [34] demonstrate that this combination of noncoagulating slurry liquid with coagulating

packing liquid results in a good quality of slurry-packed capillaries. No consolidation has been observed during the conditioning of packed beds of reversed-phase support materials for capillaries that have been packed with 70/30 (v/v) acetonitrile/water as coagulating packing liquid [34]. Our results confirm these findings in that we generally did not observe voids in the packed capillaries or dead volume behind the inlet frits during or after chromatographic analysis. Microscopic inspection revealed that all packings had a high degree of homogeneity and remained densely packed in the axial direction. Figure 5 illustrates by representative micrographs that the capillaries were also densely packed in the radial direction. In addition, the first layer of particles forming a uniform ring along the inner surface of the fused-silica capillaries becomes visible, especially for the smaller i.d. capillaries (cf. Figure 1).

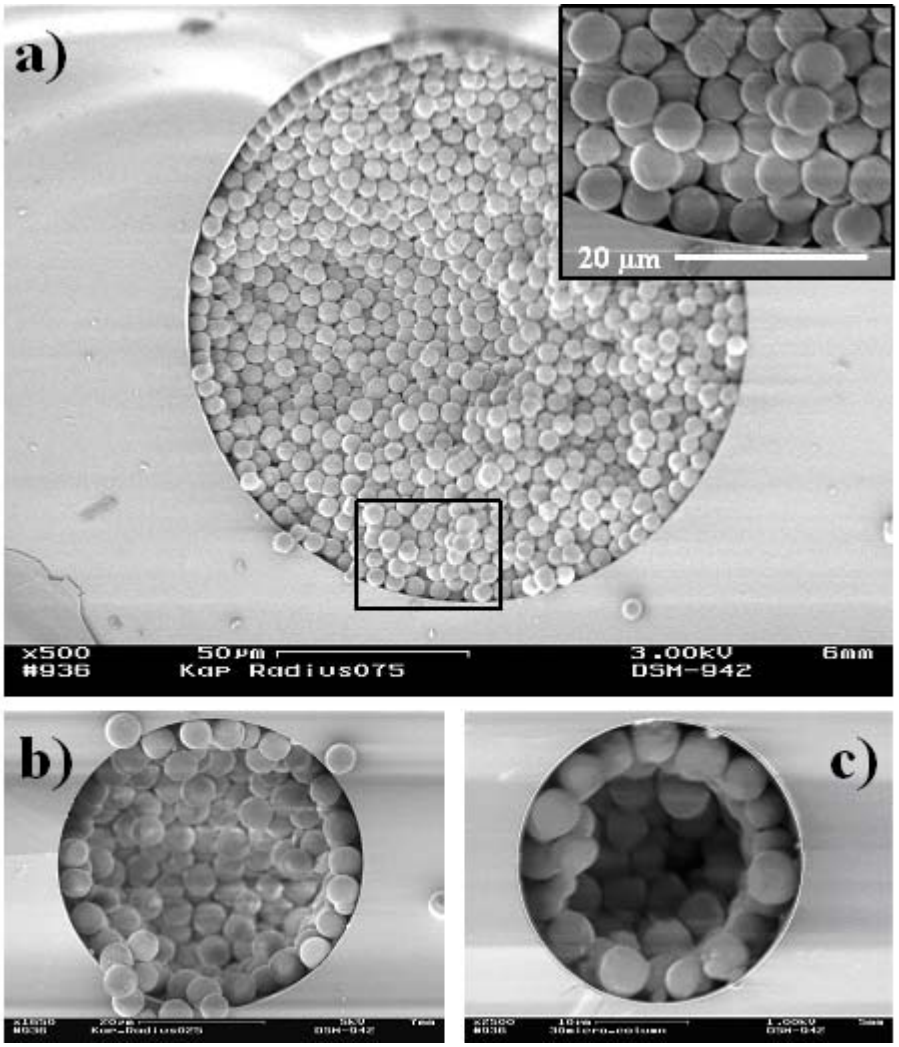

Figure 5: Cross-sectional view on cut capillaries packed with the 5 µm-sized Zorbax SB-C18 particles. a) 180 µm i.d., b) 50 µm i.d., and c) 30 µm i.d. capillary.

In analyzing separation efficiency as a criterion for the packing quality we found a minimum axial plate height with the packed 100 µm i.d. capillaries around 17 µm at an average velocity through the beds of about 0.6 mm/s, which gives a reduced plate height of slightly more than 3. This result was obtained with benzene in 70/30 (v/v) acetonitrile/water as the mobile phase (k' ~ 1.5) and indicates a good quality of these packings, in particular, when comparing with the data of Vissers et al. [34] who have employed very similar particles. For example, they reported a reduced plate height of 4.7 with 5 µm-sized Zorbax SB-C18 particles using acetone as the slurry liquid and methanol as packing liquid. With Zorbax ODS the reduced plate height was 3.5 using a noncoagulating/coagulating system of tetrahydrofuran (slurry liquid) and 70/30 (v/v) acetonitrile/water (packing liquid) [34].

Concerning a correlation of the geometrical wall effect with separation efficiencies in dependence of the aspect ratio d_c/d_p Kennedy and Jorgenson [4] and later Hsieh and Jorgenson [6] have shown by clear trends that the performance of fused-silica capillaries packed with 5 µm-sized porous C18-silica particles improves with decreasing capillary inner diameter between 12 and 50 µm. A closely related diameter-dependent dispersion has also been observed in some numerical studies which suggest that the adverse influence of the geometrical wall effect on axial dispersion remains significant even at aspect ratios on the order of d_c/d_p = 100 [10, 35]. (N.B. In practice, however, other and more extended wall effects, e.g., the one mentioned in the Introduction may be involved and become dominating at higher aspect ratios depending on how a column packing is generated. This will contribute to an even stronger diameter-dependent dispersion than based on the geometrical wall effect alone.) By contrast, Eeltink et al. [8] did not find a corresponding dependence of separation efficiency and flow resistance on the aspect ratio for 75, 100, and 150 µm i.d. capillaries packed with 5 and 10 µm-sized particles, but concluded that differences in the packing and particle batch quality associated with different aspect ratios become more important. In the present work, the preparation of frits occasionally introduced heterogeneities which caused peak tailing and prevented an accompanying correlation of packing density and aspect ratio with the separation efficiency.

3.2 Analysis of interparticle bed porosity with polystyrene standards

Halász and Martin [36] demonstrated the use of inverse size-exclusion chromatography for the determination of internal porosity of the packing inside liquid chromatography columns. In size-exclusion chromatography (SEC) sample mixtures that are dissolved in the mobile phase can be separated according to their different molecular sizes [37]. Classical SEC uses the known pore structure of an adsorbent to determine the molecular mass distribution of a polymer mixture. On the other hand, if the molecular mass of a series of polymer standards is known, the pore-size distribution of an unknown stationary

phase can be determined from the distribution of their retention times. Provided that standard samples are available for calibration, experiments show that there is a correlation between the average molecular mass of the polymers (M_r) and the average diameter of the pores (d_{pore}) from which they are excluded (exclusion volumes), assuming that all the polymeric chains remain in the same conformation of a random coil [37]. For polystyrene dissolved in methylene chloride, we have the following relation [36]

$$M_r = 2.25\ (d_{pore})^{1.7}. \quad (1)$$

This correlation is based on the fact that the access of molecular coils into pores is limited by steric hindrance caused by the wall. For each packing material, there are two thresholds, a low and a high one. Molecules larger than the high threshold have no access to any significant fraction of the intraparticle porosity. Molecules smaller than the low threshold have access to the entire pore volume. Molecules of intermediate size have access to part of the pores, as indicated by Eq. (1). The validity of this correlation relies on the assumption that the polymer samples used, although having different molecular masses, have the same structure and that the same solvent is used.

Conversely, in inverse SEC solutions of known polymeric samples are injected into a column packed with an unknown adsorbent, and the retention behavior of these solutes can be correlated with the pore size distribution of the packing material [36, 38]. For polystyrene samples eluted by methylene chloride through a bed of porous C18-silica particles, the correlation is obtained by solving Eq. (1) for d_{pore}

$$d_{pore}\ [\text{Å}] = 0.62\ (M_r)^{0.59} \quad (2)$$

In this work a total of 9 polystyrene standards with molecular masses ranging from 250 to 500000 g/mol were dissolved in methylene chloride and injected into a capillary packed with the 5 μm-sized Zorbax SB-C18 particles. Benzene was included in the calibration and used for the determination of the total accessible porosity of the capillary.

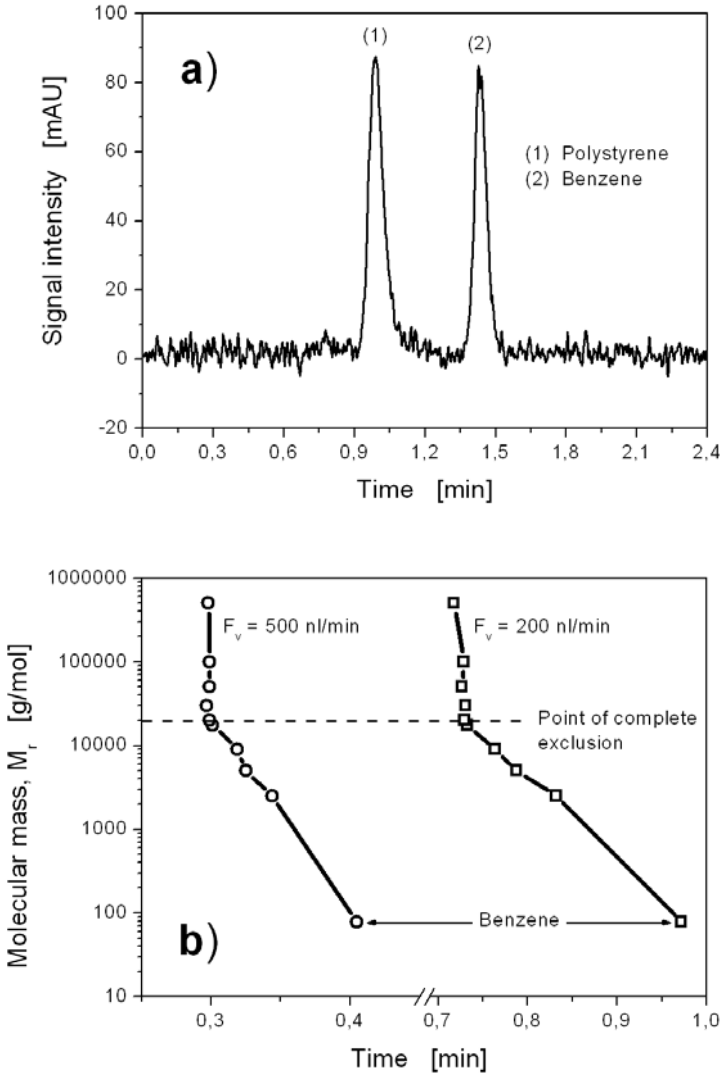

Figure 6: a) Elution of a polystyrene (M_r = 20000 g/mol) together with benzene through a 100 µm i.d. packed capillary at a volumetric flow rate of F_v = 500 nl/min (1.75 mm/s). The asymmetry factor for the polystyrene peak is 1.11. b) Plots of the logarithm of the molecular weight of the polystyrenes versus their retention time for elution through a 50 µm i.d. packed capillary at two volumetric flow rates, as indicated.

The elution of a polystyrene (M_r = 20000 g/mol) together with benzene is shown in Figure 6a. Plots of the logarithm of the molecular weight of the polystyrenes versus their retention time at two volumetric flow rates (Figure 6b) reveal a bimodal pore-size distribution representing the internal (intraparticle) and external (interparticle) porosity of the fixed bed [36, 38].

For both flow rates in Figure 6b the borderline between the two porosities is around M_r = 20000 g/mol (see point of complete exclusion in Figure 6b) which translates to a mean intraparticle pore size of 214 Å (Eq. (2)), a value that is decidedly larger than the nominal pore size of these Zorbax particles (80 Å). However, it has been pointed out by Halász and Martin [36] that d_{pore} assigned by a polystyrene standard of molecular weight M_r (Eq. (2)) is 2.5 times as large as the coil diameter of molecules of the same polystyrene. In other words,

rotational coil diameters must be some 2.5 times smaller than the diameter of the pores to allow the polymer unhindered access to the pores. After taking this into account we obtain d_{pore} = 85.6 Å at the point of complete exclusion (Figure 6b), a value that remains just slightly larger than the nominal pore size of the support. As a consequence of this conclusive result the polystyrene standard with M_r = 20000 g/mol was used in subsequent experiments for the determination of the interparticle pore volume (V_{inter}) of a packed capillary. The total pore volume (V_{total}) was taken as the retention volume of benzene in methylene chloride, which was practically equal to that of uracil under reversed-phase chromatography conditions with 70/30 (v/v) acetonitrile/water as the mobile phase.

The interparticle and total bed porosities (ε_{inter} and ε_{total}, respectively) were calculated using the total capillary volume, V_c, itself derived from the geometrical dimensions of a capillary, $V_c = \pi r_c^2 L_{bed}$ (where r_c is the capillary radius and L_{bed} is the bed length), while the intraparticle porosity (ε_{intra}) is defined with respect to the volume of the particles

$$\varepsilon_{inter} = \frac{V_{inter}}{V_c} \tag{3}$$

$$\varepsilon_{total} = \frac{V_{total}}{V_c} \tag{4}$$

$$\varepsilon_{intra} = \frac{V_{intra}}{V_c(1-\varepsilon_{inter})} \tag{5}$$

In the determination of both ε_{inter} and ε_{total} the injection volume V_{inj} is taken into account by subtracting 0.5 V_{inj} (2 nl) from V_{inter} (Eq. (3)) and V_{total} (Eq. (4)), respectively. Total, interparticle, and intraparticle porosities are related by the following balance

$$\varepsilon_{total} = \varepsilon_{inter} + (1-\varepsilon_{inter})\varepsilon_{intra} \tag{6}$$

which is used to derive ε_{intra} from the independent determinations of ε_{inter} (polystyrene standard with M_r = 20000 g/mol) and ε_{total} (benzene; both in methylene chloride) [38].

3.3 Dependence of packing density on column-to-particle diameter ratio

Figure 7a shows the results of the determination of i) the total bed porosity ε_{total} (Eq. (4)), ii) the interparticle or external porosity ε_{inter} (Eq. (3)), and iii) the intraparticle or internal porosity ε_{intra} (Eq. (6)) as a function of the column diameter (d_c) to particle diameter (d_p) ratio

for a range of almost $5 < d_c/d_p < 50$. We note first that, as expected, the values for the intraparticle porosity ($\varepsilon_{intra} \approx 0.29$) remain independent of d_c/d_p because the available intraparticle pore space with respect to the overall particle volume for rigid particles should remain unaffected by the actual density of a packed bed. In contrast, the packed beds external porosity shows a steady decrease from $\varepsilon_{inter} \approx 0.47$ at $d_c/d_p = 5$ towards $\varepsilon_{inter} = 0.36$-$0.37$ at $d_c/d_p = 40$-50. The same trend is necessarily observed for the total bed porosity in view of Eq. (6) and the fact that $\varepsilon_{intra} = const.$ This systematic increase in ε_{inter} and ε_{total} at decreasing capillary diameter (decreasing d_c/d_p) lends support to the operation of a geometrical wall effect which affects and even limits the achievable packing density due to the inherent oscillations of interparticle voidage in a transition region between the hard inner surface of the fused-silica capillaries and the bulk, random-close packing of particles, if the latter can be reached at all which depends on the actual d_c/d_p-ratio. As a consequence of the geometrical wall effect (cf. Figure 1) higher interparticle and total bed porosities result while d_c/d_p is decreased into a critical regime in which the volumetric contribution of porosity oscillations near the wall to the overall bed volume cannot be neglected any longer. Figure 7b compares the data for ε_{inter} as a function of d_c/d_p obtained in this work with data reported by de Klerk [1] for $d_c/d_p < 20$. While our data show a continuous decrease in ε_{inter} for $d_c/d_p > 5$ with increasing capillary diameter over the whole range of d_c/d_p, the data of de Klerk [1] demonstrate a practically constant value for ε_{inter} (slightly higher than 0.36) already at $d_c/d_p > 13$. With $d_c/d_p < 10$, the average interparticle voidage increases to reach $\varepsilon_{inter} = 0.42$ at $d_c/d_p = 5$.

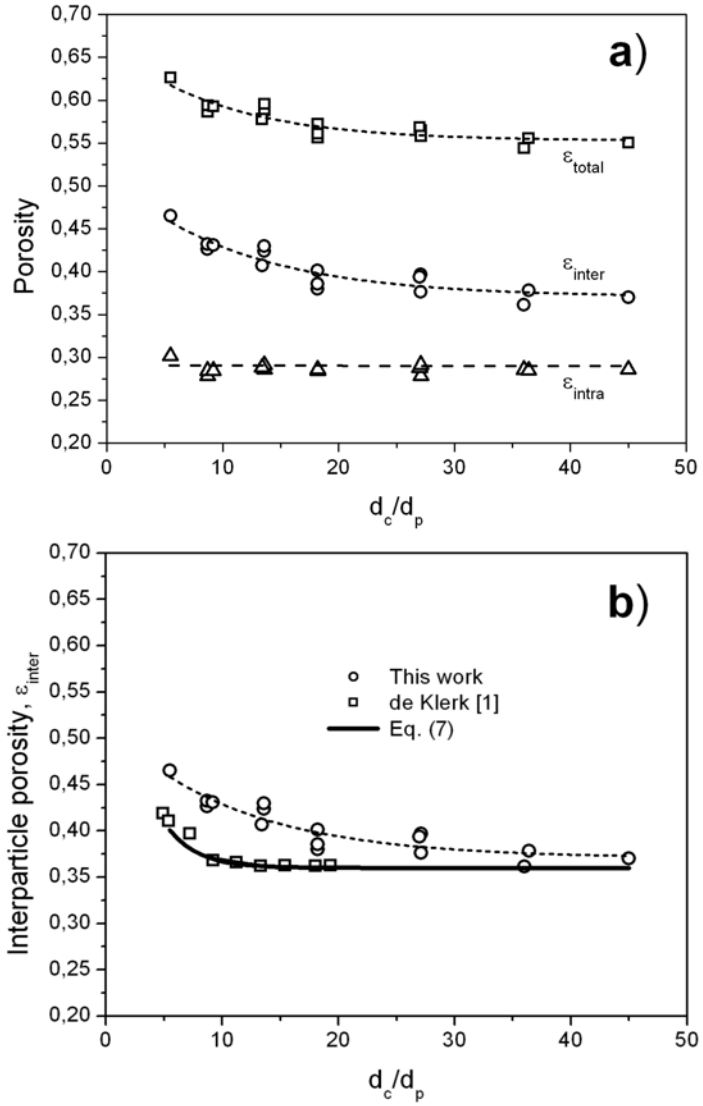

Figure 7: a) Plot of the experimentally determined values of total, interparticle, and intraparticle porosities in slurry-packed capillaries as a function of the aspect ratio for $5 < d_c/d_p < 50$. b) Comparison of the interparticle porosities with data of de Klerk [1].

Thus, while our data and those of de Klerk [1] tend towards similar values of ε_{inter} = 0.36-0.37 at higher values of d_c/d_p, the values of ε_{inter} reported by de Klerk [1] are always below our data and demonstrate a significant increase only for $d_c/d_p < 10$. The solid line in Figure 7b is based on the following equation which has been used by de Klerk [1] to model average bed porosity

$$\varepsilon_{inter} = \varepsilon_{bulk} + 0.35 \exp\left(-0.39 \frac{d_c}{d_p}\right) \qquad (7)$$

The constants in this exponential decay function have been determined by regression of the data by Carman [39] due to its consistency and spread. The effect of the packing procedure

is embodied in the average bed porosity at infinite column diameter (ε_{bulk}). In his classical work, Carman [39] found an exponential decrease in average bed porosity in the region $2 < d_c/d_p < 10$, while constant voidage values were obtained at larger d_c/d_p-ratios. Leva and Grummer [29] like Sonntag [40] and Schnitzlein [24] reported a linear relationship between the inverse ratio of column-to-particle diameter and the bed voidage which is quite similar to an exponential decay function. Our data for ε_{inter} in Figure 6b also display an exponential decay at increasing d_c/d_p, although this decay towards ε_{inter} = 0.36-0.37 extends over a larger range of d_c/d_p values than in the work of de Klerk [1].

In comparing our data for ε_{inter} in packed capillaries used for nano-HPLC as a function of d_c/d_p with those of de Klerk [1] in the context of much larger fixed beds which are typically employed in engineering applications, several aspects must be precautioned which limit a direct comparison, but which, on the other hand, provide helpful insight into those parameters which influence the achievable bed porosities. In particular, the experiments of de Klerk [1] were conducted with nonporous glass beads of d_p = 3 mm in glass columns with d_c ranging from 4.9 to 57.5 mm. Glass beads were poured in the dry state into these columns with some tapping of the column wall. In our work, by contrast, porous C18-silica particles of d_p = 5 µm were packed into fused-silica capillaries with d_c ranging from 30 to 250 µm employing a slurry-packing procedure with high pressures and ultrasonication. Thus, while similar d_c/d_p ratios are realized with both approaches (cf. Figure 7b), the packing modes, column dimensions, and particle characteristics are different.

Leva and Grummer [29] noted that for regular shaped particles the average bed porosity is influenced by the packing mode, column-to-particle diameter ratio, the particle shape, particle size distribution, and roughness of the particle surface. An additional aspect which becomes important when moving from engineering applications with mm-sized particles to nano-HPLC with d_p in the lower µm-range is the very different absolute particle size. As particle size is reduced, the interparticle force, which is the collective outcome of weak forces such as van der Waals and electrostatic forces, becomes more important [41]. Long-range interparticle forces, such van der Waals and electrostatic forces, play an essential role in the packing of fine particles. This picture differs from that of coarse particles where each particle can be treated as an individual. Therefore, fine particles are usually packed in the form of a slurry which disperses the particles and avoids formation of agglomerates due to the strong cohesive forces. Thus, optimization of the packing process is a far more important issue with the small particles used in this work than for the large ones employed by de Klerk [1] which can be placed individually in a drop-and-roll analogy.

In comparing our experimental data with those of de Klerk [1] it is interesting to note that in both cases very similar values are approached at large d_c/d_p for the average bed voidage, with ε_{inter} = 0.36-0.37. In the literature, usually four random packing modes for

spheres at large d_c/d_p are distinguished [1]. a) Very loose random packing ($\varepsilon_{bulk} \approx 0.44$) obtained by gradual defluidization of a fluidized bed or by sedimentation. b) Loose random packing ($\varepsilon_{bulk} \approx 0.40$-$0.41$) obtained by letting spheres roll individually in place, or by dropping the spheres into the container as a loose mass. c) Poured random packing ($\varepsilon_{bulk} \approx 0.375$-$0.391$), obtained by pouring spheres into a container. d) Dense random packing ($\varepsilon_{bulk} \approx 0.359$-$0.375$), obtained by vibrating or shaking down the packed bed. The experimental data for large d_c/d_p reported in Figure 6b demonstrate that a dense packing is not only possible with the coarse particles employed by de Klerk [1] ($\varepsilon_{inter} \approx 0.36$ at $d_c/d_p > 13$), but also with the fine particles used in this work ($\varepsilon_{inter} \approx 0.37$ at $d_c/d_p > 35$). It indicates that the packing procedure followed in this work is indeed optimized for obtaining densely packed beds of fine particles.

The fact that our experimental data, however, demonstrate an earlier increase in ε_{inter} at decreasing d_c/d_p compared to the data of de Klerk [1] (Figure 7b) may be explained by an individual property of the employed Zorbax particles. They exhibit a higher degree of surface roughness than the relatively smooth glass beads employed by de Klerk [1]. Figure 8 illustrates that these Zorbax particles generally have a rugose external surface. This characteristic has been claimed as being responsible for higher bed porosities of analytical columns compared to particles with a smooth surface, and it has been further argued that this unusual surface roughness of the Zorbax particles can limit chromatographic performance at high flow rates by generating an unusually high film mass transfer resistance [42]. Returning to capillary packing at low values of d_c/d_p the roughness of the particle surface influences the ease with which a stable packing configuration can be achieved. It has strong impact on packing microstructure in the wall region which reflects the transition of interparticle voidage from its maximum value of nearly unity at the column wall via damped oscillations (with a period close to d_p) over a distance of about 4-5 d_p into the bulk of the packing. Particles with a rough surface have a higher resistance to the slippage needed here for a denser packing. It has been demonstrated in simulations that by lowering the friction parameters the particles settle more and achieve a lower overall void fraction of the packing [2].

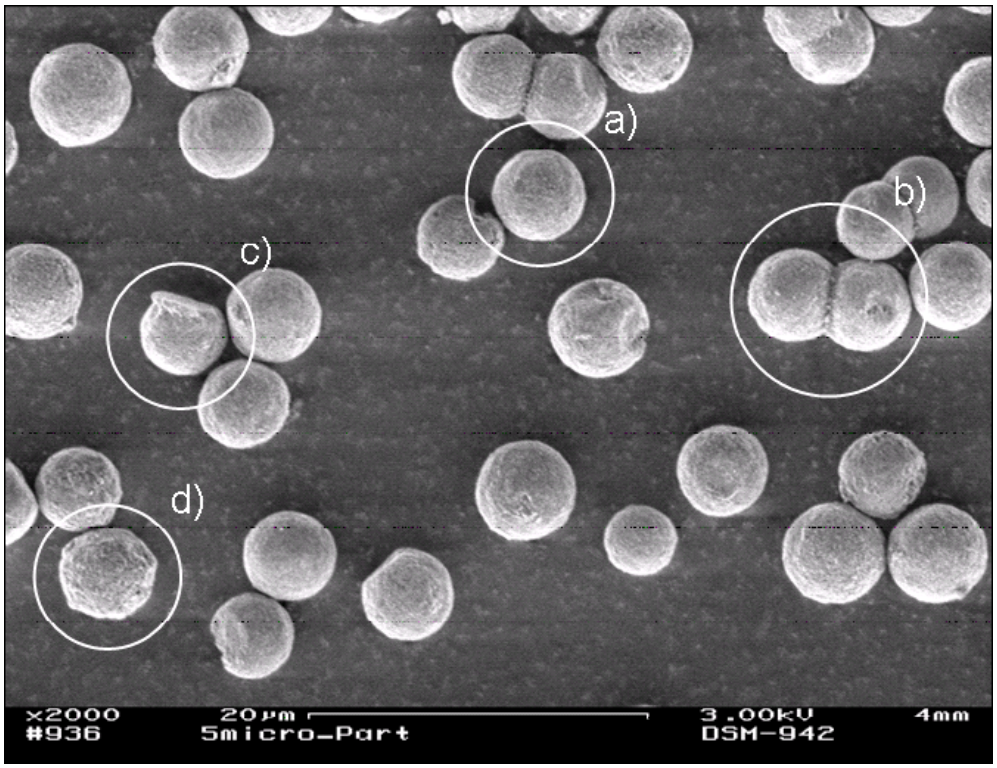

Figure 8: Packing material (5 µm-sized Zorbax SB-C18 particles) dispersed in acetone and stirred in a vibrating shaker for 30 seconds. a) Well-shaped spherical particle, b) particle dimer, c) particle originating from a dimer, d) abrasion of the particles external surface. The surface morphology of these basically spherical particles is rough and sometimes irregular.

In addition, the particles employed in this work (although basically spherical) sometimes appear, at least partly, damaged and irregularly shaped (Figure 8). Further, the unsymmetrical particle size distribution contains a significant amount of larger-than-average species (Figure 3). These factors will also contribute to difficulties in obtaining dense packings at low aspect ratios with porosities comparable to the work of de Klerk [1] (ε_{inter} = 0.36-0.37 for d_c/d_p > 10, Figure 7b) who employed more uniformly sized and shaped glass beads.

4 Conclusions

This work provides evidence for the operation of a geometrical wall effect in slurry-packed capillaries in a range of capillary diameter (d_c) to particle diameter (d_p) ratios of $5 < d_c/d_p < 50$. Straight fused-silica capillaries with inner diameters from 30 to 250 µm were packed with 5 µm-sized porous C18-silica particles, following an optimized slurry-packing procedure reported by Vissers et al. [34] involving optimized slurry and packing solvents, high pressure, and ultrasonication. It allowed to obtain homogeneous and densely-packed capillary columns which did not show a consolidation during further operation. The geometrical wall effect results from the inability of the hard silica-based particles to form a close packing against the hard surface of the capillary wall. The first particle layer of the bed in contact with the wall is not only highly ordered, but differs from subsequent layers, because the interstitial space between the wall and the first layer cannot be partially occupied by other particles. As the distance from the wall increases the packing order decreases until the void fraction reaches values typical for random-close packings. The associated damped voidage oscillations cover a distance of 4-5 particle diameters from the wall towards the bulk packing. When the volumetric contribution of this critical wall region to the overall volume of the packed bed becomes significant, the interparticle porosity is expected to increase. This interplay between a more loosely packed wall region and a more tightly packed core region forms the basis for explaining the improved performance of fused-silica capillaries packed with 5 µm-sized porous C18-silica particles in the work of Jorgenson and co-workers [4, 6] as the capillary inner diameter is decreased from 50 to 12 µm. With such a decrease in aspect ratio the core region ultimately disappears and the packing structure is dominated by the loosely packed wall region; the packing structure becomes effectively more homogeneous.

In general, oscillations of interparticle voidage next to the column wall depend on the packing mode, particle shape, size distribution and absolute particle size, as well as the surface roughness. These aspects, in turn, also influence the discussion on phenomena related to the intensity of the geometrical wall effect like the pressure drop – flow rate characteristics or hydrodynamic dispersion in packed beds at low values of d_c/d_p. For example, the use of irregular-shaped particles or particles with a broad size distribution can prevent the formation of significant porosity oscillations compared to uniform particles with a perfect spherical shape and single diameter (monosized spheres; cf. Figure 1). This may explain why Eeltink et al. [8] did not retrieve a noticeable effect of d_c/d_p on the flow resistance and separation efficiency with packed capillaries for d_c/d_p = 7.5, 10, and 15. They employed 10 µm-sized particles with a broad, actually bidisperse size distribution. Smaller particles then can fill the voids between the larger ones, thereby preventing the formation of systematic oscillations in porosity with significant amplitudes next to the capillary wall.

Additional studies are required to resolve the influence of the particle size distribution and roughness of the particle surface on a fine-tuning of the geometrical wall effect. These relevant details often remain undetermined or are not consequently used throughout the analysis, although practically no particle size distribution is like the other. Only then can consecutive effects like hydrodynamic dispersion in packed beds at low values of d_c/d_p be more quantitatively understood [3-6, 8, 10, 20, 43]. An important prerequisite for that investigation is the realization of packings with reproducible and known characteristics (e.g., homogeneity of packing, average porosity, etc.) to make a correlation between particle size distribution, surface roughness, packing mode, and separation efficiency in dependence of the aspect ratio d_c/d_p meaningful.

References

[1] de Klerk, A. *AIChE J.* **2003**, *49*, 2022-2029.

[2] Theuerkauf, J.; Witt, P.; Schwesig, D. *Powder Technol.* **2006**, *165*, 92-99.

[3] Karlsson, K.-E.; Novotny, M. *Anal. Chem.* **1988**, *69*, 1662-1665.

[4] Kennedy, R. T.; Jorgenson, J. W. *Anal. Chem.* **1989**, *61*, 1128-1135.

[5] Li, W.; Pyo, D.; Wan, Y.; Ibaňez, E.; Malik, A.; Lee, M. L. *J. Microcolumn Sep.* **1996**, *8*, 259-268.

[6] Hsieh, S.; Jorgenson, J. W. *Anal. Chem.* **1996**, *68*, 1212-1217.

[7] Winterberg, M.; Tsotsas, E. *AIChE J.* **2000**, *46*, 1084-1088.

[8] Eeltink, S.; Rozing, G. P.; Schoenmakers, P. J.; Kok, W. Th. *J. Chromatogr. A* **2004**, *1044*, 311-316.

[9] Delgado, J. M. P. Q. *Heat Mass Transfer* **2006**, *42*, 279-310.

[10] Maier, R. S.; Kroll, D. M.; Davis, H. T. *AIChE J.* **2007**, *53*, 527-530.

[11] Roblee, L. H. S.; Baird, R. M.; Tierney, J. W. *AIChE J.* **1958**, *4*, 460-464.

[12] Benenati, R. F.; Brosilow, C. B. *AIChE J.* **1962**, *8*, 359-361.

[13] Ridgway, K.; Tarbuck, K. J. *Chem. Eng. Sci.* **1968**, *23*, 1147-1155.

[14] Dixon, A. G. *Can. J. Chem. Eng.* **1988**, *66*, 705-708.

[15] Küfner, R.; Hofmann, H. *Chem. Eng. Sci.* **1990**, *45*, 2141-2146.

[16] Mueller, G. E. *Powder Technol.* **1992**, *72*, 269-275.

[17] Hosseini-Ashrafi, M. E.; Tüzün, U. *Chem. Eng. Sci.* **1993**, *48*, 53-67.

[18] Giese, M.; Rottschäfer, K.; Vortmeyer, D. *AIChE J.* **1998**, *44*, 484-490.

[19] Sederman, A. J.; Alexander, P.; Gladden, L. F. *Powder Technol.* **2001**, *117*, 255-269.

[20] Tang, D.; Jess, A., Ren, X.; Blümich, B.; Stapf, S. *Chem. Eng. Technol.* **2004**, *27*, 866-873.

[21] Ren, X.; Stapf, S.; Blümich, B. *AIChE J.* **2005**, *51*, 392-405.

[22] Manz, B.; Gladden, L. F.; Warren, P. B. *AIChE J.* **1999**, *45*, 1845-1854.

[23] Nandakumar, K.; Shu, Y.; Chuang, K. T. *AIChE J.* **1999**, *45*, 2286-2297.

[24] Schnitzlein, K. *Chem. Eng. Sci.* **2001**, *56*, 579-585.

[25] Maier, R. S.; Kroll, D. M.; Bernard, R. S.; Howington, S. E.; Peters, J. F.; Davis, H. T. *Phys. Fluids* 2003, *15*, 3795-3815.

[26] Hlushkou, D.; Seidel-Morgenstern; A., Tallarek, U. *Langmuir* **2005**, *21*, 6097-6112.

[27] Freund, H.; Bauer, J.; Zeiser, T.; Emig, G. *Ind. Eng. Chem. Res.* **2005**, *44*, 6423-6434.

[28] Khirevich, S.; Höltzel, A.; Hlushkou, D.; Tallarek, U. *Anal. Chem.* 2007, *79*, 9340-9349.

[29] Leva, M.; Grummer, M. *Chem. Eng. Prog.* 1947, *43*, 713-718.

[30] Guiochon, G.; Drumm, E.; Cherrak, D. *J. Chromatogr. A* 1999, *835*, 41-58.

[31] Shalliker, R. A.; Broyles, B. S.; Guiochon, G. *J. Chromatogr. A* **2000**, *888*, 1-12.

[32] Shalliker, R. A.; Wong, V.; Broyles, B. S.; Guiochon, G. *J. Chromatogr. A* **2002**, *977*, 213-223.

[33] Chen, G.; Pačes, M.; Marek, M.; Zhang, Y.; Seidel-Morgenstern, A.; Tallarek, U. *Chem. Eng. Technol.* **2004**, *27*, 417-428.

[34] Vissers, J. P. C.; Claessens, H. A.; Laven, J.; Cramers, C. A. *Anal. Chem.* **1995**, *67*, 2103-2109.

[35] Tobis, J.; Vortmeyer, D. *Chem. Eng. Process.* **1991**, *29*, 147-153.

[36] Halász, I.; Martin, K. *Angew. Chem. Int. Ed.* **1978**, *17*, 901-908.

[37] Yau, W. W.; Kirkland, J. J.; Bly, D. D. *Modern Size-Exclusion Liquid Chromatography*, John Wiley & Sons, New York **1979**.

[38] Guan, H.; Guiochon, G. *J. Chromatogr. A* **1996**, *731*, 27-40.

[39] Carman, P. C. *Trans. Inst. Chem. Engrs.* **1937**, *15*, 150-166.

[40] Sonntag, G. *Chem.-Ing.-Tech.* **1960**, *32*, 317-329.

[41] Yang, R. Y.; Zou, R. P.; Yu, A. B. *Phys. Rev. E* **2000**, *62*, 3900-3908.

[42] Gritti, F.; Guiochon, G. *J. Chromatogr. A* **2007**, *1166*, 30-46.

[43] Billen, J.; Guillarme, D.; Rudaz, S.; Veuthey, J.-L.; Ritchie, H.; Grady, B.; Desmet, G. *J. Chromatogr. A* **2007**, *1161*, 224-233.

Chapter 3 - Determination of the interparticle void volume in packed beds via intraparticle Donnan exclusion

1. Introduction

The measurement and meaning of void volumes in reversed-phase liquid chromatography (RPLC) has been the subject of a considerable number of publications, as reviewed a few years ago by Rimmer et al. [1] and, consequently, has been studied extensively from theoretical and experimental point of views [2]. The total volume of a particle-packed RPLC column can be written as the sum of three contributions: (i) the interparticle, interstitial, or external pore volume; (ii) the intraparticle or internal pore volume; and (iii) the unaccessible volume which can be split into the stationary-phase solid volume, the closed-pore volume, and the volume of the bonded chains [3]. The different void volumes of a packed column are important in both kinetic and thermodynamic measurements, particularly when attempts are made to correlate solute retention with solvent composition [4, 5].

In this work we are concerned with the interparticle void volume (V_{inter}) and porosity (ε_{inter}). Its accurate determination and the corresponding analysis of packing densities provides essential feedback, e.g., during the optimization of column packing conditions and dynamic bed consolidation [6-9], or in the discussion of hydraulic permeabilities via phenomenological models and so-derived correlations [10]. This is reflected in the strong dependence on ε_{inter} of different porosity functions that have been used to characterize the resistance to low Reynolds number flow of liquid through packed beds, including the most popular one $(1 - \varepsilon_{inter})^2/\varepsilon_{inter}^3$ after Blake, Kozeny, and Carman, or $4(1 - \varepsilon_{inter})\varepsilon_{inter}^{-4.55}$ after Rumpf and Gupte which appears to be more accurate [11].

Traditionally, V_{inter} (and ε_{inter}) in packed beds are analyzed by inverse size-exclusion chromatography (ISEC) [12]. While classical SEC uses the known pore structure of an adsorbent to determine the molecular weight distribution of a polymer mixture [13], the pore-size distribution of an unknown stationary phase can be determined from the distribution of retention volumes of a series of polymer standards if their molecular weight is known. Provided that standard samples are available for calibration, experiments show that there

exists a correlation between the average molecular weight of the polymers and average diameter of the pores from which they are excluded, assuming that all polymeric chains remain in the same conformation of a random coil [13]. For each packing material, there are two thresholds, a low and a high one. Molecules larger than the high threshold have no access to any significant fraction of the intraparticle porosity. Molecules smaller than the low threshold have access to the entire pore volume. In ISEC solutions of known polymeric samples are injected into a column packed with an unknown adsorbent, and the retention behavior of these solutes can be correlated with the pore size distribution of the packing material [3, 12]. Plots of the logarithm of the molecular weight of the polystyrenes versus their retention time reveal a bimodal pore-size distribution representing the internal (intraparticle) and external (interparticle) porosity of the packed bed.

To overcome drawbacks of ISEC for the analysis of V_{inter} (and ε_{inter}) in packed beds [14] Cabooter et al. [15] recently presented a method that relies on measuring the elution time of an unretained small tracer after having filled the intraparticle pores of the particles with a hydrophobic solvent that is completely immiscible with the mobile phase employed during the elution time measurements. Thus, based on the total blocking of the intraparticle pores in a packed bed it allows to perform interparticle void volume measurements with a single, small tracer rather than a large polymer standard. While the total pore blocking method requires careful, time-consuming pretreatment of the materials, it does not need the regression analysis underlying ISEC.

Another and at least as accurate, but far simpler method than total pore blocking and ISEC for the analysis of V_{inter} (and ε_{inter}) in packed beds is based on the interparticle elution of organic or inorganic ions which are completely, but in this case electrostatically exluded from the intraparticle pore space due to the Donnan potential [16-18]. This approach originates as a limiting variant of the much explored use of organic or inorganic ions as dead time markers in RPLC (see Chapter 4.3 in [1] and references therein). In this context, it has been noted that mobile phases and/or samples with sufficient ionic strength are required to effectively screen the surface charges of the intraparticle pores and prevent Donnan exclusion of the charged dead time markers (which behave co-ionic with respect to the surface charge). As, towards the opposite electrostatic extreme, mobile phase composition is tuned for complete intraparticle Donnan exclusion a small, unretained, co-ionic tracer permeates through the interparticle void space only. It allows the fast, noninvasive analysis of V_{inter} (and ε_{inter}) using water-soluble, UV-detectable ions such as nitrate.

The use of simple organic or inorganic ions as selective markers for V_{inter} (and ε_{inter}) in packed beds based on the intraparticle Donnan exclusion has been observed and explored before [4, 14, 17, 19-23]. In this work, we present further insight into the operational domain of this simple as elegant approach by addressing, together with a variation of the mobile

phase ionic strength, the influence of the intraparticle mean pore size and surface charge density, as well as the onset of Donnan exclusion already on the interparticle pore level in dependence of the mean particle size. Values of ε_{inter} are compared with those obtained by the traditional ISEC method.

2. Background

In porous adsorbents like membranes, sphere packings, and monoliths which contain charged solid-liquid interfaces and through which ionic species (simple ions, analytes, or colloidal particles) are transported, several electrical fields may be superimposed. This includes local fields near the wall of charged pores, or around devised spacer groups and bonded chains which extend from the surface, the Donnan potentials between different compartments in hierarchically structured materials, the quasi-equilibrium electrical double layer (EDL) at the phase boundaries, as well as externally applied fields [18, 24].

Ion-permselectivity (charge-selectivity) is a unique and often tailored characteristic of porous media which they can show either as a whole (e.g., membranes separating completely adjacent solutions) or by means of local, discrete ion-permselective regions (meso- and/or microporous domains) in materials which are macroscopically charge-nonselective (packed beds, monoliths). While charge-selectivity traditionally plays a central role in membrane science [25, 26], ion-permselective transport also prevails in the intraparticle or intraskeleton mesopores of particulate and monolithic columns typically used in HPLC (Figure 1) [17, 18]. It is therefore also relevant to reversed-phase silica particles, even those with a conventional endcapping, due to the persistence of residual silanol groups which, in turn, contribute a pH-dependent surface charge [27].

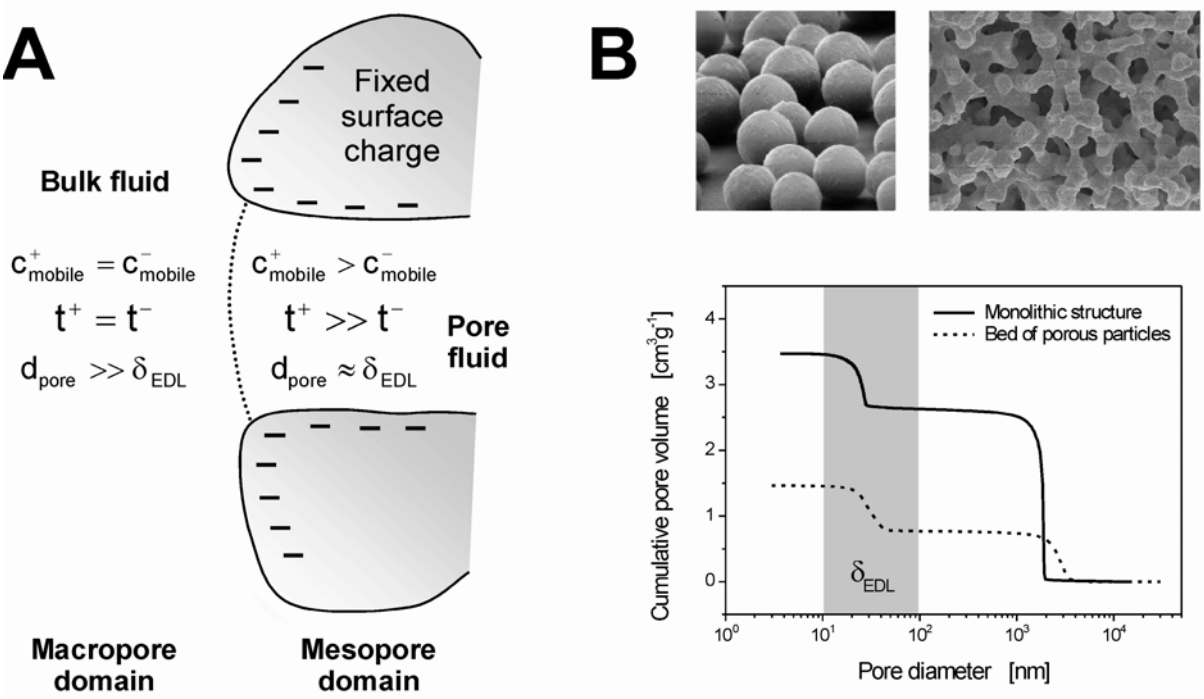

Figure 1: (A) Schematic representation of equilibrium ion concentrations (for a strong, symmetrical background electrolyte), transport numbers, and the ratio of the local pore diameter (d_{pore}) to the EDL thickness (δ_{EDL}) in the interconnected macropore and mesopore spatial domains of hierarchically structured materials. The concentration of mobile counterions (c^+_{mobile}) and their transport number (z^+t^+; t^+) is the transference number [16]) in the pore fluid of the mesopore domain exceed those of the co-ions. (B) SEM (scanning electron microscopy) images and pore size distributions characterizing many sphere packings and monolithic structures. These fixed beds reveal bimodal pore size distributions due to the intraparticle (intraskeleton) mesopores and the interparticle (interskeleton) macropores. Reprinted with permission from Leinweber et al. [24].

The characteristic pore sizes d_{pore} of the interparticle (interskeleton) macropore space of a packed bed (monolith) usually substantially exceed the typical EDL thickness δ_{EDL} at the particles external surface (along the monolith skeleton), as illustrated in Figure 1A (d_{pore} » δ_{EDL}). Thus, liquid in the macropore space is quasi-electroneutral (thin-EDL-limit) and transport numbers of the co-ions and counterions in the background electrolyte are well balanced. By contrast, intraparticle or intraskeleton mesopore sizes are comparable with the EDL thickness (Figure 1A, $d_{pore} \approx \delta_{EDL}$), as shown in Figure 1B for a representative silica-based monolith and a packed bed [24]. The mesopore-scale EDL interaction (also referred to as EDL overlap) results in counterion enrichment and co-ion exclusion with respect to the bulk solution. As illustrated in Figure 2 it is governed by the surface electrical potential inside the mesopores (ψ_S) and r_{pore}/λ_D, the ratio of the intraparticle or intraskeleton mesopore radius r_{pore} (if we assume cylindrical pores for simplicity) and the Debye screening length λ_D which characterizes the EDL thickness and which depends on the mobile phase ionic strength according to [28]

$$\lambda_D = \left(\frac{\varepsilon_0 \varepsilon_r RT}{F^2 \sum z_i^2 c_{i,\infty}} \right)^{\frac{1}{2}}, \qquad (1)$$

where ε_0 and ε_r are the permittivity of vacuum and relative permittivity of the bulk solution, respectively. R is the gas constant, T is the absolute temperature, and F is the Faraday constant; z_i is the valency of ionic species i and $c_{i,\infty}$ its concentration in the electroneutral, bulk solution (that is, beyond the EDL).

Depending on the actual intensity of EDL overlap, e.g., inside mesoporous particles of a packed bed represented by r_{pore}/λ_D, we expect the complete permeation ($\varepsilon_{tracer} = \varepsilon_{total}$) and exclusion ($\varepsilon_{tracer} = \varepsilon_{inter}$ only) of an unretained, co-ionic tracer as the extreme scenarios (Figure 2) [17, 19, 20, 23]. For $r_{pore}/\lambda_D \approx 1$, the EDL extends over the whole pore fluid, the pore is ion-permselective and excludes co-ions. Their transport numbers decrease at increasing EDL overlap, while those of the counterions increase. For $r_{pore} \gg \lambda_D$, the EDL is confined to a thin layer at the pore walls only, meaning that the whole pore fluid is quasi-electroneutral and its charge-selectivity disappears. The transport numbers of co-ions and counterions become balanced. These extremes ($r_{pore}/\lambda_D < 1$ and $r_{pore}/\lambda_D \gg 1$) and the broad intermediate regime can be easily tuned in chromatographic practice by the mobile phase ionic strength ($\rightarrow \lambda_D$) and the intraparticle pore dimensions ($\rightarrow d_{pore}$). Apart from the ion-exclusion chromatography, this adjustable electrostatic on-off behaviour [18, 29-34] of the intraparticle permeation in chromatographic media (Figure 2) is relevant also for the design of preparative separations and purification processes [35-37], because the actual electrolyte concentration determines the availability of chromatographic sites and “effective porosity“ for co-ionic analytes, as well as the pore-level concentrations of charged analytes (co-ion exclusion, counterion enrichment), in general.

Alternatively, the situation illustrated by Figures 1 and 2 can be analyzed in terms of Donnan exclusion [16]. At electrochemical equilibrium between electrolyte solutions in both compartments (Figure 1A) counterion concentration in the intraparticle (intraskeleton) mesopore space is higher and co-ion concentration lower than in the interparticle (interskeleton) macropore space. An electrical phase boundary potential between interconnected bulk and ion-permselective domains balances the tendency of ions to level out these concentration (chemical potential) differences. This potential is also known as the Donnan potential (Φ_{Don}) [38, 39]. It pulls cations back into the negatively charged intraparticle (intraskeleton) pore space and anions back into the positively charged interparticle (interskeleton) compartment [40]. For ideal solutions we have

$$\Phi_{Don} \equiv \phi_{intra} - \phi_{inter} = -\frac{RT}{z_i F} \ln \frac{c_{i,intra}}{c_{i,inter}}, \qquad (2)$$

where *i* applies to $TrisH^+$, H_3O^+, and K^+ (z_i = +1) as well as to Cl^-, OH^-, and NO_3^- (z_i = –1) for the buffer (Tris-HCl) and tracer salt (KNO_3) used in the present work. The distribution coefficient $c_{i,intra}/c_{i,inter}$ (which represents the ion-permselectivity of the particles or the monolith skeleton) depends on the mobile phase ionic strength, the surface charge density in the intraparticle or intraskeleton pore space, and on valencies of the co-ionic and counterionic species. Actually, these parameters similarly influence EDL overlap and resulting co-ion exclusion in a double-layer model.

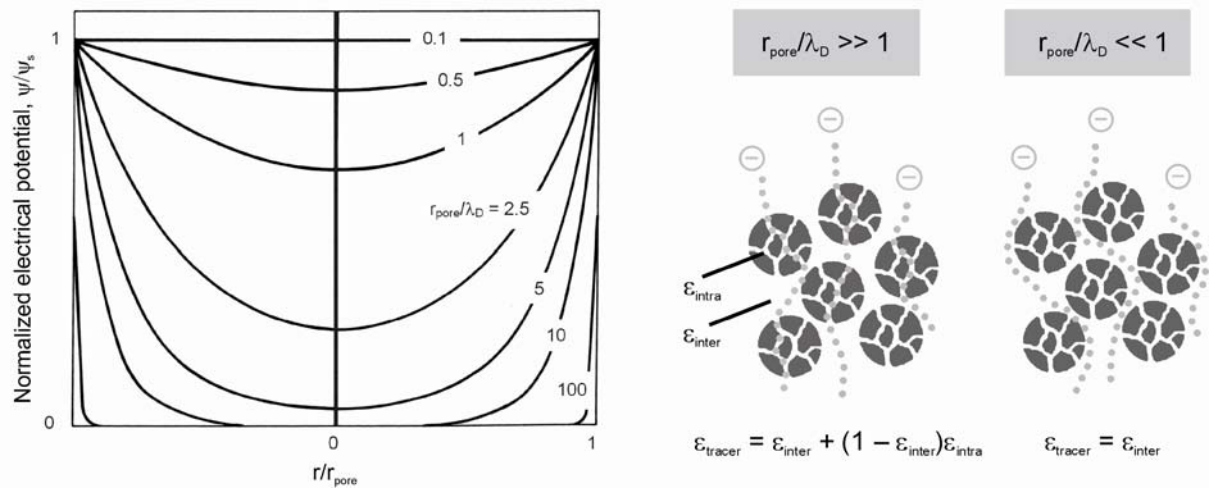

Figure 2: Pore-scale distribution of electrical potential normalized by the surface potential ψ_S for different values of r_{pore}/λ_D reflecting EDL overlap and co-ion exclusion (adapted from [28]). For r_{pore}/λ_D >> 1 a co-ionic (here negatively charged) tracer has access to the total porosity of the packed bed, while for r_{pore}/λ_D << 1 it samples only the interparticle porosity. Plots of the elution volumes of a co-ionic tracer versus r_{pore}/λ_D reveal a bimodal pore-size distribution with a plateau region at low ionic strength representing the interparticle porosity and another plateau region at high ionic strength where the charge-selectivity of the particles has disappeared and the co-ionic tracer experiences the entire pore space.

The considerations on relevant parameters (Figures 1 and 2) which define the operational domain of co-ion exclusion and inorganic ions as selective markers for V_{inter} (and ε_{inter}) in packed beds have motivated us to conduct the following capillary HPLC experiments. For an extended range of mobile phase ionic strengths (Tris-HCl buffer) and with KNO_3 as the tracer salt we compared particles with similar intraparticle mean pore sizes, but different surface charge densities (reversed-phase, bare silica, strong cation-exchange); particles with different intraparticle pore sizes (100 and 1000 Å); as well as different mean particle sizes (3, 5, and 10 µm) to retrieve Donnan exclusion not only inside, but already between the particles.

3. Experimental

3.1. Chemicals and materials

Organic solvents of HPLC grade (acetonitrile, methylene chloride, methanol, ethanol, and acetone) were purchased from Sigma-Aldrich (Taufkirchen, Germany). Benzene and KNO_3 were obtained from Carl Roth (Karlsruhe, Germany). Hydrochloric acid was bought from VWR International (Briare, France). Polystyrene standards with a molecular weight of 2500, 5000, 9000, 30000 and 50000 g/mol were purchased from Supelco (Bellefonte, PA). Polystyrene standards with 20000, 100000, 500000, 1000000, 2000000, and 4000000 g/mol as well as Tris(hydroxymethyl)-aminomethane came from Fluka Chemie (Buchs, Switzerland). HPLC-grade water was prepared with a Milli-Q gradient water purification system (Millipore, Bedford, MA).

In our capillary HPLC studies we employed the following support particles: 3 and 10 µm-sized 120 Å Hypersil MOS (monomeric octyl silica, C8) (Thermo Fisher Scientific, Waltham, MA); 3 µm-sized 80 Å Spherisorb SCX (propanesulfonic acid-modified silica) (Waters, Milford, MA); and 5 µm-sized 100 Å and 1000 Å Nucleosil 100-5 and Nucleosil 1000-5 (bare silica) (Macherey-Nagel, Düren, Germany). These particles were slurry-packed into 75 µm i.d., 360 µm o.d. cylindrical fused-silica capillaries (Polymicro Technologies, Phoenix, AZ).

3.2. Apparatus

All data were acquired with an Agilent 1100 liquid chromatograph (Agilent Technologies, Waldbronn, Germany) consisting of a degasser and a nanopump, equipped with a variable wavelength UV detector (VWD) and a high-sensitivity cell (SunChrom, Friedrichsdorf, Germany) working at 254 nm for the ISEC experiments with the polystyrene standards and at 210 nm for the Donnan exclusion experiments with KNO_3. Manual sample injection was performed via a two-position injection valve with a 4 nl internal loop volume (Model CN4 from Vici AG Valco Europe, Schenkon, Switzerland). The loop was continuously flushed by use of a syringe installed on a syringe pump (Harvard Apparatus, Holliston, MA). Fused-silica restriction capillaries having a length of either 900 mm (15 µm i.d.) or 500 mm (10 µm i.d.) were used as pre-columns to ensure a sufficient working pressure. Volumetric flow rates were continuously monitored by an external flow sensor (Model SLG-1430-150, Sensirion, Stäfa, Switzerland) connected to the outlet of the detection cell. To avoid daily fluctuations of the nanopump the actual flow rates recorded by the external flow sensor were

used to calculate elution volumes of the analytes. All experiments were carried out at 298 ± 1 K under isocratic elution conditions. Injections were thrice-repeated for a given capillary and the results averaged to account for the error from manual injection.

3.3. Capillary packing

Capillaries were slurry-packed using a WellChrom K-1900 pneumatic pump (Knauer, Berlin, Germany) with a 500 µm i.d. glass-lined metal tubing as the slurry reservoir [8, 41]. A micro-union with a 1 µm mesh stainless-steel frit (Upchurch Scientific, Oak Harbor, WA) was connected to each capillary to provide a temporary outlet frit during packing. Slurries were prepared by suspending the dry particles in 1 ml of the appropriate solvent while applying ultrasound for 10 min (Table 1).

The degassed pushing (packing) solvents were also used for rinsing and conditioning of the fused-silica capillaries prior to the packing process. 70 µl of the slurries were injected into the reservoir and a pressure of 300 bar was applied for at least 5 min. After a short optical inspection to verify whether the packing of the capillary had started or blockage occurred, the pressure was raised (Table 1) and the capillaries were inserted into an ultrasonic bath (Bandelin Electronic, Berlin, Germany) for 40 min during packing and consolidation. As demonstrated earlier the application of ultrasound appeared to be critical for obtaining densely packed capillaries [8].

After consolidation of the packing, the system was depressurized slowly and the capillary removed from the packing device. The pushing solvent was replaced by bidistilled, filtered, and degassed water containing NaCl which was needed for preparing mechanically stable frits (Table 1). Afterwards, the capillary was reassembled within the packing device and flushed for 90 min with the aqueous electrolyte solution for a complete exchange of the packing solvent. The bed was fixed by a sintered inlet and outlet frit to obtain a total bed length of about 120 mm. Packing procedures were not evaluated for separation efficiencies; the conditions in Table 1 proved to be adequate for obtaining stable packed beds without gaps and further tendency for settling during the measurements.

Table 1: Packing conditions for the adsorbents.

Packing material	Slurry solvent	Slurry concentration	Packing solvent	Max. applied pressure	Fritting electrolyte
Hypersil MOS; 3 µm, 120 Å	Acetone	20 mg/ml	Methanol	550 bar	1 g/l NaCl
Hypersil MOS; 10 µm, 120 Å	Acetone	20 mg/ml	Methanol	550 bar	1 g/l NaCl
Spherisorb SCX; 3 µm, 80 Å	1 M NaCl	10 mg/ml	2 M NaCl	550 bar	30 g/l NaCl
Nucleosil; 5 µm, 100 Å	Ethanol	35 mg/ml	Water	400 bar	1 g/l NaCl
Nucleosil; 5 µm, 1000 Å	Ethanol	15 mg/ml	Water	300 bar	1 g/l NaCl

3.4. Porosity measurements

Interparticle void volumes and porosities (V_{inter} and ε_{inter}) of the packed capillaries were analyzed by ISEC (size exclusion) and Donnan (electrostatic) exclusion. In the former case benzene (1 mmol/l) and a total of eleven polystyrene standards ranging from 2500 to 4000000 g/mol (0.6 mg/ml each) were dissolved in methylene chloride. Analytes were injected and chromatographed at a flow rate of 200 nl/min and detection at 254 nm. For the determination of V_{inter} and $\square_{inter}$ via Donnan exclusion in capillaries packed with the Hypersil MOS phases KNO_3 in 70/30 acetonitrile/water (v/v) was injected and detected at 210 nm. For the bare silica and SCX materials KNO_3 was used in 30/70 acetonitrile/water (v/v). The concentration of Tris-HCl buffer (pH 8.1) in the mobile phases was varied from 0.01 to 40 mM and is, where useful, also presented as λ_D (the Debye screening length, Eq. (1)) to express the Donnan exclusion of nitrate also via r_{pore}/λ_D (cf. Figure 2). The relative permittivity (ε_r) in Eq. (1) for the mobile phases was taken from Moreau and Douhéret [42].

For low buffer concentrations in the running mobile phase (from 0.01 to 0.1 mM) KNO_3 solutions in the respective, but unbuffered mobile phase were injected. In this case, the KNO_3 concentration was adjusted to the ionic strength of the runing mobile phase which resulted in negligible disturbances of the intraparticle Donnan exclusion during elution of the nitrate due to the mismatch between injected sample and running mobile phase. At higher

buffer concentrations (> 0.1 mM) a fixed KNO_3 concentration of 0.04 mM was added to the respective and now buffered mobile phase for sample injection.

4. Results and Discussion

Interparticle void volumes and porosities (V_{inter} and ε_{inter}) have been determined by ISEC and Donnan exclusion for all packings. In ISEC eleven polystyrene standards with molecular weights (M_W) from 2500 to 4000000 g/mol and benzene dissolved in methylene chloride were injected onto the packed capillaries for each packing material. Interparticle porosities ($\varepsilon_{inter} = V_{PS}/V_{column}$) were calculated from the elution volumes of the most suitable standard (V_{PS}), which is just size-excluded from the intraparticle pore space, and the geometrical column volume (V_{column}). The latter has been determined by measuring nitrate elution volumes for the empty capillaries that were subsequently used for packing.

Plots of $\log(M_W)$ of the polystyrene standards vs. their elution volume revealed a bimodal pore size distribution for all packings (only for capillaries packed with macroporous Nucleosil 1000-5 material the determination of the high threshold was not unambiguous, as discussed later). The intersection of the calibration curves providing the smallest polystyrene coil which is completely excluded from the intraparticle pore space was determined graphically by linear regression. The associated pore diameter of each stationary phase was calculated by [12]

$$d_{pore}\left(\text{Å}\right) = 0.62\left(M_W\right)^{0.59} \tag{3}$$

and values are summarized in Table 2. As pointed out [12], d_{pore} assigned by a polystyrene standard of molecular weight M_W (Eq. (3)) is 2.5 times as large as the coil diameter of molecules of the same polystyrene. In other words, rotational coil diameters must be some 2.5 times smaller than the diameter of the pores to allow the polymer unhindered access to the pores. When comparing the results in Table 2 with manufacturers' data slight differences are resolved for Hypersil MOS and Spherisorb SCX particles. For Nucleosil 100-5 particles, however, the calculated pore diameter turned out to be significantly higher (162 Å instead of the nominal 100 Å); similarly, the 2000000 g/mol polystyrene standard denotes d_{pore} = 1295 Å for the Nucleosil 1000-5 particles (nominal d_{pore}: 1000 Å).

Table 2: Characteristics of the packed capillaries.

Material	d_{pore} [Å]	ε_{inter} (NO_3^-)	ε_{inter} (PS)
Hypersil MOS; 3 µm, 120 Å	110	n.a.	0.36
Hypersil MOS; 10 µm, 120 Å	119	0.42	0.41
Spherisorb SCX; 3 µm, 80 Å	95	0.42	0.43
Nucleosil; 5 µm, 100 Å	162	0.43	0.44
Nucleosil; 5µm, 1000 Å	1295	< 0.49	n.a.

Interparticle porosities determined by Donnan exclusion were calculated from the nitrate elution volumes at a buffer concentration of 0.02 mM, where elution volumes (V_{tracer}) for most packings reached the plateau region (see below) indicating complete intraparticle Donnan exclusion, and the geometrical column volume (V_{column}). To realize maximum surface charge of all packing materials the aqueous part of all mobile phases was buffered with Tris-HCl (pH 8.1). This caused a complete dissociation of silanol groups on the surface of the bare silica, reversed-phase silica, and SCX particles.

Interparticle porosities are summarized in Table 2 and show good agreement between the two methods (ISEC and Donnan exclusion). Packing densities for the Hypersil MOS phases with ε_{inter} = 0.36 for the 3 µm and ε_{inter} = 0.41-0.42 for the 10 µm particles at a particle-aspect ratio (column-to-particle diameter ratio) of d_c/d_p = 25 and 7.5, respectively, agree with the trend in earlier investigations where the packing density of confined cylindrical sphere packings was found to decrease exponentially at low particle-aspect ratios due to the increasing contribution of the geometrical wall effect [8, 43]. The value of ε_{inter} = 0.36 realized with the 3 µm Hypersil MOS particles closely reflects the maximum density of disordered (random) hard sphere packings [44, 45]. Nucleosil bare silica particles were packed at lower pressures to avoid damage of the highly porous particle structure (Table 1). The application of high packing pressures turned out to be essential for generation of densely packed beds, thus the lower packing pressures limited by the stability of the Nucleosil material explain the slightly higher porosities of Nucleosil 100-5 (ε_{inter} = 0.43-0.44) and Nucleosil 1000-5 (ε_{inter} < 0.49) packings. Additionally, the Nucleosil particles show a stronger deviation from spherical

shape and higher surface roughness than the other materials which also contributes to lower packing densities [8, 46].

Despite these obvious differences in packing densities all packings were consolidated, rigid, and therefore met the requirements for a reliable data acquisition by chromatographic measurements of the interparticle void volumes. Careful microscopic inspection revealed that all packings remained densely packed; no voids were observed in the axial direction before and after the chromatographic analysis.

4.1. Effect of the mean particle size

Figure 3 shows the calibration curves for electrostatic exclusion (Figure 3A) and size-exclusion (Figure 3B) acquired with the Hypersil MOS particles (120 Å nominal pore size). Comparing the calibration curves for the two differently sized materials (d_p = 3 and 10 µm nominal particle size) it is first noticed that both size-exclusion and Donnan exclusion with the 10 µm particles develop relatively discretely. Complete Donnan exclusion in Figure 3A (open circles) is characterized by the plateau region at low buffer concentrations where the normalized elution volumes V_{tracer}/V_{column} are plotted versus the dimensionless ratio r_{pore}/λ_D characterizing intraparticle EDL overlap (or Donnan exclusion). In this plateau region nitrate is completely excluded from the negatively charged intraparticle pore space (thus, $V_{tracer} \equiv V_{inter}$). This exclusion persists up to r_{pore}/λ_D = 0.12 (which translates to a Tris buffer concentration of 0.04 mM) and these "plateau" elution volumes can be used for calculating the interparticle porosity according to $\varepsilon_{inter} = V_{inter}/V_{column}$. At higher ionic strength nitrate ions begin to penetrate the intraparticle pore space (and $V_{tracer} > V_{inter}$). The hyperbolic shape of the graph in Figure 3A (open circles) results from the inverse dependence of λ_D on the square root of the counterion concentration (Eq. (1)), so that the electrostatic (Donnan) exclusion is only slowly developing (or disappearing) over a wide range of mobile phase ionic strengths. At the highest buffer concentration (40 mM) the nitrate ions are still not able to penetrate the complete pore space; otherwise, the elution volumes would reach a second plateau (where $V_{tracer} \equiv V_{total}$). This illustrates that relatively high ionic strengths need to be realized in order to use the nitrate ions as a tracer for the column dead volume [1, 17]. The size-exclusion curve for the 10 µm Hypersil MOS particles (Figure 3B, open circles) reveals a bimodal distribution. Benzene has access to the entire pore space and it therefore denotes the overall void volume of the packing. Complete size-exclusion is reached with the polystyrene standard of 50000 g/mol. At increasing molecular weight M_W of the polystyrene standards a sharp increase in $V_{PS}/V_{Benzene}$ with a nearly vertical calibration curve is observed.

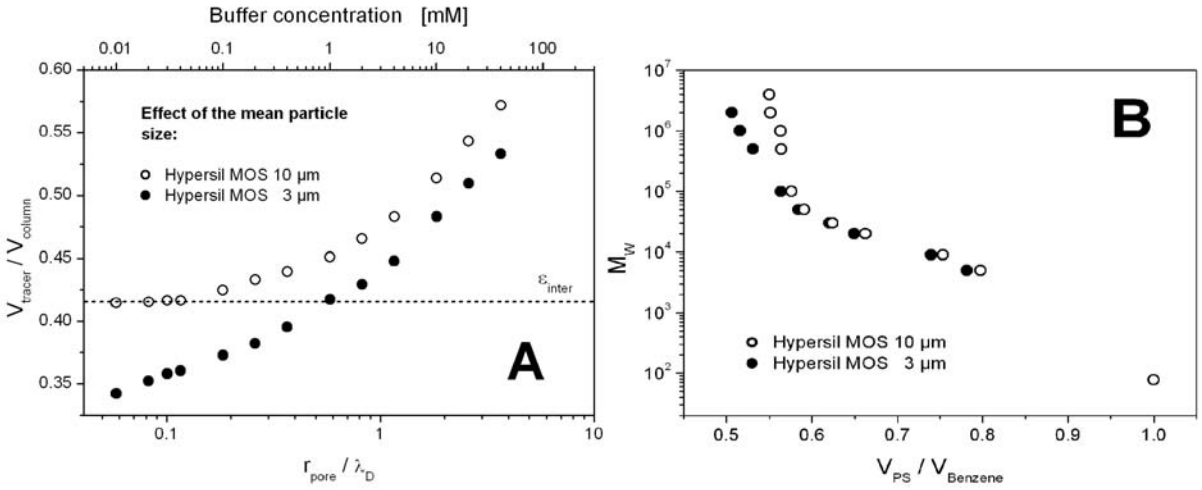

Figure 3: (A) Electrostatic exclusion curves of nitrate vs. r_{pore}/λ_D and (B) inverse size-exclusion curves of polystyrene standards with known molecular weight (M_W) for capillaries packed with the 3 and 10 µm-sized Hypersil MOS particles (120 Å nominal pore size). The elution volumes of nitrate (V_{tracer}) were normalized by the empty capillary volume (V_{column}), while polystyrene elution volumes (V_{PS}) were normalized by that of benzene.

Calibration curves for electrostatic and size-exclusion in the case of capillaries packed with the smaller (3 µm-sized) Hypersil MOS particles reveal a different trend. The Donnan exclusion curve in Figure 3A at high ionic strengths (and, correspondingly, high values of r_{pore}/λ_D) is similar to the calibration data for the 10 µm particles with a nearly identical surface chemistry and pore size distribution; however, at decreasing ionic strength (and decreasing r_{pore}/λ_D) V_{tracer}/V_{column} does not enter into a plateau region. Instead, the nitrate elution volumes continue to decrease. To explain this behavior, another aspect of packing morphology needs to be considered. Compared with the d_p = 3 µm packings the 10 µm packings not only consist of larger particles (translating to a larger d_p/λ_D ratio), but they are also more loosely packed (cf. Table 2). The mean nearest-neighbor distance in random sphere packings depends on the packing density [47]. As a result (concerning absolute particle size and packing density), significant EDL overlap does not develop between the loosely packed 10 µm particles, even as the EDL thickness continues to increase at decreasing buffer concentration. By contrast, EDL overlap in the interparticle pore space becomes important for the densely packed 3 µm packings and explains the continued decrease in nitrate elution volumes at decreasing r_{pore}/λ_D (without entering a plateau). In other words, while still increasingly exluded from the intraparticle pore space the nitrate ions already become partly excluded from the interparticle pore space as well.

The importance of the interparticle pore space dimensions is also reflected in the ISEC graphs (Figure 3B), but now in view of size-exclusion, not electrostatic exclusion. For the 3 µm packings the high-molecular-weight polystyrenes do not demonstrate the theoretically expected vertical distribution of elution data ($V_{PS}/V_{Benzene}$) for completely size-

excluded polystyrene standards, as observed almost for the 10 µm packings. The significantly smaller slope for the 3 µm packings can be explained by the onset of size-exclusion from the interparticle pore space already where these polystyrenes are unable to fully penetrate the cusp regions between the small (and densely packed) 3 µm particles.

4.2. Effect of the surface charge density

To study the influence of the intraparticle surface charge density on Donnan exclusion nitrate elution curves for the 3 µm Hypersil MOS particles and 3 µm Spherisorb SCX particles are compared in Figure 4A. Both particles have similar intraparticle pore sizes (110 and 95 Å, Table 2), but their surface modification is very different. Hypersil MOS is a dimethyloctylsilane non-endcapped silica, whereas the Spherisorb SCX is a propanesulfonic acid-modified silica. By comparing calibration curves in Figure 4A, where normalized elution volumes of nitrate ions are plotted vs. the Tris buffer concentration, we notice that V_{tracer}/V_{column} for the Hypersil MOS particles decreases monotonically with decreasing ionic strength, while elution volumes on the Spherisorb SCX material run into a plateau below a buffer concentration of 0.1 mM. The discrete Donnan exclusion regime with a fully developed pleateau can be explained by the significantly higher surface charge density of the Spherisorb SCX particles. This property leads to a much stronger Donnan exclusion of the nitrate ions, in turn enabling the observation of a discrete plateau region (Figure 4A).

Figure 4B shows the results of the ISEC calibration. Both curve shapes in this case are similar, in contrast to Figure 4A, because size-exclusion of the larger polystyrene standards from parts of the interparticle pore space is independent of the surface charge density of the particles and is therefore similar for packing materials with a similar mean particle size and size distribution.

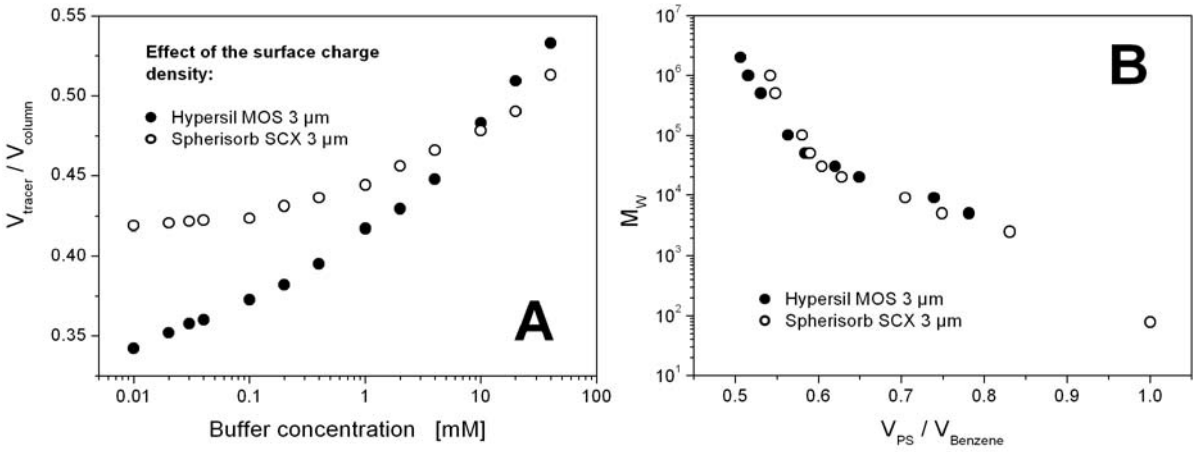

Figure 4: (A) Electrostatic exclusion curves of nitrate vs. the concentration of Tris-HCl buffer in the mobile phase and (B) inverse size-exclusion curves of polystyrene standards with known molecular weight (M_W) for capillaries packed with 3 µm Hypersil MOS (monomeric octyl silica, non-endcapped) and 3 µm Spherisorb SCX (propanesulfonic acid-modified silica) particles.

4.3. Effect of the mean intraparticle pore size

Intraparticle co-ion exclusion for a packing material is expected to depend sensitively on the mean pore size, i.e., the actual pore-scale EDL overlap expressed in r_{pore}/λ_D (Figure 2), assuming that the particle size (cf. Figure 3) and the surface potential (cf. Figure 4) of the stationary phases are identical. To demonstrate the influence of r_{pore} in r_{pore}/λ_D, the calibration curves for packed capillaries obtained with Nucleosil 100-5 (5 µm-sized particles, nominal 100 Å pores) and Nucleosil 1000-5 (nominal 1000 Å pores) are shown in Figure 5A. The surface charge density of these Nucleosil bare silica particles is higher than that of the Hypersil MOS reversed-phase particles, which leads us to predict a more pronounced plateau region in the Donnan exclusion data for the Nucleosil 100-5 particles (open circles, Figure 5A) compared to the 10 µm Hypersil MOS particles (open circles, Figure 3A). This is indeed confirmed by the experimental data when comparing the slopes of both curves at low buffer concentrations. The asymptotic limit of intraparticle exclusion is almost reached at r_{pore}/λ_D = 0.21 for Nucleosil 100-5 (Figure 5A), whereas for 3 µm Hypersil MOS (Figure 3A) the nitrate ions at this ratio still are not completely excluded. The higher surface electrical potential in the even slightly larger pores of the bare silica (162 Å) compared to the C8-silica material (119 Å) results in a stronger Donnan exclusion.

In a comparison of columns packed with the Nucleosil 100-5 (162 Å pores, Table 2) and Nucleosil 1000-5 (1295 Å pores) particles, the differences in Donnan exclusion are nearly independent of the surface electrical potential, but should reflect exclusively the

dependence on the mean pore diameter. The much smaller EDL overlap for the Nucleosil 1000-5 particles results in an immediately sharp increase in the V_{tracer}/V_{column} data of the Donnan exclusion curve at r_{pore}/λ_D = 0.63 (already with the low buffer concentrations), whereas the calibration curve of the Nucleosil 100-5 particles starts much earlier, at r_{pore}/λ_D = 0.07. An accurate determination of the point of complete exclusion from the intraparticle pore space cannot be made for the macroporous Nucleosil 1000-5 particles, because the nitrate elution volumes do not reach, but just approach the asymptotic limit (plateau region at still lower values of r_{pore}/λ_D indicating complete Donnan exclusion). Although the slope of the V_{tracer}/V_{column} data at buffer concentrations below 0.03 mM (r_{pore}/λ_D = 1.09) starts to decrease, the deviation of the calculated ε_{inter} = 0.49 (using the nitrate elution volume with 0.01 mM Tris) from the real packing density is difficult to estimate by extrapolation. Thus, the smallest nitrate elution volume for the macroporous particles at r_{pore}/λ_D = 0.63 (lowest Tris buffer concentration used) provides only an upper limit and $\varepsilon_{inter} < 0.49$.

Regarding the analysis of ISEC data for the small-pore and wide-pore silicas (Figure 5B) a discrete point of complete size-exclusion can be recognized only for the Nucleosil 100-5 particles (open circles) at a molecular weight of 100000 g/mol translating to the pore diameter of 162 Å in Table 2. For the Nucleosil 1000-5 particles, however, the opposite extreme can be observed: here, the pores are so large to become almost fully penetrated not only by benzene, but also the polystyrene standards with 2500 and 5000 g/mol. A significant size-exclusion from the pores starts with 9000 g/mol, i.e., for a pore diameter of 54 Å, and reaches the upper limit in this work at 4000000 g/mol (1948 Å). Although the point of complete size-exclusion can not be identified exactly, elution volumes of the 2000000 g/mol and 4000000 g/mol polystyrene standards are already slightly higher than expected from the linear fit to the data of intermediate-sized polystyrenes indicating the onset of size-exclusion from the interparticle pore space. Thus, the coil diameter of the 2000000 g/mol polystyrene standard (1295 Å) represents a more reliable pore diameter of the Nucleosil 1000-5 material.

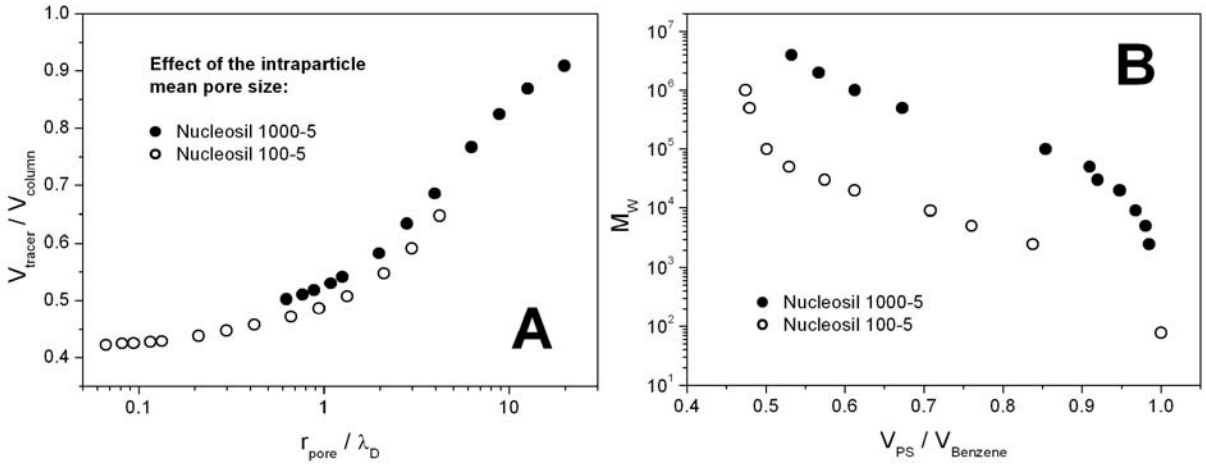

Figure 5: (A) Electrostatic exclusion curves of nitrate vs. r_{pore}/λ_D and (B) inverse size-exclusion curves of polystyrene standards with known molecular weight (M_W) for capillaries packed with 5 µm Nucleosil 100-5 (100 Å nominal pore size) and Nucleosil 1000-5 bare silica particles (1000 Å).

5. Conclusions

Interparticle void volumes (V_{inter}) and porosities (ε_{inter}) of particle-packed, 75 µm i.d. fused-silica capillaries have been determined by careful adjustment for complete intraparticle Donnan exclusion of a small, unretained, co-ionic tracer (nitrate ions). Electrostatic exclusion provides a theoretically clear, physically sharp definition of the boundary between (charge-selective) mesopore space and (charge-nonselective) macropore space in typical hierarchically structured porous media like packed beds and monoliths (Figure 1).

The operational domain of this approach has been studied for bare silica, reversed-phase, and strong cation-exchange materials with different particle sizes and intraparticle pore sizes. This allowed to realize a wide range of conditions under which this simple approach could be tested by analyzing – in combination with the mobile phase ionic strength (Tris-HCl buffer) – the intraparticle EDL overlap and co-ion exclusion (Figure 2) in dependence of the intraparticle pore size (Figure 5) and the surface charge density of the particles (Figure 4). For all investigated surface chemistries the intraparticle Donnan exclusion approach resulted in values of ε_{inter} that agreed well with those obtained independently by ISEC. Limitations to the use of Donnan exclusion (electrostatic exclusion) and ISEC (mechanical exclusion) arise as either type of exclusion becomes noticeable also in the cusp regions between the particles (Figure 3), or as the intraparticle pores are so large that complete electrostatic and size exclusion are difficult to realize (Figure 5).

Because mesoporous packing materials are common in HPLC and a sufficient surface charge density even exists on typical reversed-phase particles (Figure 3) Donnan

exlusion for the determination of ε_{inter} presents a most simple, fast, and reliable approach, with convenient mobile phases and detection. It thereby offers advantages compared to ISEC and it also shows that the total pore blocking of reversed-phase packings using a hydrophobic solvent [15] is redundant in most cases, particularly because Cabooter et al. [15] recommended the use of an inorganic salt like $NaNO_3$ or KI anyway as tracer for the determination of ε_{inter} after pore blocking. Our results confirm that the long-known "electrostatic pore blocking" [1] (using just the inorganic salt) is far easier, faster, and not limited by the surface chemistry.

References

[1] Rimmer, C.A.; Simmons, C.R.; Dorsey, J.G. *J. Chromatogr. A* **2002**, *965*, 219-232.

[2] Gritti, F.; Kazakevich, Y.; Guiochon, G. *J. Chromatogr. A 2007*, *1161*, 157-169.

[3] Guan, H.; Guiochon, G. *J. Chromatogr. A* **1996**, *731*, 27-40.

[4] Alhedai, A.; Martire, D.E.; Scott, R.P.W. *Analyst* **1989**, *114*, 869-875.

[5] Felinger, A.; Kele, M.; Guiochon, G. *J. Chromatogr. A* **2001**, *913*, 23-48.

[6] Guiochon, G.; Sarker, M. *J. Chromatogr. A* **1995**, *704*, 247-268.

[7] Koh, J.-H.; Broyles, B.S.; Guan-Sajonz, H.; Hu, M. Z.-C.; Guiochon, G. *J. Chromatogr. A* 1998, *813*, 223-238.

[8] Ehlert, S.; Rösler, T.; Tallarek, U. *J. Sep. Sci.* **2008**, *31*, 1719-1728.

[9] Ehlert, S.; Kraiczek, K.; Mora, J.-A.; Dittmann, M.; Rozing, G. P.; Tallarek, U. *Anal. Chem.* **2008**, *80*, 5945-5950.

[10] Dullien, F. A. L. *Porous Media – Fluid Transport and Pore Structure*. Academic Press, San Diego, **1991**.

[11] Rumpf, H.; Gupte, A.R. *Chem.-Ing.-Tech.* **1971**, *43*, 367-375.

[12] Halász, I.; Martin, K. *Angew. Chem. Int. Ed.* **1978**, *17*, 901-908.

[13] Yau, W.W.; Kirkland, J.J.; Bly, D.D. *Modern Size-Exclusion Liquid Chromatography.* John Wiley & Sons, New York, **1979**.

[14] Gritti, F.; Guiochon, G. *J. Chromatogr. A* 2006, *1136*, 192-201.

[15] Cabooter, D.; Lynen, F.; Sandra, P. Desmet, G. *J. Chromatogr. A* **2007**, *1157*, 131-141.

[16] Helfferich, F. *Ion Exchange*. McGraw-Hill, New York, **1962**.

[17] Nischang, I.; Chen, G.; Tallarek, U. *J. Chromatogr. A* **2006**, *1109*, 32-50.

[18] Höltzel, A.; Tallarek, U. *J. Sep. Sci.* **2007**, *30*, 1398-1419.

[19] Berendsen, G.E., Schoenmakers, P.J.; de Galan, L.; Vigh, G.; Varga-Puchony, Z.; Inczédy, J. *J. Liq. Chromatogr.* **1980**, *3*, 1669-1686.

[20] Wells, M.J.M.; Clark, C.R. Anal. Chem. 1981, 53, 1341-1345.
[21] Engelhardt, H.; Müller, H.; Dreyer, B. *Chromatographia* **1984**,*19*, 240-245.
[22] Shibukawa, M.; Ohta, N. *Chromatographia* **1988**, 25, 288-294.
[23] Daignault, L.G.; Jackman, D.C.; Rillema, D.P. *J. Chromatogr.* **1989**, *462*, 71-84.
[24] Leinweber, F.C.; Pfafferodt, M.; Seidel-Morgenstern, A. Tallarek, U. *Anal. Chem.* **2005**, *77*, 5839-5850.
[25] Sørensen, T.S. *(Ed.), Surface Chemistry and Electrochemistry of Membranes*. Marcel Dekker, New York, **1999**.
[26] Strathmann, H. *Ion Exchange Membrane Separation Processes*. Elsevier, Amsterdam, The Netherlands, **2004**.
[27] Melnikov, S.M.; Höltzel, A.; Seidel-Morgenstern, A.; Tallarek, U. *J. Phys. Chem. C* **2009**, *113*, 9230-9238.
[28] Probstein, R.F. *Physicochemical Hydrodynamics*. Wiley, New York, **1994**.
[29] Kemery, P.J.; Steehler, J.K.; Bohn, P.W. *Langmuir* **1998**, *14*, 2884-2889.
[30] Kuo, T.C.; Sloan, L.A.; Sweedler, J.V.; Bohn, P.W. *Langmuir* **2001**, *17*, 6298- 6303.
[31] Ku, J.R.; Stroeve, P. *Langmuir* **2004**, *20*, 2030-2032.
[32] Stein, D.; Kruithof, M.; Dekker, C. *Phys. Rev. Lett.* **2004**, *93*, 035901.
[33] Schmuhl, R.; Keizer, K.; van den Berg, A.; ten Elshof, J.E.; Blank, D.H.A. *J. Colloid Interface Sci.* **2004**, *273*, 331-338.
[34] Plecis, A.; Schoch, R.B.; Renaud, P. *Nano Lett.* **2005**, *5*, 1147-1155.
[35] Guiochon, G.; Golshan-Shirazi, S.; Katti, A.M. *Fundamentals of Preparative and Nonlinear Chromatography*. Academic Press, Boston, MA, **1994**.
[36] Pujar, N.S.; Zydney, A.L. *J. Chromatogr. A* **1998**, *796*, 229-238.
[37] Burns, D.B.; Zydney, A.L. *AIChE J.* **2001**, *47*, 1101-1114.
[38] Donnan, F.G. *Z. Elektrochem.* **1911**, *17*, 572-581.
[39] Donnan, F.G.; Guggenheim, E.A. *Z. Phys. Chem.* **1932**, *162*, 346-360.
[40] Ståhlberg, J. *J. Chromatogr. A* **1999**, *855*, 3-55.
[41] Chen, G.; Pačes, M.; Marek, M.; Zhang, Y.; Seidel-Morgenstern, A.; Tallarek, U. *Chem. Eng. Technol.* **2004**, *27*, 417-428.
[42] Moreau, C.; Douhéret, G. *J. Chem. Thermodyn.* **1976**, *8*, 403-410.
[43] de Klerk, A. *AIChE J.* **2003**, *49*, 2022-2029.
[44] Song, C.; Wang, P.; Makse, H.A. *Nature* **2008**, *453*, 629-632.
[45] Anikeenko, A.V.; Medvedev, N.N. *Phys. Rev. E* **2008**, *77*, 031101.
[46] Gritti, F.; Guiochon, G. J. Chromatogr. A 2007, 1166, 30-46.
[47] Torquato, S.; *Phys. Rev. Lett.* **1995**, *74*, 2156-2159.

Chapter 4 - Separation Efficiency of Particle-Packed HPLC-Microchips

1 Introduction

In recent years separation science has witnessed the development of high performance liquid chromatography (HPLC) at the nanoliter scale. This technological advance was initiated by the ever increasing demand for sensitivity in combination with on-line electrospray ionization mass spectrometric detection (HPLC-ESI/MS) [1-6]. Nano-ESI/MS, which refers to ESI performed at flow rates in the range of 200 to 1000 nL/min, produces smaller droplets than conventional ESI resulting in more efficient ionization. Benefits include greater sensitivity, enhanced dynamic range, and a reduced competition between analytes for ionization, establishing nano-HPLC/MS as a key technique in proteomics.

A current approach to this technique is microchip-HPLC, where a credit card-sized separation device contains all the functional elements for executing the demanding HPLC separations required in proteomics [7]. Contrary to the cylindrical fused-silica columns used in conventional nano-HPLC, the separation medium on HPLC-microchips is contained in a microfluidic channel. Such channels have been fabricated in silicon, glass, quartz, diamond, and a variety of polymeric materials. Their geometry is mainly determined by the fabrication methods used and usually noncylindrical. Cross-sections of microchip separation channels include semicircular, quadratic, rectangular, trapezoidal, and elliptical geometries, often with irregularly-angled corners and curved sides. Recent microchips [8-20] use either porous monoliths or slurry-packed particulate beds as separation media. The former have the advantage of easy fabrication by polymerization of the monolithic column directly in the microfluidic channel, while the latter are desirable if the wide range of available chromatographic media and the knowledge gained from conventional HPLC is to be utilized. An efficient alternative to the use of packed beds for microchip-HPLC separations may be provided by microfabricated, perfectly ordered pillar array columns [21-23].

For a broad acceptance of the microchip-HPLC technology beyond the proteomics community, the separation performance of HPLC-microchips should at least equal those of conventional column platforms. A central question that needs to be resolved is how the noncylindrical geometry of the separation channel influences the structure of the packed particulate bed and thus the overall chromatographic performance of the microfluidic chip. Axial dispersion in noncylindrical packings is expected to be affected by the corners of the

various conduit geometries which are absent in the classical cylindrical column format. The three-dimensional velocity field and hydrodynamic dispersion in pressure-driven flow through beds of spherical particles have been studied recently by quantitative numerical analysis for conduits with different cross-sectional geometries [24]. This analysis revealed two important aspects which influence hydrodynamic dispersion in noncylindrical compared to cylindrical packings: i) the presence of corners gives rise to the formation of channels of advanced fluid flow velocity, and ii) the reduced symmetry of noncylindrical packings leads to a longer characteristic length of the solute molecules for lateral equilibration between different velocities. These aspects effect that axial dispersion in noncylindrical packed beds becomes larger than in cylindrical ones of equal cross-sectional area. In addition, noncylindrical packings are much stronger affected by higher bed porosities than cylindrical ones, whereas at low bed porosities hydrodynamic dispersion comes close to that in cylindrical packings [24].

To corroborate the results from the numerical analysis, the current work presents an experimental investigation of separation efficiencies in microchip-HPLC. For this study, prototype HPLC-microchips with minimal dead volumes, a separation channel with trapezoidal cross-section, and on-chip UV-detection were used. Our equipment allowed to pack the microfluidic channels under pressures of up to 400 bar and ultrasonication. Bed densities (interparticle porosities) of the packed separation channels were investigated with respect to the packing process and correlated to the measured pressure drop and separation efficiencies under isocratic elution conditions. The performance of the microchips is finally compared to nanobore-HPLC columns packed with the same adsorbent particles, demonstrating comparable separation efficiencies for both platforms.

2 Experimental Section

2.1 Chemicals and materials

Organic solvents (acetonitrile, methylene chloride, methanol, tetrahydrofurane) and analytes (uracil, benzene, alkylbenzenes) were purchased from Sigma-Aldrich Chemie GmbH (Taufkirchen, Germany). HPLC grade water was prepared using a Milli-Q gradient water purification system (Millipore, Bedford, MA, USA). The packing material was 5 µm-sized Zorbax SB-C18 with a mean intraparticle pore size of 80 Å (Agilent Technologies, Waldbronn, Germany). Measurement of the size distribution provided a Sauter mean diameter of 5.51 ± 0.12 µm for these particles [25] which were slurry-packed into prototype HPLC/UV-microchips.

2.2 Microchip design and on-chip UV-detection

The prototype HPLC/UV-microchips consist of a three-layered, laminated polyimide design and integrate the following three operational elements: injection, separation, and detection (Figure 1). For sample injection the microchips were connected to a face-seal rotary valve with a 0.7 nL internal loop between ports 1 and 4. Each port contributed another 2.2 nL to the sample load. Sample is injected without dead volume onto the packed bed in the separation channel. This separation channel between ports 3 and 8 has a 75 µm x 50 µm trapezoidal cross-section and typically a length of 75 mm. A micromachined outlet frit was used to retain the packing at the end of the separation channel. On-chip UV-detection occurred behind the outlet frit with a prototype UV-cell of 50 µm i.d. and 300 µm path length (port 9) which was connected to the DAD with a special holder (Figure 4). The dead volume between outlet frit and detection cell (ports 8 and 9) was 2.5 nL. Thus, the overall dead volume passed by the analytes from injection to detection is negligible compared to the volume of the empty separation channel of about 260 nL. Behind the detector the mobile phase is redirected via ports 10 and 7 to an external flow sensor.

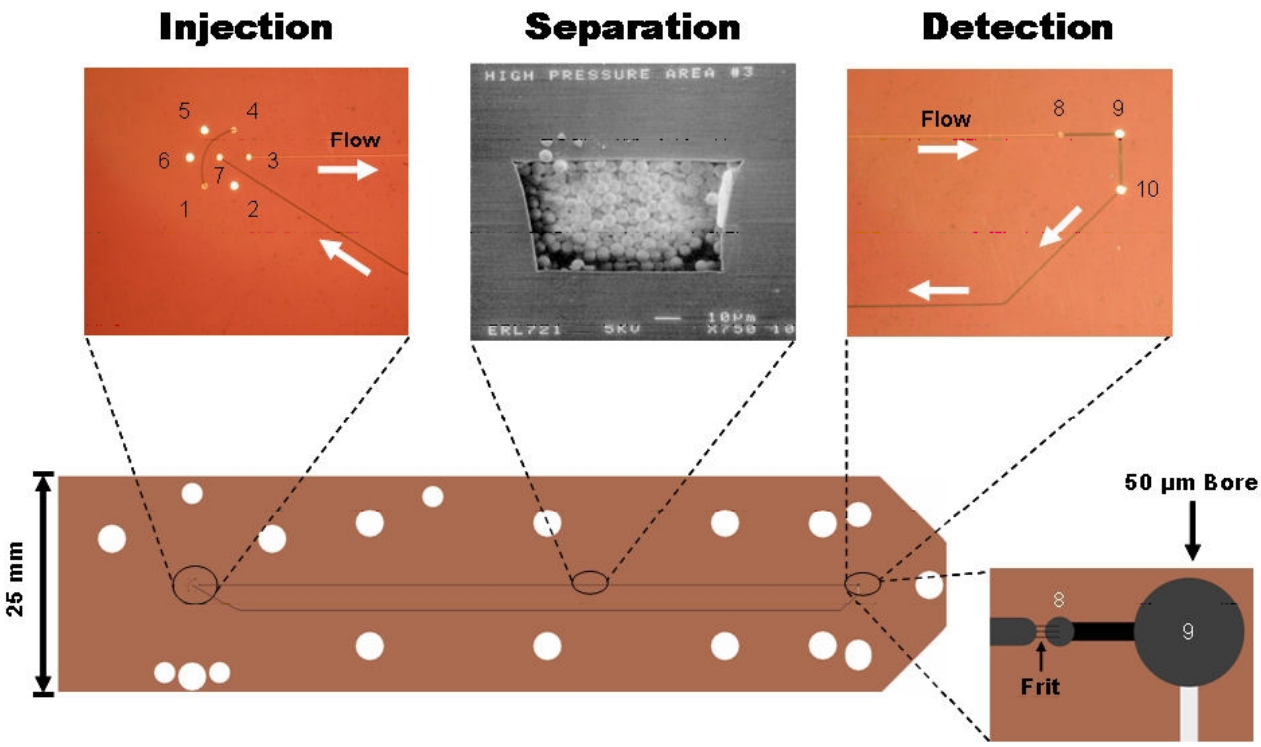

Figure 1: Layout of the polyimide-based microchips employed for the study of packing density and separation efficiency in microchip-HPLC. The design integrates sample injection, HPLC separation in a packed bed with trapezoidal cross-section, and UV-detection.

2.3 Determination of empty channel dispersion

The microchips received were inspected optically for obvious damages, alignment problems and clogged channels via a microscope. Chips passing this test were assembled in the HPLC-device and equilibrated with acetonitrile/water 80/20 (v/v). Subsequently, pentylbenzene was injected at different volumetric flow rates for the determination of the chip volume and the empty channel efficiency. Pentylbenzene was used for a better comparison of the dispersion data, as this analyte was also considered to determine the efficiency in the packed microchannels. The other alkylbenzenes used in this study showed the same elution times (empty channel) due to the fact that there were no interactions (retention or adsorption) with the channel. Only the dispersion was slightly different due to the different diffusion coefficients of the analytes. The volume of the empty separation channel was usually about 260 nl and the empty channel efficiency as depicted in Figure 2 for 10 representative chips. The linear relationship of the plate height against the linear flow velocity is in agreement with the Taylor-Aris dispersion theory in empty channels if no retention mechanism is present. Particular variations of the plate height (chip-to-chip) were attributed to (non-visible) alignment problems arising during the arrangement and lamination of the microchip foils, non-permeable frits or clogged channels, causing additional band broadening. Hereby, these

chips showed a much steeper ascend compared to the curves plotted in Figure 2. This phenomenon was also present after the chips were packed and evaluated via H-u-plots. As expected the additional band broadening effects causing additional dispersion in the empty channel were also present with the packed channels and increased the C-Term of the plate height curves significantly. It was decided that all chips showing a considerable deviation in empty channel efficiency should not be considered for any further measurement.

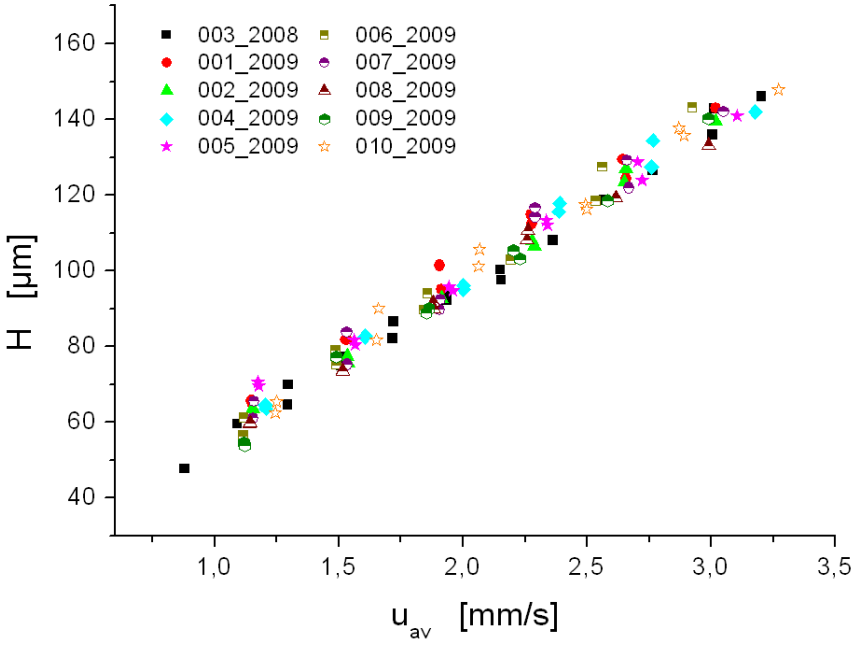

Figure 2: Evaluation of the empty channel efficiency for 10 representative chips.

2.4 Microchip packing

Slurries of 50 mg of the dry particles were prepared in ca. 1 mL tetrahydrofurane. Initially, the channels were slurry-packed by connecting the microchips to the autosampler of an Agilent 1200 liquid chromatograph. Microchips were fixed in a stainless-steel housing with a bore to port 3 (Figure 1) used to connect the needle of the autosampler to the separation channel. Methanol was used as pushing solvent for the packing process [26]. The applied pressure was kept constant for 7 min, followed by slow depressurization of the system for 10-20 min depending on packing pressure. This approach allowed to pack the separation channels at pressures of up to 400 bar, without ultrasound application.

For simultaneous application of high pressure and ultrasound during the packing process a WellChrom K-1900 pneumatic pump (Knauer GmbH, Berlin, Germany) with a 500 µm i.d. glass-lined metal tubing as slurry reservoir was used. Microchips were tightly fixed in a custom-built stainless-steel holder and connected to the packing station (Figure 3). After filling the slurry reservoir the microchips were inserted into an ultrasonic bath. By applying

simultaneously ultrasound and pressure of up to 400 bar the packing procedure was started and maintained for 7 minutes. Then, ultrasound was switched off and the system slowly depressurized which took at least 15 min. The microchips were disconnected, inspected microscopically for gaps in the packing and damages in general, and then attached to the injection valve and special UV-holder (see final assembly in Figure 4) for the subsequent studies of interparticle porosity and separation efficiency.

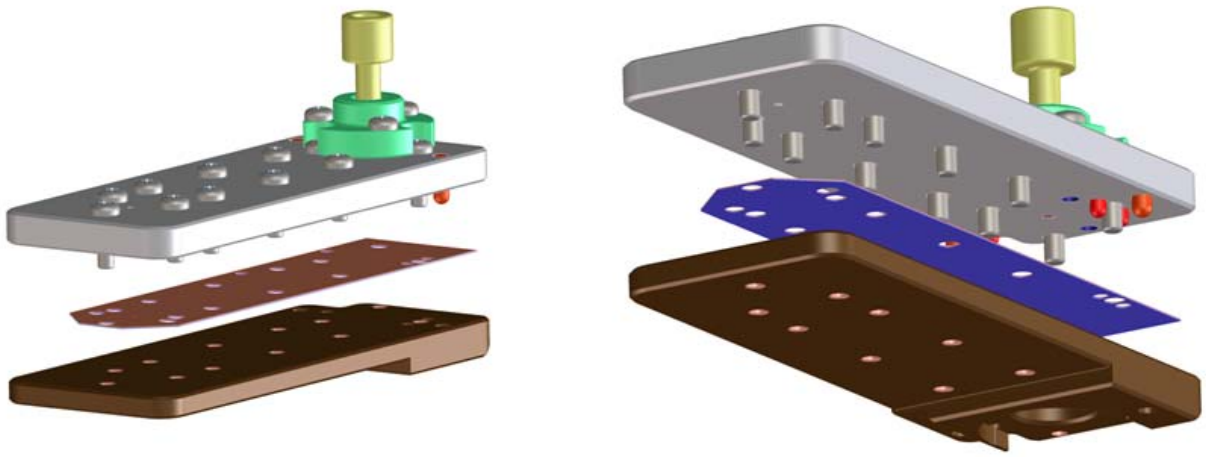

Figure 3: Custom-built stainless steel housing for the microchip packing process with high pressure and the assistance of ultrasound.

2.5 Packing densities and separation efficiencies

Packing densities in the separation channels of the microchips were analyzed with the help of inverse size-exclusion chromatography [25]. The interparticle pore volume (V_{inter}) of the packed microchips was calculated using the elution volumes in methylene chloride of a small polystyrene standard (M_r = 20000) that is just size-excluded from the intraparticle pore space of the employed C18-silica particles. The interparticle porosity (ε_{inter}) was then calculated by $\varepsilon_{inter} = V_{inter}/V_{ch}$ where V_{ch} is the volume of the empty separation channel measured prior to the microchip packing. Separation efficiencies were analyzed by isocratic elution of a mixture of alkylbenzenes with acetonitrile/water 80/20 (v/v) and uracil as dead time marker. This complementary analysis allowed to correlate the packing procedure for the microchips with the achieved packing densities and separation efficiencies.

2.6 Hardware configuration

All data were acquired with an Agilent 1200 liquid chromatograph, including a degasser and a nanopump, equipped with a diode-array UV detector. Microchips were sandwiched between the stator and the rotor of a two-position HPLC rotary valve (Figure 4). Volumetric flow rates were controlled by an additional flow sensor (Model SLG-1430-150 from Sensirion, Staefa, Switzerland) installed behind the analytical system (behind port 7, see Figure 1). Packing densities (interparticle porosities) were analyzed with methylene chloride as mobile phase and detection at 230 nm, while separation efficiencies were analyzed with acetonitrile/water 80/20 (v/v) as mobile phase and detection at 210 nm. All experiments were carried out at 298 ± 1 K.

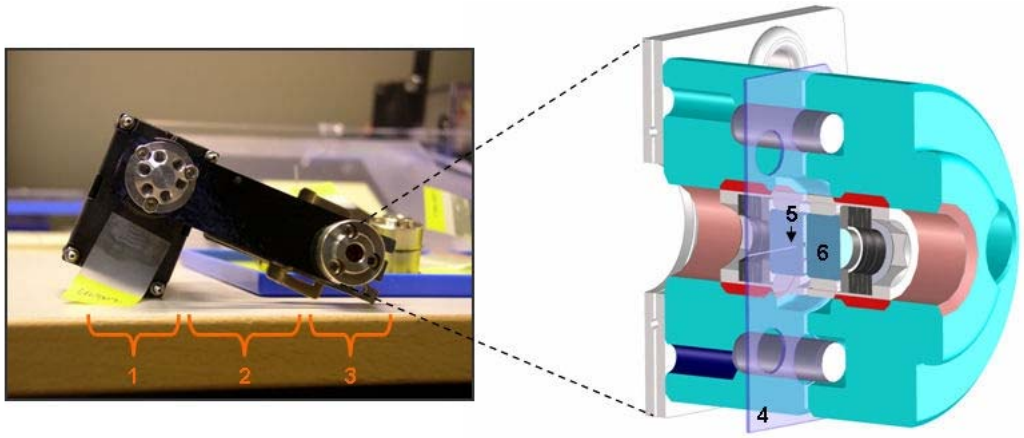

Figure 4: Final assembly of an HPLC microchip between rotary valve and UV detection cell. The numbers indicate 1: injection; 2: separation; 3: detection; 4: fixed microchip; 5: particle-packed separation channel; and 6: sapphire window (3 mm thick).

3 Results and Discussion

Microchips of the design illustrated in Figures 1 and 4 and packed under different conditions were studied by chromatographic separations of a mixture of alkylbenzenes (Figure 5a) at different mobile phase velocities. The peak shapes observed in the chromatograms were generally very symmetrical, with typical asymmetry factors around 1.1. Separation efficiencies of the microchips were analyzed by the axial plate height calculated from the pentylbenzene peak (k' = 3.5) in the chromatograms. Figure 5b shows the dependence of axial plate height (H) on the average mobile phase velocity (u_{av}) for microchips under different packing conditions. It is evident that both, packing pressure (150 bar → 300 bar) and the application of ultrasound, are critical to obtaining good separation

efficiencies. The chromatogram shown in Figure 5a was acquired at the highest applied mobile phase velocity (u_{av} = 4.6 mm/s) with the best-performing microchip packed at 300 bar and with ultrasound assistance, resulting in an axial plate height of H = 25 µm for pentylbenzene (cf. Figure 5b).

The improvement in separation efficiency demonstrated in Figure 5b of microchips packed at higher pressure (150 bar → 300 bar) and with ultrasound assistance is significant, by a factor of more than three for velocities above u_{av} = 4 mm/s. Packing pressures of up to 400 bar were investigated, with and without ultrasound assistance, but did not result in a further improvement of separation efficiencies. While Figure 5b reveals also a decrease in the minimum plate height from 23 µm at u_{av} = 0.55 mm/s for the microchip packed at 150 bar to 14 µm at u_{av} = 1.25 mm/s for the one packed at 300 bar and with ultrasound assistance, the strongest effect is seen at increasing velocities (for u_{av} > 1 mm/s) in a strongly reduced slope of the plate height curve. With the best-performing microchip (300 bar/ultrasound) we observe a relatively broad minimum and weak increase in plate heights for u_{av} > 1.5 mm/s. This behavior indicates that the contribution to the plate height from mass transfer resistance in the mobile phase (which scales linearly with the average velocity) is very sensitive to the packing procedure used for the microchips.

A possible reason for this behavior can be found in the channeling of fluid flow in the corners of noncylindrical, here trapezoidal packings which is expected to depend critically on the packing density. It has been demonstrated that the morphologies and corresponding flow patterns for noncylindrical packings can deviate significantly from those of conventional cylindrical packings [24]. This deviation becomes more pronounced at higher bed porosities (lower packing densities). Extended regions of high local porosity in the corners of noncylindrical conduits give rise to the formation of fluid channels of advanced flow velocity, while at lower bed porosities (higher packing densities) hydrodynamic dispersion comes close to that of the cylindrical packings [24].

In order to verify this hypothesis we analyzed the packing densities of the microchips by their interparticle porosity (ε_{inter}), using a suitable polystyrene standard in methylene chloride which is size-excluded from the intraparticle pore space of the packing [25]. We found a consistent decrease in ε_{inter} of the microchips with increasing separation efficiency, that is, ε_{inter} decreased in the following series of packing modes: 150 bar > 150 bar/ultrasound > 300 bar > 300 bar/ultrasound. The more densely a microchip is packed, the better it performs. In Figure 6a plate height data at selected mobile phase velocities from Figure 5b are correlated to the actual values of ε_{inter}. For example, at a velocity of u_{av} = 3.7 mm/s (open circles) we observe a decrease in plate height by a factor of about three from the microchip packed at 150 bar (ε_{inter} = 0.475) to the one packed at 300 bar and with ultrasound assistance (ε_{inter} =

0.423). These complementary data confirm that the improvement in separation efficiency (Figure 5b) can be explained by higher packing densities (Figure 6a) achieved by the increased packing pressure and application of ultrasound.

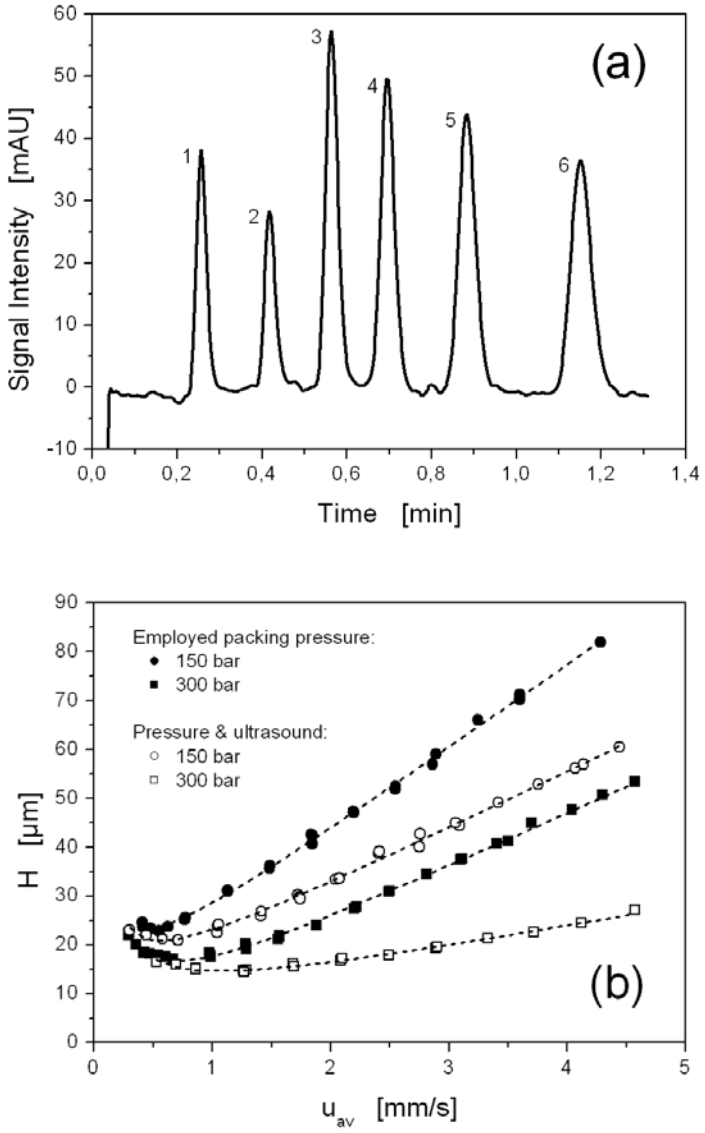

Figure 5: (a) Separation of alkylbenzenes (u_{av} = 4.6 mm/s) using the microchip packed at 300 bar and with the assistance of ultrasound (see Figure 5b: bottom curve, last point for pentylbenzene). Analytes (asymmetry factors) are 1: uracil (0.97); 2: benzene (1.20); 3: ethylbenzene (1.06); 4: propylbenzene (1.25); 5: butylbenzene (1.04); and 6: pentylbenzene (1.14). (b) Plate height *vs.* average mobile phase velocity for microchips packed at different pressures, with or without the assistance of ultrasound. Mobile phase: acetonitrile/water 80/20 (v/v); analyte: pentylbenzene (k' = 3.5).

As mentioned above, the corners of a noncylindrical cross-section favor the formation of channels of advanced fluid flow velocity. A denser packing reduces the extension of these channels as well as the actual fluid velocity in these channels [24]. Thus, associated hydrodynamic dispersion can be reduced significantly by a denser packing. The numerical analysis of a conduit with semicircular cross-section, which has a symmetry comparable to the trapezoidal one encountered in this work, revealed a reduction of the axial dispersion coefficient by a factor of about three at a reduced velocity of $u_{av}d_p/D_m = 20$ (where d_p is the particle diameter and D_m the tracer diffusivity in the mobile phase) when the interparticle porosity was decreased from $\varepsilon_{inter} = 0.48$ to $\varepsilon_{inter} = 0.42$ [24]. At least from a macroscopic hydrodynamic viewpoint these predictions, which are based on the numerical simulation of flow and dispersion in noncylindrical sphere packings, reflect closely the experimental data presented in this work for a similar velocity. The reduced velocity of $u_{av}d_p/D_m = 20$ in the simulations translates to an u_{av} of ca. 4 mm/s in this work. Around this velocity the data in Figures 3b and 4a show a reduction of the plate height (dispersion coefficient) by a factor of about three as the interparticle porosity is decreased from $\varepsilon_{inter} = 0.475$ (microchip packing at 150 bar) to $\varepsilon_{inter} = 0.423$ (300 bar and ultrasound), comparable to the simulated data.

In addition, a porosity-dependent intensity of the channeling in the corners of the trapezoidal packed beds well explains the different slopes of the plate height curves in Figure 5b (150 bar *vs.* 300 bar and ultrasound). The corner regions act as more permeable flow paths parallel to the more densely packed bed (parallel combination of unequal resistances) over the entire length of the bed. Lateral equilibration is diffusion-limited and therefore this macroscopic flow heterogeneity engenders mass transfer resistance in the mobile phase over relatively long distances (requiring trans-column equilibration) [24, 27].

The higher packing density in microchips not only effects better separation efficiencies, but also leads to an expected increase in pressure drop at a given flow rate, as illustrated in Figure 6b. While we observe a linear pressure drop – flow rate characteristics for both, densely and more loosely packed microchips ($\varepsilon_{inter} = 0.423$ and $\varepsilon_{inter} = 0.475$), reflecting the validity of Darcy's law, the actual increase in pressure drop for the denser packed microchip can be well explained on the basis of the Kozeny-Carman equation [28] which correlates pressure drop to the porosity function $(1 - \varepsilon_{inter})^2/\varepsilon_{inter}^3$.

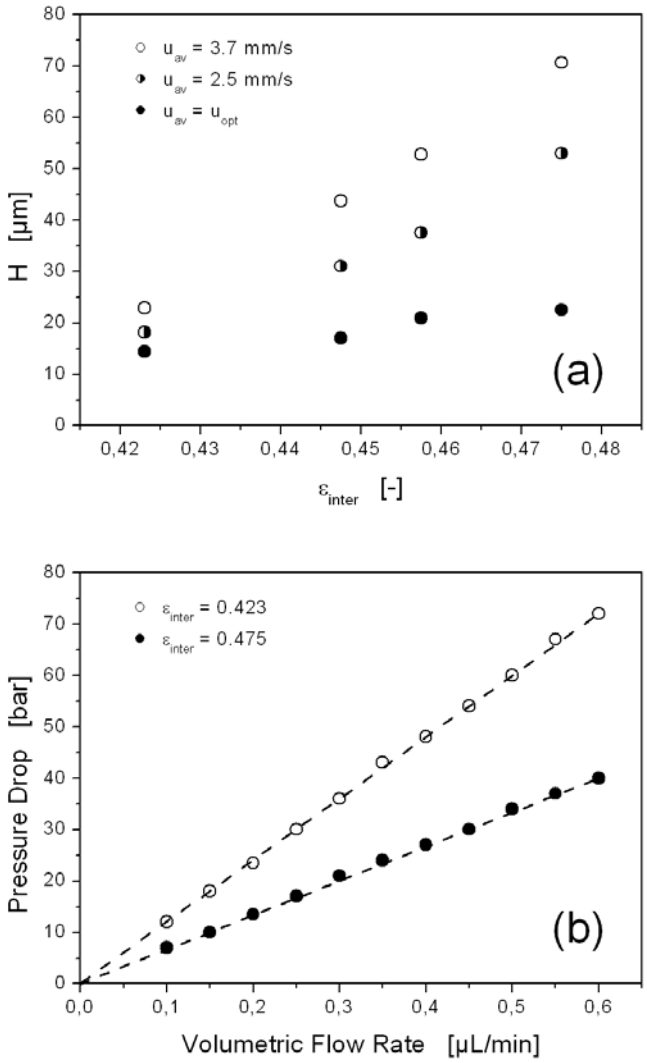

Figure 6: (a) Dependence of plate height at selected mobile phase velocities on the interparticle porosity of packed microchips. u_{opt} refers to the minimum in the plate height curves of Figure 5b. Mobile phase: acetonitrile/water 80/20 (v/v); analyte: pentylbenzene (k' = 3.5). (b) Pressure drop over the length of the packed separation channel (75 mm) *vs.* volumetric flow rate. The lower packing density (ε_{inter} = 0.475) characterizes the microchip packed at 150 bar; ε_{inter} = 0.423 corresponds to the one packed at 300 bar and with ultrasound assistance (cf. Figure 5b).

The interparticle porosity of microchips packed at 300 bar and with ultrasound assistance ($\varepsilon_{inter} \approx 0.42$) characterizes packing densities very close to those realized in nano-HPLC columns packed with the same particles [25]. In particular, we found ε_{inter} = 0.41-0.43 for 50 and 75 µm i.d. cylindrical fused-silica capillary columns packed with the Zorbax particles used in this study. These capillaries were packed following optimized protocols available in the literature. This means that with the current equipment the microchips can be packed as densely as conventional columns in nano-HPLC with a comparable column-to-particle size ratio. This is an important finding because microchip column packing is not a firmly established procedure, but still retains an experimental character: Microchannels are often filled manually with a syringe or the help of pumps at low to moderate pressure. We

show that, in principle, noncylindrical packings in microchip-HPLC can be prepared as densely as those routinely used in nano-HPLC.

An important conclusion from this fact is that the separation efficiencies of the noncylindrical packed beds in microchip-HPLC should become similar to those achieved with the cylindrical packings in nano-HPLC [24]. Figure 7 compares plate height data generated with the packed microchips to those realized with 50 and 75 µm i.d. cylindrical fused-silica capillaries packed with the same particles [25]. The complete range spanned by the plate height data for these nano-HPLC columns is represented by the gray-shaded area. The microchips used in this comparison (circles) have been packed at 300 bar and with ultrasound assistance reflecting the best packing conditions realized in this work (cf. Figure 5b). All packed bed structures gave interparticle porosities of ε_{inter} = 0.41-0.43 and are, thus, comparable in this regard. In addition, the packed microchips, which were taken from different fabrication batches, demonstrate a good reproducibility concerning separation efficiencies in combination with the packing process.

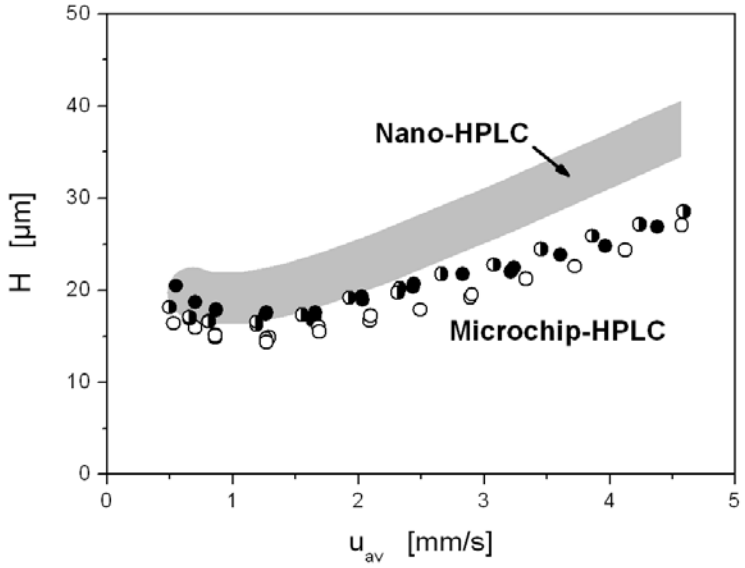

Figure 7: Comparison of plate height curves in nano-HPLC and microchip-HPLC employing 50 and 75 µm i.d. cylindrical fused-silica capillaries and polyimide-based microchips with a ca. 50 µm x 75 µm trapezoidal cross-section, respectively, packed with the same particles (5 µm-sized Zorbax SB-C18). The three microchip packings (circles) have been prepared with 300 bar as packing pressure and ultrasound assistance. Mobile phase: acetonitrile/water 80/20 (v/v); analyte: pentylbenzene (k' = 3.5).

While the plate height data in nano-HPLC and microchip-HPLC are generally close, especially around the plate height minimum (u_{av} = 1.0-1.5 mm/s), the microchips even demonstrate a slightly better performance at increasing mobile phase velocities (u_{av} > 2 mm/s). We attribute this finding to the preparation (sintering) of inlet and outlet frits in the

case of the packed capillaries. Packed capillaries were cut at the inlet frit and connected directly to the injection valve, and the detection window was prepared immediately behind the outlet frit [25]. Thus the dead volume for the nano-HPLC configuration was minimized, as in the microchip-HPLC studies. Sintered frits are known as a possible source of structural inhomogeneities which increase band broadening. The retaining filter and frit elements of microchips can be micromachined more precisely, homogeneously, and reproducibly than frits can be sintered over the whole cross-section of the capillaries, which may explain the slightly better performance of microchip-HPLC compared to nano-HPLC demonstrated by Figure 7.

4 Conclusions

This work provides an experimental analysis and consistent interrelation of the packing procedure, resulting packing density (interparticle porosity), pressure drop over the packed microchannel, and separation efficiency under isocratic elution conditions for noncylindrical packed beds employed in microchip-HPLC. In particular, the present work demonstrates that the separation channels of suitable microfluidic analysis systems, which often cannot tolerate the high packing pressures used in conventional column packing and the application of ultrasound, can be packed as densely as the cylindrical fused-silica capillaries commonly used in nano-HPLC. This progress was realized with a stainless steel envelope which tightly fixed the flexible polymeric microchips during the packing process, allowing the application of packing pressures of up to 400 bar with ultrasound assistance. The achieved packing densities were comparable to those in nano-HPLC for capillary columns characterized by similar column-to-particle size ratios as the trapezoidal microchip separation channels when packed with the same particles.

To realize the dense packing in microchip separation channels that is crucial to achieve good separation efficiency, it is necessary to optimize packing procedures, and in this respect the development of high-pressure rating microchannels and fittings is particularly desirable. As a consequence of the denser packing the separation efficiencies in microchip-HPLC with noncylindrical packed beds approach those realized with the cylindrical packed beds used in conventional nano-HPLC. This behavior was predicted by numerical simulations [24] and is explained by the presence of fluid channels of advanced flow velocity in the corners in noncylindrical packed beds. Noncylindrical packings are therefore much stronger affected by higher bed porosities than cylindrical ones, while at low bed porosities hydrodynamic dispersion comes close to that of the cylindrical packings as demonstrated experimentally in this work. With optimized particle packing in the separation channels the

microchip-HPLC platform benefits from a seamless integration of functional elements and the precision possible with micromachining technology.

References

[1] Smith, R. D.; Shen, Y. F.; Tang, K. Q. *Acc. Chem. Res.* **2004**, *37*, 269-278.

[2] Saito, Y.; Jinno, K.; Greibokk, T. *J. Sep. Sci.* **2004**, *27*, 1379-1390.

[3] Shen, Y. F.; Smith, R. D. *Expert Rev. Proteomics* **2005**, *2*, 431-447.

[4] Wickremsinhe, E. R.; Singh, G.; Ackermann, B. L.; Gillespie, T. A.; Chaudhary, A. K. *Curr. Drug Metabolism* **2006**, *7*, 913-928.

[5] Manisali, I.; Chen, D. D. Y.; Schneider, B. B. *Trends Anal. Chem.* **2006**, *25*, 243-256.

[6] Hernández-Borges, J.; Aturki, Z.; Rocco, A.; Fanali, S. *J. Sep. Sci.* **2007**, *30*, 1589-1610.

[7] Koster, S.; Verpoorte, E. *Lab Chip* **2007**, *7*, 1394-1412.

[8] Xie, J.; Miao, Y.; Shih, J.; Tai, Y.-C.; Lee, T. D. *Anal. Chem.* **2005**, *77*, 6947-6953.

[9] Lazar, I. M.; Trisiripisal, P.; Sarvaiya, H. A. *Anal. Chem.* **2006**, *78*, 5513-5524.

[10] Yin, H.; Killeen, K.; Brennen, R.; Sobek, D.; Werlich, M.; van de Goor, T. *Anal. Chem.* **2005**, *77*, 527-533.

[11] Reichmuth, D. S.; Shepodd, T. J.; Kirby, B. J. *Anal. Chem.* **2005**, *77*, 2997-3000.

[12] Carlier, J.; Arscott, S.; Thomy, V.; Camart, J. C.; Cren-Olivé, C.; Le Gac, S. *J. Chromatogr. A* **2005**, *1071*, 213-222.

[13] Yang, Y.; Li, C.; Kameoka, J.; Lee, K. H.; Craighead, H. G. *Lab Chip* **2005**, *5*, 869-876.

[14] Shih, C.-Y.; Chen, Y.; Xie, J.; He, Q.; Tai, Y.-C. *J. Chromatogr. A* **2006**, *127*, 272-278.

[15] Ro, K. W.; Liu, J.; Knapp, D. R. *J. Chromatogr. A* **2006**, *1111*, 40-47.

[16] Ishida, A.; Yoshikawa, T.; Natsume, M.; Kamidate, T. *J. Chromatogr. A* **2006**, *1132*, 90-98.

[17] Bhattacharyya, A.; Klapperich, C. M. *Anal. Chem.* **2006**, *78*, 788-792.

[18] Mair, D. A.; Geiger, E.; Pisano, A. P.; Fréchet, J. M. J.; Svec, F. *Lab Chip* **2006**, *6*, 1346-1354.

[19] Wen, J.; Guillo, C.; Ferrance, J. P.; Landers, J. P. *Anal. Chem.* **2007**, *79*, 6135- 6142.

[20] Brio Cartridges, Nanostream, Pasadena, CA, USA.

[21] De Malsche, W.; Eghbali, H.; Clicq, D.; Vangelooven, J.; Gardeniers, H.; Desmet, G. *Anal. Chem.* **2007**, *79*, 5915-5926.

[22] De Pra, M.; De Malsche, W.; Desmet, G.; Schoenmakers, P. J.; Kok, W. Th. *J. Sep. Sci.* **2007**, *30*, 1453-1460.

[23] Billen, J.; Desmet, G. *J. Chromatogr. A* **2007**, *1168*, 73-99.

[24] Khirevich, S.; Höltzel, A.; Hlushkou, D.; Tallarek, U. *Anal. Chem.* **2007**, *79*, 9340-9349.

[25] Ehlert, S.; Rösler, T.; Tallarek, U. *J. Sep. Sci.* **2008**, *31*, 1719-1728.

[26] Vissers, J. P. C.; Claessens, H. A.; Laven, J.; Cramers, C. A. *Anal. Chem.* **1995**, *67*, 2103-2109.

[27] Broeckhoven, K.; Desmet, G. *J. Chromatogr. A* **2007**, *1172*, 25-39.

[28] Bear, J. *Dynamics of Fluids in Porous Media*; Dover Publications: New York, **1988**.

Chapter 5 - Performance of HPLC/MS microchips in isocratic and gradient elution modes

1 Introduction

Miniaturized analysis systems are of growing interest in analytical chemistry [1-3]. They offer improved performance, smaller amount of sample consumption, rapid separation, and lower costs by integrating as many as possible miniaturized sample pre-treatment and analysis steps onto a single microchip. The ultimate goal are micro total analysis systems (μTAS) [4], which additionally offer automation and parallelization to meet the demands of high sample throughput and high sample complexity typical of screening applications and proteomics workflows [5, 6].

Experimental efforts of coupling microfluidic devices to mass spectrometers started a decade ago and are of on-going interest.[7-9] Microfluidic flow rates are well suited to the requirements of electrospray ionization mass spectrometry (ESI-MS). One of the challenges of chip-MS is the development of a stable and effective interface. The existing chip-ESI-MS interfaces use one of the following approaches: (1) spraying directly from the edge of a chip [10, 11], (2) spraying from a chip-inserted fused-silica capillary [12, 13], and (3) spraying from a chip-integrated (micro-fabricated) ESI-tip [14-16].

For interfacing on-chip separation techniques like capillary electrophoresis (CE) or liquid chromatography (LC) to MS, the critical point of all interfacing methods is the associated dead volume. Harrison's group has shown that even small dead volumes can significantly decrease the separation performance by post-column band broadening [12, 13]. Most of the chip-MS systems described in the literature contain ESI-tips made from fused-silica capillaries that were attached *after* microchip fabrication [8, 9]. There is, however, a growing number of MS-chips with integrated ESI-tips. This approach minimizes dead volumes and generally enables mass fabrication, as microfluidic channels and ESI-tip are formed during the same fabrication step.

Research on chip-LC has been slow to progress due to various obstacles, most of them related to pressure. For example, the integration of pressure-driven flow, especially high-pressure operation required for true HPLC, is still a challenge. Another problem is that dense particulate packings are much more difficult to attain in noncylindrical microchannels

than in the fused-silica capillaries conventionally used in nano-HPLC. While monolithic beds are easily fabricated in microchannels and have been used as separation media on LC-chips [10, 17-21], particulate beds have miscellaneous advantages due to the wide range of available surface chemistries and the knowledge gained from conventional HPLC [22]. High packing pressure and ultrasound are essential to obtain dense particulate beds in fused-silica capillaries as well as microchannels, but this requirement interferes with the pressure-sensitivity of most LC-chips, which tolerate only low to moderate pressures. Consequently, particulate beds on LC-chips [15, 23-26] have so far mostly been packed under sub-optimal conditions. As research on chip-LC is usually focused on integration, systematic evaluations of the performance of LC-chips, monolithic or particulate, have been rare [27, 28].

With the ability of the MS-detector to resolve several peaks simultaneously, the chromatographic performance of HPLC/MS chips has not been considered to be of prime importance. But the complexity of typical samples requires good chromatographic resolution with discrete peaks. Interferences like background noise and ion suppression increase with sample complexity [29], so improvement of peak shape and resolution is important to reduce the co-elution of analytes and provide a better MS performance, which ultimately enables the analysis of more analytes at smaller concentrations in a shorter time.

The detailed three-dimensional numerical simulation of flow and dispersion in particulate microchip packings has recently shown that high packing density is one of the most important factors for realizing excellent, true HPLC separation efficiencies with microchips [30-32]. In this experimental study the packing conditions and particle size of the packing material of the standard Agilent HPLC/MS chip (Figure 1) are systematically varied and the chip’s performance investigated in terms of hydraulic permeability and separation efficiency under isocratic and gradient elution conditions.

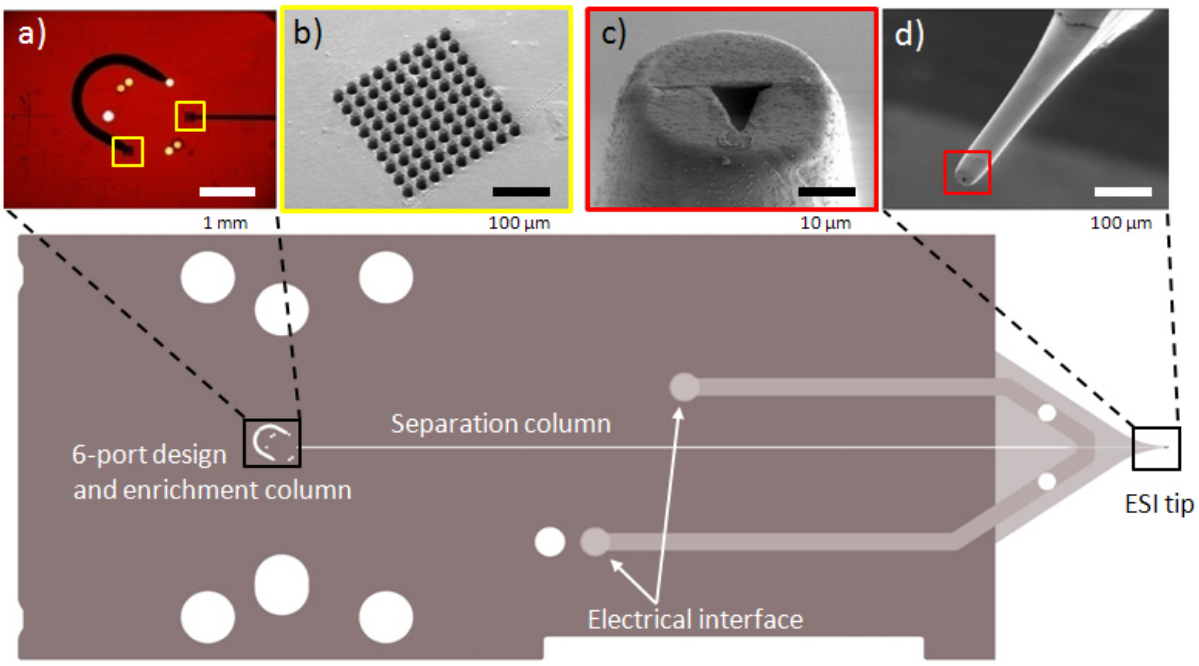

Figure 1: Layout of the polyimide HPLC/MS chip integrating sample enrichment, HPLC separation on a packed particulate bed, and electrospray ionisation. Enlargements show details of the chip: (a) six-port-interface and serpentine enrichment column, (b) µ-sieves for retaining the packing at the inlet of enrichment and separation columns, and (c, d) the ESI-tip with its Gaussian-shaped orifice. Two internally grounded electrodes provide the contact to the microfluidic channel near the ESI-tip (see electrical interface).

2 Experimental

2.1 Chemicals and materials

HPLC grade tetrahydrofuran was purchased from AppliChem GmbH (Darmstadt, Germany) and the alkylphenones pentanophenone, hexanophenone, and octanophenone from Pierce Chemicals (Rockford, IL). Methanol, uracil, heptanophenone, nadolol, atropine, timolol maleate, trimipramine maleate, metoprolol tartrate, and hydrochloride salts of acebutolol, labetalol, propranolol, alprenolol, betaxolol, and imipramine as well as peptides (methionine-enkephalin, angiotensin III, neurotensin, and substance P) were purchased from Sigma-Aldrich Chemie GmbH (Taufkirchen, Germany). Formic acid (FA) and trifluoroacetic acid (TFA) were obtained from Fluka Chemie GmbH (Buchs, Switzerland) and HPLC grade acetonitrile from Merck KGaA (Darmstadt, Germany). HPLC grade water was prepared with a Milli-Q gradient water purification system (Millipore, Bedford, MA). The packing materials were 3.5 µm and 5 µm (nominal particle sizes) Zorbax SB-C18, classical reversed-phase materials (C18-bonded silicas, non-endcapped), with a mean intraparticle pore size of 80 Å (Agilent Technologies, Waldbronn, Germany).

2.2 Particle size distributions

The two particle size distributions were characterized on a Mastersizer 2000 equipped with a Hydro SM manual small volume sample dispersion unit (Malvern Instruments GmbH, Herrenberg, Germany). A spatula tip of the particles was dispersed in 30 ml isopropanol and injected into the device. Three measurements were averaged for each nominal particle size and the results are summarized in Table 1 and Figure 2. Both distributions are close to log-normal and have similar asymmetries as reflected by their $d_{p,\#}^{90} / d_{p,\#}^{10}$ ratios.

Table 1: Characteristics of the particle size distributions.[a)]

Material	$d_{p,\#}$ [µm]	$d_{p,\#}^{10}$ [µm]	$d_{p,\#}^{90}$ [µm]	$d_{p,\#}^{90} / d_{p,\#}^{10}$	$d_{p,surf}$ [µm]	$d_{p,vol}$ [µm]
Zorbax SB C18 3.5 µm	3.40	2.61	4.68	1.79	3.82	4.10
Zorbax SB C18 5 µm	4.72	3.69	6.41	1.73	5.25	5.59

a) Mean particle diameters $d_{p,\#}$, $d_{p,surf}$, and $d_{p,vol}$ refer to the number-, surface area-, and volume-weighted size distributions. $d_{p,\#}^{10}$ and $d_{p,\#}^{90}$ are the 10 and 90 percentiles and $d_{p,\#}^{90} / d_{p,\#}^{10}$ is their ratio.

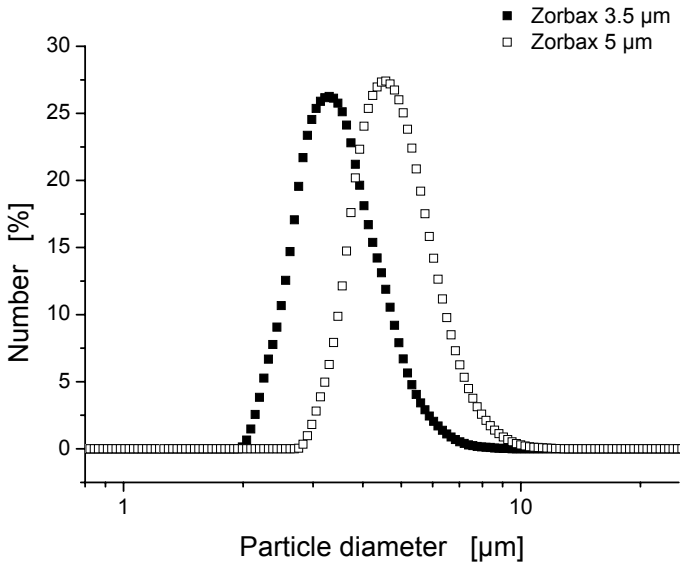

Figure 2: Size distribution of the 3.5 and 5 µm Zorbax SB-C18 particles.

2.3 Microchip packing

For the slurry-packing of the microchips' separation channels, suspensions of 50 and 75 mg of the dry 5 and 3.5 µm particles, respectively, in 1 ml tetrahydrofuran were prepared. The HPLC/MS chips were tightly fixed in a custom-built stainless-steel holder and connected to the packing apparatus. A WellChrom K-1900 pneumatic pump (Knauer GmbH, Berlin, Germany) equipped with a glass-lined metal tubing (500 µm i.d.) as slurry reservoir was used for the application of high pressures (up to 300 bar). After filling the slurry reservoir and inserting the microchip into an ultrasonic bath the packing procedure was started and took 13 minutes. Methanol served as the pushing solvent [33]. Subsequently, ultrasound was switched off and the system depressurized slowly for at least 20 minutes. Afterwards, chips were inspected microscopically for gaps in the packing and damages in general. Enrichment columns of all HPLC/MS chips (*cf.* Figure 1a) were slurry-packed (150 bar, no ultrasound) with the 5 µm Zorbax SB-C18 particles after packing the separation channels.

2.4. HPLC/MS analysis

We used an Agilent HPLC-Chip-Cube MS interface equipped with a 1100 LC/MSD trap XCT Ultra ion trap mass spectrometer. Data were acquired in the positive ion mode applying a voltage of 1.7 kV at the electrospray inlet capillary, a nitrogen drying gas flow of 3 l/min, and a temperature of 320°C at the transfer capillary for desolvation. The chromatograms shown in Figures 6 and 7 were derived from the extracted ion chromatograms of the individual analytes. An Agilent 1100 Cap pump at a flow rate of 4 µl/min attached to a 1100 microwell plate autosampler was used for sample injection. The packed HPLC/MS chips were connected to a six-port face-seal rotary valve.

In isocratic elution mode the enrichment column (Figure 1a) was by-passed with an on-chip loop (internal volume: 1.6 nl), similar to the injection method described before [27, 28]. In gradient elution mode the sample (injected volume: 1 µl) was loaded from the autosampler onto the enrichment column via the six-port rotary valve, while the separation column was equilibrated with the mobile phase (Figure 3a). A switch of the rotor controlled by the ChemStation software started elution of the sample from the enrichment onto the separation column with the mobile phase gradient (Figure 3b).

Pressure drop – flow rate curves of the packed microchips (for comparison of their hydraulic permeabilities) were acquired with a typical reversed-phase HPLC mobile phase of water/acetonitrile 20/80 (v/v). Plate height curves for the analysis of separation efficiency under isocratic elution conditions were acquired with a mobile phase consisting of 0.1% FA in water/acetonitrile 50/50 (v/v) at volumetric flow rates between 100 and 1000 nl/min and the alkylphenones as analytes. This mobile phase with a lower acetonitrile content allowed to

realize a sufficiently strong retention on the reversed-phase particles required for the study of true chromatographic efficiencies without interference from extra-column band broadening (see later, Figure 6). Uracil was used as dead time marker. Gradient elution separations of the peptide mixture were carried out with a mobile phase of 0.05% TFA in water/acetonitrile. Gradients from 2 to 40% acetonitrile in 4, 8, 15, 20, and 25 min were applied at a flow rate of 500 nl/min. Gradient elution separations of the eleven drugs were carried out with a mobile phase of 0.1% FA in water/acetonitrile. Gradients from 2 to 70% acetonitrile in the same time steps as above were applied at a flow rate of 500 nl/min.

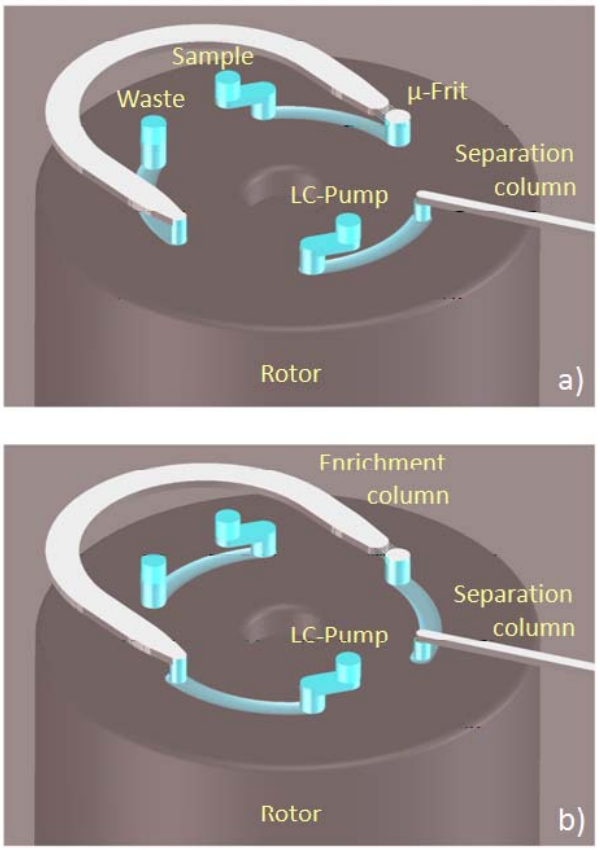

Figure 3: Schematic of the on-chip sample handling: (a) The sample is loaded onto the 40-nL enrichment column while the separation column is equilibrated with the mobile phase. (b) A left-turn motion of the rotor initiates elution of the trapped analytes from the enrichment column directly onto the separation column. Note that the LC pump is connected to the outlet of the enrichment column so that pre-separated analytes reach the separation column in reverse order of their migration distance in the enrichment column (backward-flush configuration).

2.5 HPLC/UV analysis

Experimental data of prototype HPLC/UV chips (hydraulic permeabilities; interparticle porosities reflecting their packing density; plate height curves) that are used for comparison with the performance of the HPLC/MS chips were collected under similar conditions. All details concerning these prototype HPLC/UV chips are described in our previous papers [27, 28]. The term prototype refers to the fact that these microchips were specially fabricated for our research with a UV-detection cell. Briefly, a prototype UV cell of 50 µm i.d. and 300 µm path length was installed behind the outlet frit of the separation channel and connected to the diode-array detector with a dedicated holder. Dead volume between outlet frit and detection cell (2.5 nl) is negligible compared to the volume of the separation channel of 260-290 nl. All data were acquired at 298 ± 1 K with an Agilent 1200 liquid chromatograph, including degasser, nanopump, and a diode array UV detector.

Interparticle porosities (ε_{inter}) representing the packing densities of the HPLC/UV chips were determined by inverse size-exclusion chromatography (ISEC) based on the elution of a polystyrene standard (extracted from an ISEC calibration curve obtained with a series of polystyrene standards) which is size-excluded from the intraparticle pores and therefore exclusively samples the void space between particles. This procedure is based on our earlier elaborated protocols [27, 28]. Interparticle porosities ($\varepsilon_{inter} = V_{inter}/V_{channel}$) are calculated from the interparticle elution volumes of this polystyrene standard (V_{inter}) and the geometrical volume of the separation channel ($V_{channel}$). The latter is measured with the elution volumes of the same polystyrene standard for the empty separation channels that were subsequently used for packing. Bed porosities of the HPLC/MS chips are not directly accessible by this way because polystyrene standards cannot be sprayed into the MS. However, they can be estimated via comparison of their hydraulic permeabilities with the HPLC/UV chips.

3 Results and Discussion

The design of the HPLC/MS chips is shown in Figure 1. These chips were fabricated by direct laser ablation and lamination of three polyimide foils of 125 µm (outer layers) and 50 µm (middle layer) thickness. The HPLC/MS chips contain a 40 nl enrichment column, a 43 mm long separation column with a *ca.* 50 µm (height) × 75 µm (median) trapezoidal cross-section (Figure 4a), microfluidic channels, solvent inlets, and a microfabricated ESI-emitter tip adjacent to the separation column (Figures 1c and 1d). Packed particles inside enrichment and separation columns are retained by µ-sieves at the inlet (Figure 1b) and µ-frits at the outlet (Figure 4b).

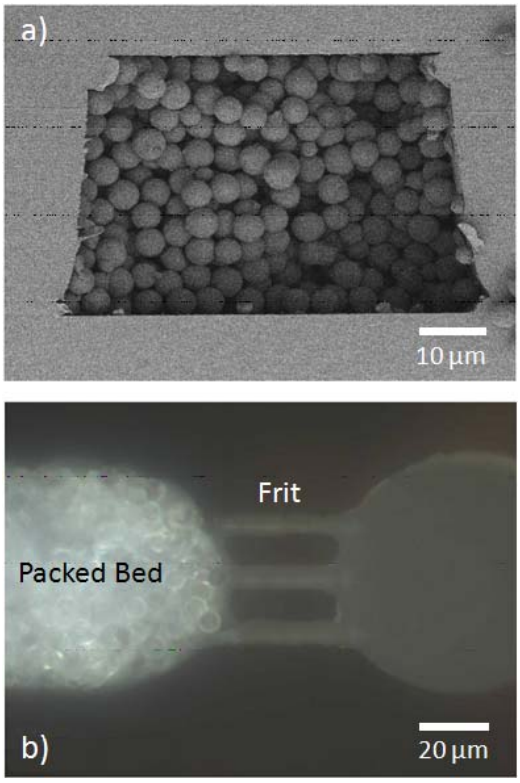

Figure 4: (a) SEM image of the ca. 50 µm (height) × 75 µm (median) trapezoidal cross-section of the separation column. The packed bed contains 5 µm Zorbax SB-C18 particles at an interparticle porosity of ε_{inter} ~ 0.42. (b) Microfabricated channels act as µ-frit to retain the packing at the outlet of the separation column.

HPLC/MS chips were packed under different conditions and with particles of different nominal size and compared with prototype HPLC/UV chips of a very similar design [27, 28]. As for the HPLC/MS chips the separation channels on the HPLC/UV chips have a *ca.* 50 µm × 75 µm trapezoidal cross-section, but a total length of 75 mm. This extension of the separation channels compared with the HPLC/MS chips (43 mm) is due to the spatial

configuration of the UV detection cell and its adapter [28]. The acquisition of the complementary data with these HPLC/UV chips not only allowed a more precise analysis of packing conditions and achieved packing densities for the HPLC/MS chips, therefore a better correlation of their analytical performance with their chromatographic efficiency, but also the comparison of both detection modes due to the similar chip and packing formats.

3.1 Hydraulic permeability

Darcy's law generally describes the resistance to flow of a Newtonian fluid with viscosity η through a packed bed as a linear relationship between the superficial velocity $u_{sf} = F_v/A$ (where F_v is the volumetric flow rate and A the cross-sectional area of the conduit) and the pressure drop over the length of the packed bed $\Delta p/L_{bed}$ [34]

$$u_{sf} = \frac{F_v}{A} = \frac{\kappa_D \Delta p}{\eta L_{bed}} \quad (1)$$

This linear relationship is valid for the case of creeping flow (linear-laminar flow regime) and incompressible Newtonian fluid and porous medium. Deviations from this law for packed beds starting at Reynolds numbers above 1 are attributed to inertial forces (nonlinear-laminar or viscous-inertial flow regime) and should not be misinterpreted as transition to turbulent flow [35]. The specific permeability κ_D is defined as a proportionality constant in Eq. (1); it can be accurately observed experimentally, but it does not provide insight into the physics of flow through a material.

We determined the pressure drop – flow rate curves for the packed microchip separation channels for each packing condition and nominal particle size (Figure 5). For both, the HPLC/MS and the HPLC/UV chips, these data were acquired at 298 ± 1 K (outside the MS-chip-cube compartment) over a sufficient range of volumetric flow rates and corrected for the pressure drop over the empty (unpacked) microchip assemblies. The ratio of pressure drop (Δp) and packed bed length (L_{bed}) was then plotted *vs.* the superficial velocity (u_{sf}), and the slope of the resulting graph determined by linear regression. To calculate κ_D from Eq. (1) the reciprocal of this slope was multiplied by the viscosity of the mobile phase ($\eta = 5.39 \times 10^{-4}$ Pa·s for water/acetonitrile 20/80 (v/v) at 298 K) [36].

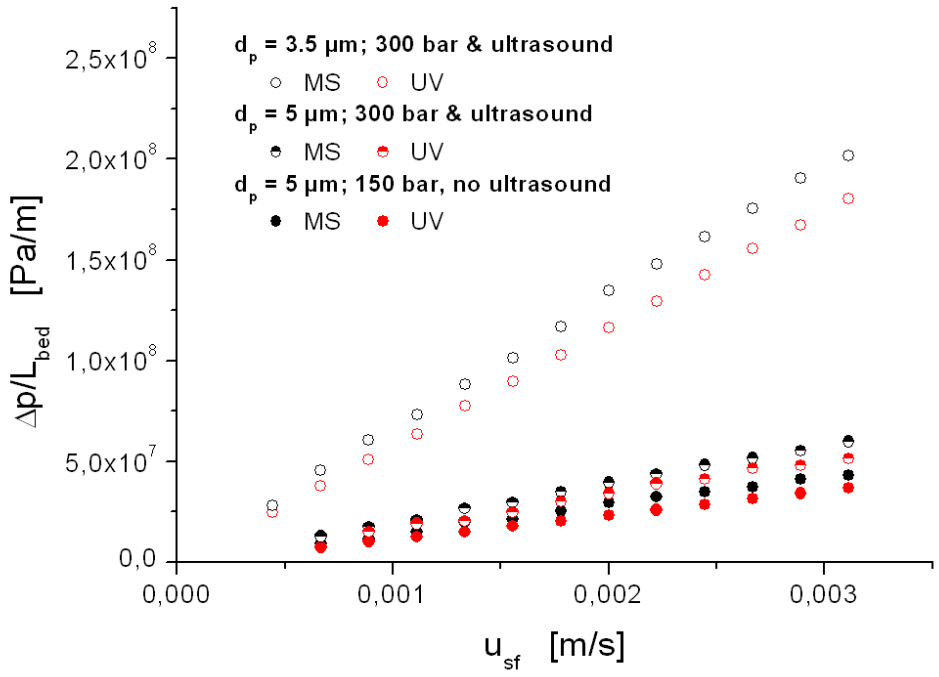

Figure 5: Pressure drop – flow rate data for prototype HPLC/UV chips and standard HPLC/MS chips packed with 3.5 or 5 µm Zorbax SB-C18 particles under the indicated conditions. Data are plotted as pressure drop measured over the length of the packed separation channel *vs.* the superficial velocity u_{sf} of the mobile phase, water/acetonitrile 20/80 (v/v).

The determined κ_D values (Table 2) of the chips decrease, *i.e.*, the resistance to flow of the packings increases, as expected, with increased packing pressure and decreased particle size of the packing material. Values for HPLC/MS chips packed with 3.5 and 5 µm particles at 300 bar and ultrasonication show good agreement with the data for the HPLC/UV chips (κ_D values of the HPLC/UV chips are 11.8% and 13.6% higher, respectively, than those of the corresponding HPLC/MS chips). The deviation of the κ_D values for microchips packed at 150 bar without ultrasonication is higher (19.1%).

Generally, hydraulic permeabilities of the HPLC/MS chips are lower than those of the HPLC/UV chips. This is a consequence of the shorter separation channel of the HPLC/MS chips (43 mm) compared with the HPLC/UV chips (73 mm) [27, 28]. A shorter channel translates to a higher pressure drop during packing under otherwise similar conditions. At 150 bar packing pressure, the shorter channel results in a denser bed, *i.e.*, in a decreased permeability of the HPLC/MS chips compared with the corresponding HPLC/UV chips (Table 2). With increased pressure and ultrasound application during packing the effect of the shorter channel is diminished, but still present.

Table 2: Specific Darcy permeabilities κ_D of the microchip packings.[a)]

Particle size and packing conditions	HPLC/UV κ_D [m^2]	HPLC/MS κ_D [m^2]
5 µm 150 bar, no ultrasound	4.49×10^{-14} $\varepsilon_{inter} = 0.48$	3.77×10^{-14} $\varepsilon_{inter} \approx 0.46$
5 µm 300 bar & ultrasound	3.17×10^{-14} $\varepsilon_{inter} = 0.42$	2.79×10^{-14} $\varepsilon_{inter} \approx 0.41$
3.5 µm 300 bar & ultrasound	0.920×10^{-14} $\varepsilon_{inter} = 0.40$	0.823×10^{-14} $\varepsilon_{inter} \approx 0.39$

a) **Interparticle porosities ε_{inter} of the HPLC/UV chips were determined by ISEC using the elution volumes of a suitable polystyrene standard (here, M_W = 20000 g/mol) in methylene chloride with UV detection at 230 nm [27].**

We therefore assume on the basis of the identical packing conditions and materials, the similar pressure drop – flow rate curves (Figure 5) and Darcy permeabilities (Table 2), that the bed porosities of the HPLC/MS chips and prototype HPLC/UV chips are close, but that in general the HPLC/MS chips are more densely packed. To further quantify this conclusion interparticle porosities (ε_{inter}) of the HPLC/UV chips have been determined by ISEC and are also listed in Table 2. Based on these values and permeability data in Figure 5 (κ_D in Table 2), the corresponding ε_{inter} for the HPLC/MS chips can be derived using the most popular porosity function $(1 - \varepsilon_{inter})^2/\varepsilon_{inter}^3$ after Blake, Kozeny, and Carman [34] to characterize the resistance to low Reynolds number flow of liquid through the microchip packings. Values of ε_{inter} for the HPLC/MS chips are expectedly slightly lower than for the HPLC/UV chips (Table 2) which is most pronounced for chips packed at 150 bar without ultrasound. For chips packed with the 3.5 µm particles at 300 bar and ultrasonication we obtain dense packings (HPLC/UV: $\varepsilon_{inter} = 0.40$, HPLC/MS: $\varepsilon_{inter} \approx 0.39$) [27, 28].

3.2 Separation efficiency in isocratic elution mode

We compared the chromatographic performance of the standard HPLC/MS chips with those of the prototype HPLC/UV chips by isocratic separation of four alkylphenones (pentano-, hexano-, heptano-, and octanophenone) using a mobile phase of 0.1% FA in acetonitrile/water 50/50 (v/v). Separation efficiencies were analyzed by the plate height H calculated from the full width at half maximum (FWHM) of the octanophenone peak. The retention factor $k' = (t_r - t_0)/t_0$ (where t_r is the retention time of the analyte and t_0 the residence time of an unretained tracer) for octanophenone was k' = 28 on the HPLC/MS chips and k' = 35 on the HPLC/UV chips. The decreased retention on the HPLC/MS chips with the same stationary and mobile phases is a consequence of the elevated temperature inside the MS-chip-cube compartment (313 ± 1 K) [37]. Separations with the prototype HPLC/UV chips were carried out at 298 ± 1 K like the permeability studies for both types of chips. The plate height curves (H *vs.* average mobile phase velocity u_{av}) are shown in Figure 6a. Both ultrasound and high pressure are crucial during packing to obtain improved separation efficiencies, where the minimum of the plate height curves (H_{min}) is shifted to lower plate heights (Table 3) and higher velocities. For chips packed with 3.5 µm particles at 300 bar and ultrasonication we obtain a good chromatographic performance as reflected by the reduced minimum plate heights (Table 3) of h_{min} = 2.5 (HPLC/UV) and h_{min} = 2.1 (HPLC/MS). Even more important, the slope of the plate height curves at higher velocities (Figure 6a) is smaller for the chips packed under optimal conditions, enabling shorter analysis times without compromising resolution (see typical range of velocities and volumetric flow rates for the HPLC/MS chips indicated by the dashed lines in Figure 6a).

Due to band broadening effects external to the microchip packings plate heights decrease with the retention factor (k') of the analyte for both chip types until an asymptotic value is reached (Figure 6b). It reflects the influence on the apparent separation efficiency of even a small extra-column volume of the instrument [38]. Yet the HPLC/MS chips show a much stronger dependence at small k'-values than their HPLC/UV counterparts, even if the actual plate height plateau is lower. Both chip types have a high, comparable ratio of the separation channels' volume (which contains the packing) to the chips' dead volume (HPLC/UV chip: ~110, HPLC/MS chip: ~150). We therefore assume that the diminished efficiency of the HPLC/MS chips at low k'-values is caused by additional band broadening effects that occur *after* separation, *i.e.*, during spray formation, ionization, and transfer to the mass spectrometer. In the plateau region, post-column band broadening effects lose their relative importance as a contribution to the overall peak width. The plate height data in Figure 6a have been recorded in this regime (*cf.* the k' of octanophenone in acetonitrile/water 50/50 (v/v)) to compare only the "true" packed microchannel efficiencies.

Table 3: Reduced minimum plate heights $h_{min} = H_{min}/d_{p,surf}$ of the packings.[a)]

Particle size and packing conditions	HPLC/UV h_{min}	HPLC/MS h_{min}
5 µm; 150 bar, no ultrasound	3.5	2.9
5 µm; 300 bar & ultrasound	2.6	2.1
3.5 µm; 300 bar & ultrasound	2.5	2.1

[a)] **Values of H_{min} were extracted from the plate height curves in Figure 6a and normalized by the respective $d_{p,surf}$ (Table 1).**

The question of why the HPLC/MS chips outperform the HPLC/UV chips in the plateau region (Figure 6b) and associated plate height curves (Figure 6a) cannot be answered with certainty. The plate height curves of Figure 6a generally reflect the respective Darcy permeabilities κ_D of the packings (Table 2), *i.e.*, lower Darcy permeabilities and interparticle porosities result in a more uniform flow profile over the cross-section of the microchip packings supposed for the shorter separation channels of the HPLC/MS chips. Our previous experiments [27] and simulations [30, 32] have shown that higher packing densities reduce the influence of the corners in noncylindrical conduits. The channel corners are locations of advanced fluid flow, and these high-porosity and high-velocity corner regions expand with increasing ε_{inter} of the packing (decreasing packing density). As the channel corners and adjacent loosely packed regions were the main source of flow heterogeneity in the simulated packings, band broadening in the more densely packed HPLC/MS microchip packings is lower than in the HPLC/UV chips mainly because of their more densely packed channel corners. The difference in the plate height curves of the chips packed at 150 bar is the most pronounced, whereas plate height curves of the 3.5 µm packings are similar (Figure 6a). For loosely packed beds such as those packed at 150 bar, even small differences in packing density affect the chromatographic performance notably [27], whereas this effect is lessened for the denser 3.5 µm packings.

Apart from the higher packing densities (Table 2) the elevated temperature of 313 ± 1 K inside the MS-chip-cube compartment could play a role. Higher temperatures reduce the mass transfer resistance of the analytes in the stationary phase which determines the slope of the plate height curves at higher velocities [37, 38]. The actual temperature difference of 15 K between HPLC/MS and HPLC/UV systems therefore also contributes to the improved plate height curves for the HPLC/MS chips (Figure 6a) and the correspondingly smaller plate heights in the plateau region (Figure 6b).

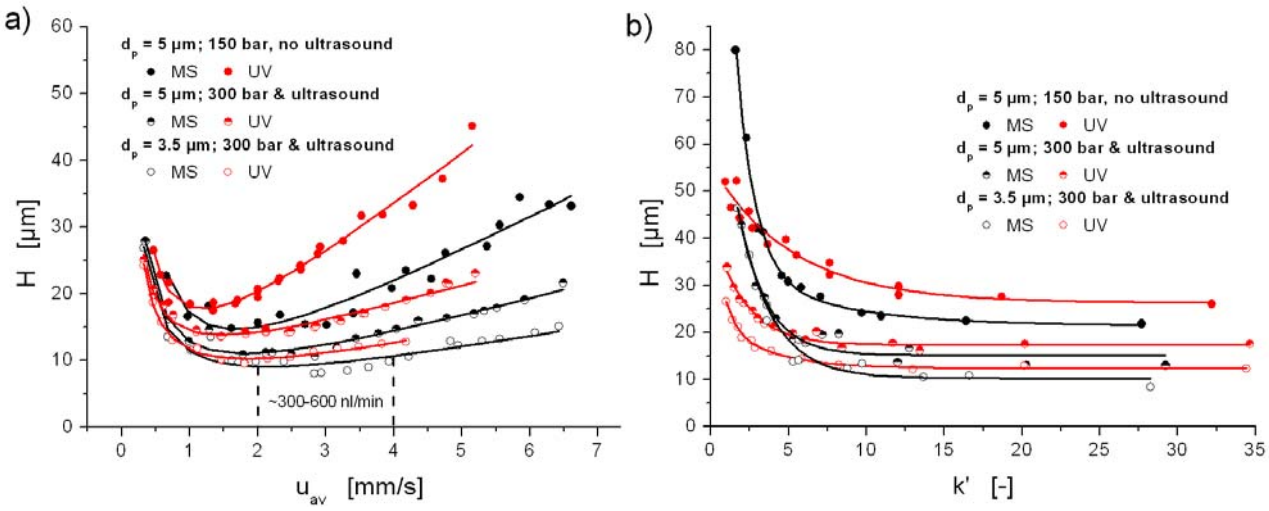

Figure 6: (a) Separation efficiency of prototype HPLC/UV chips and standard HPLC/MS chips packed under the indicated conditions. Plate heights H were calculated for the analyte octanophenone. Mobile phase: 0.1% FA in water/acetonitrile 50/50 (v/v). Each data point represents the average of three repeated experiments. (b) Plate height H *vs.* retention factor k' for prototype HPLC/UV chips and standard HPLC/MS chips at an average mobile phase velocity of u_{av} = 3.3 mm/s. To realize a sufficiently wide range of k' values for the alkylphenones the mobile phase composition has been varied from water/acetonitrile 20/80 via 30/70 and 40/60 to 50/50 (v/v).

3.3 Gradient elution performance

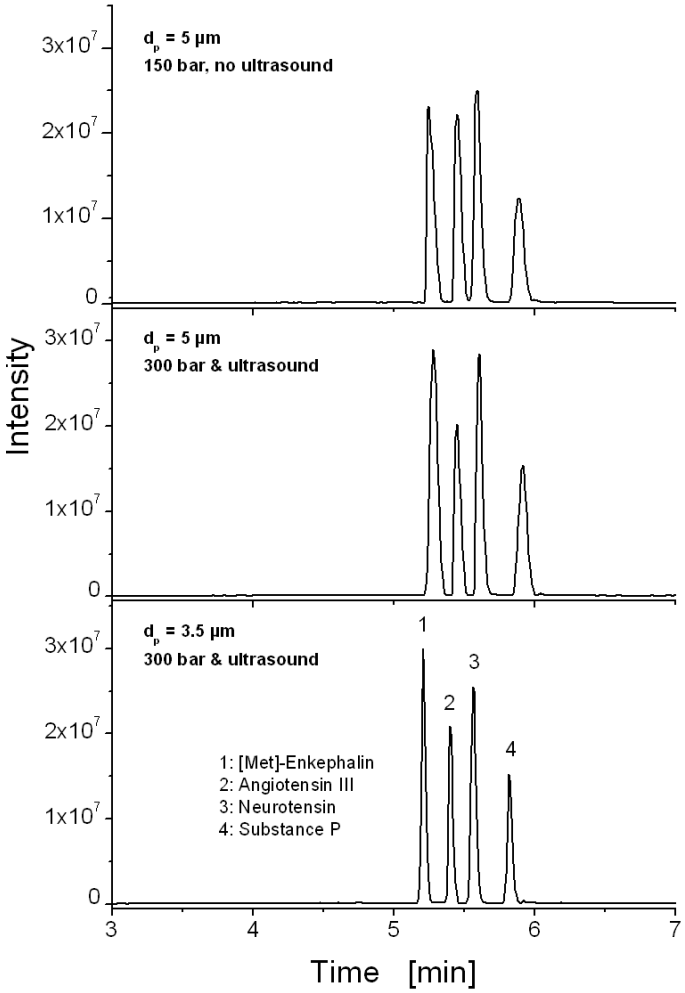

Figure 7: Separation of the four peptides on HPLC/MS chips packed under the indicated conditions. Mobile phase: 0.05% TFA in water/acetonitrile. Gradient: 2-40% acetonitrile in 4 min. Flow rate: 500 nl/min. Injected volume: 1 µl. Sample concentration: 100 fmol/µl of each peptide.

HPLC/MS-experiments for both, small molecule as well as biopolymer analysis, are usually done with gradient elution, and thus the performance of the HPLC/MS chips was investigated under typical experimental conditions, even though it has to be mentioned here that the separation efficiency can be judged adequately only under isocratic conditions.

Figures 7 and 8 contain the chromatograms from gradient elution separations carried out on the different HPLC/MS chips. They show the separation of the four peptides (Figure 7) and the separation of the eleven drugs (Figure 8). Peak width estimated by the full width at half maximum (FWHM) decreased and the resolution increased with applied packing pressure (and ultrasound) and reduced particle size of the microchip packings (from top to bottom in Figures 7 and 8). This is exemplary pointed out for peaks 6 to 9 in Figure 8 (zoomed area): propranolol (7) and alprenolol (8) co-elute in the top chromatogram, begin to

separate in the middle chromatogram, and are well separated in the bottom chromatogram. Performance gains at several gradient times are quantified in Table 4 for the drug separation. Even for steep gradients, the peak width decreased by ~15% and the resolution increased by ~20% after changing the packing conditions from 150 bar without ultrasound to 300 bar and ultrasound for the 5 µm particles. Reduction of particle size from 5 to 3.5 µm decreased the peak width further by ~15% and increased the resolution by ~20%. These findings correspond to the results from the isocratic elution experiments and demonstrate that the analytical performance of the HPLC/MS chip is critically affected by the quality of the chromatographic separation even under gradient elution conditions.

Table 4: Chromatographic performance – packing characteristics.[a)]

	5 µm: 150 bar, no ultrasound → 300 bar & ultrasound		300 bar & ultrasound: 5 µm → 3.5 µm	
Gradient time [min]	**FWHM** [%]	**Resolution** [%]	**FWHM** [%]	**Resolution** [%]
4	13.2	14.6	13.3	17.6
8	15.0	23.7	14.2	22.2
15	14.3	22.4	16.1	22.2
20	16.6	26.5	14.2	18.8
25	14.8	33.1	14.3	17.3

[a)] Average reduction in peak width (full width at half maximum, FWHM) and increase in resolution for the gradient separation of the eleven drugs (Figure 8).

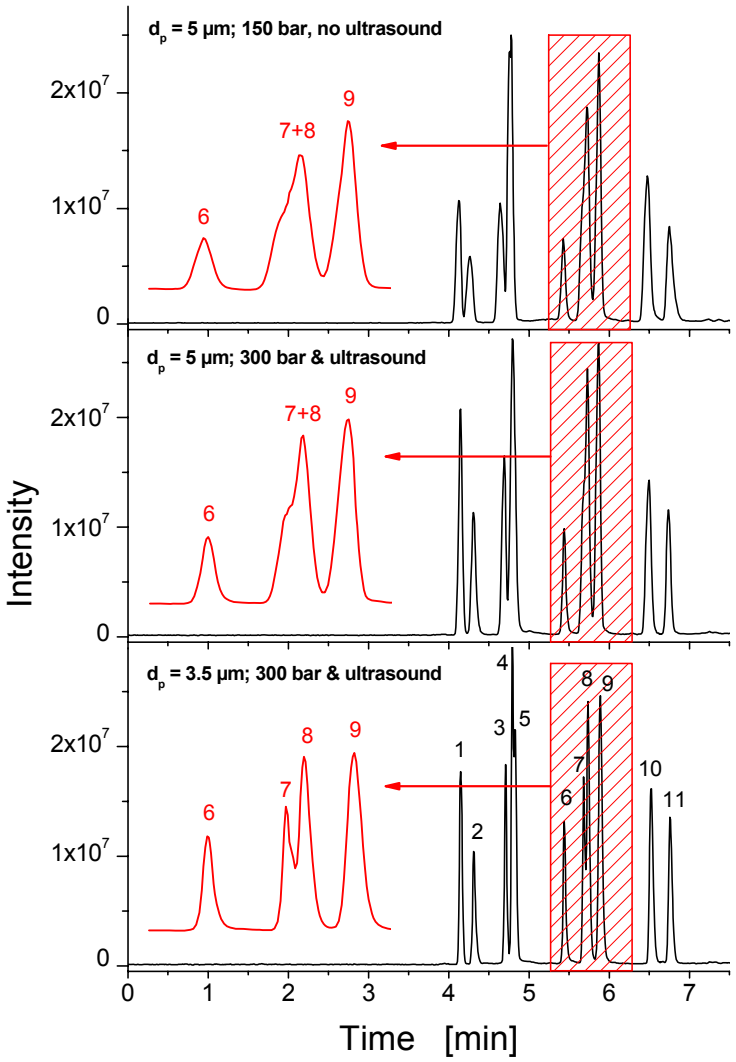

Figure 8: Separation of eleven drugs (1: nadolol, 2: atropine, 3: timolol, 4: metoprolol, 5: acebutolol, 6: labetalol, 7: propranolol, 8: alprenolol, 9: betaxolol, 10: imipramine, 11: trimipramine) on HPLC/MS chips packed under the indicated conditions. Mobile phase: 0.1% FA in water/acetonitrile. Gradient: 2-70% acetonitrile in 8 min. Flow rate: 500 nl/min. Injected volume: 1 µL. Sample concentration: 10 pg/µl of each drug. For peaks 6 to 9, peak width and resolution improve by 30% and 50%, respectively, from top to bottom chromatogram.

4 Conclusions

The chromatographic performance of HPLC/MS microchips (Figure 1) was studied in isocratic and gradient elution modes. Chips were packed under different conditions and with particles of different nominal size and compared with prototype HPLC/UV chips of similar design. Our data show that the analytical power of the HPLC/MS chip is limited by the quality of the chromatographic separation. The packing conditions significantly impact the packing density of the HPLC/MS chips (Figure 5 and Table 2), which determines their performance in both, isocratic (Figure 6) and gradient elution modes (Figures 7 and 8). Even with the steep

solvent gradients typical of HPLC/MS, the peak shape and chromatographic resolution for densely packed HPLC/MS chips are much improved (Table 4). For chips packed with 3.5 µm particles at 300 bar and ultrasonication we obtain dense packings (Table 2) and a good chromatographic performance (Table 3). The slope of the plate height curves at higher velocities is smaller for chips packed under optimal conditions (Figure 6a), enabling shorter analysis times without compromising resolution. The diminished efficiency of the HPLC/MS chips at low k'-values (Figure 6b) is explained by extra-column band broadening that occurs after the chromatographic separation.

References

[1] Janasek, D.; Franzke, J.; Manz, A *Nature* **2006**, *442*, 374-380.

[2] Rios, A. ; Escarpa, A.; González, M. C.; Crevillén, A. G. *Trends in Anal. Chem.* **2006**, *25*, 467-479.

[3] Ohno, K.; Tachikawa, K.; Manz A. *Electrophoresis* **2008**, *29*, 4443-4453.

[4] West, J.; Becker, M.; Tombrink, S.; Manz, A. *Anal. Chem.* **2008**, *80*, 4403-4419.

[5] Dittrich, P. S.; Manz, A. *Nat. Rev. in Drug Discov.* **2006**, *5*, 210-218.

[6] Freire, S. L. S.; Wheeler, A. R. *Lab Chip* **2006**, *6*, 1415-1423.

[7] Lazar, I. M.; Grym, J.; Foret, F. *Mass Spec. Rev.* **2006**, *25*, 573-597.

[8] Koster, S.; Verpoorte, E. *Lab on a Chip* **2007**, *7*, 1394-1412.

[9] Lee, J.; Soper, S. A.; Murray, K. K. *J. of Mass Spec.* **2009**, *44*, 579-593.

[10] Liu, J.; Ro, K. W.; Nayak, R.; Knapp, D. R. *Int. J. Mass Spect.* **2007**, *259*, 65-72.

[11] Freire, S. L. S.; Yang, H.; Wheeler, A. R. *Electrophoresis* **2008**, *29*, 1836-1843.

[12] Li, J. J.; Thibault, P.; Bings, N. H.; Skinner, C. D.; Wang, C.; Colyer, C.; Harrison, D. J. *Anal. Chem.* **1999**, *71,* 3036-3045.

[13] Bings, N. H.; Wang, C.; Skinner, C. D.; Colyer, C. L.; Thibault, P.; Harrison, D. J. *Anal. Chem.* **1999**, *71,* 3292-3296.

[14] Yin, H.; Killeen, K.; Brennen, R.; Sobek, D.; Werlich, M.; van de Goor, T. *Anal. Chem.* **2005**, *77*, 527-533.

[15] Xie, J.; Miao, Y.; Shih, J.; Tai, Y.-C.; Lee, T. D. *Anal. Chem.* **2005**, *77*, 6947-6953.

[16] Mellors, J. S.; Gorbounov, V.; Ramsey, R. S.; Ramsey, J. M. *Anal. Chem.* **2008**, *80*, 6881-6887.

[17] Ro, K. W.; Nayak, R.; Knapp, D. R. *Electrophoresis* **2006**, *27*, 3547-3558.

[18] Mair, D. A.; Geiger, E.; Pisano, A. P.; Fréchet, J. M. J.; Svec, F. *Lab Chip* **2006**, *6*, 1346-1354.

[19] Levkin, P. A.; Eeltink, S.; Stratton, T. R.; Brennen, R.; Robotti, K.; Yin, H.; Killeen, K.; Svec, F.; Fréchet, J. M. J. *J. Chromatogr. A* **2008**, *1200*, 55-61.

[20] Liu, J.; Chen, C.-F.; Tsao, C.-W.; Chang, C.-C.; Chu, C.-C.; DeVoe, D. L. *Anal. Chem.* **2009**, *81*, 2545-2554.

[21] Ishida, A.; Yoshikawa, T.; Natsume, M.; Kamidate, T. *J. Chromatogr. A* **2006**, *1132*, 90-98.

[22] Neue, U. D. *HPLC Columns: Theory, Technology, and Practice*. Wiley-VCH, New York, **1997**.

[23] Lazar, I. M.; Trisiripisal, P.; Sarvaiya, H. A. *Anal. Chem.* **2006**, *78*, 5513-5524.

[24] Shih, C.-Y.; Chen, Y.; Xie, J.; He, Q.; Tai, Y.-C. *J. Chromatogr. A* **2006**, *127*, 272-278.

[25] Gaspar, A.: Piyasena, M. E.; Gomez, F. A. *Anal. Chem.* **2007**, *79*, 7906-7909.

[26] Koesdjojo, M. T.; Koch, C. R.; Remcho, V. T. *Anal. Chem.* **2009**, *81*, 1652-1659.

[27] Ehlert, S.; Kraiczek, K.; Mora, J.-A.; Dittmann, M.; Rozing, G. P.; Tallarek, U. *Anal. Chem.* **2008**, *80*, 5945-5950.

[28] Jung, S.; Ehlert, S.; Mora, J.-A.; Kraiczek, K.; Dittmann, M.; Rozing, G. P.; Tallarek, U. *J. Chromatogr. A* **2009**, *1216*, 264-273.

[29] Oleschuk, R. D.; Harrison, D. J. *TrAC, Trends Anal. Chem.* **2000**, *19*, 379-388.

[30] Khirevich, S.; Höltzel, A.; Hlushkou, D.; Tallarek, U. *Anal. Chem.* **2007**, *79*, 9340-9349.

[31] Khirevich, S.; Höltzel, A.; Hlushkou, D.; Seidel-Morgenstern, A.; Tallarek, U. *Lab Chip* **2008**, *8*, 1801-1808.

[32] Khirevich, S.; Höltzel, A.; Ehlert, S.; Seidel-Morgenstern, A.; Tallarek, U. *Anal. Chem.* **2009**, *81*, 4937-4945.

[33] Vissers, J. P. C.; Claessens, H. A.; Laven, J.; Cramers, C. A. *Anal. Chem.* **1995**, *67*, 2103-2109.

[34] Dullien, F. A. L. *Porous Media – Fluid Transport and Pore Structure*. Academic Press, San Diego, **1991**.

[35] Hlushkou, D.; Tallarek, U. Transition from creeping via viscous-inertial to turbulent flow in fixed beds. *J. Chromatogr. A* **2006**, *1126,* 70-85.

[36] Melander, W. R.; Horváth, Cs. *High Performance Liquid Chromatography – Advances and Perspectives*. Academic Press, New York, **1980**.

[37] Guiochon, G. The limits of the separation power of unidimensional column liquid chromatography. *J. Chromatogr. A* **2006**, *1126,* 6-49.

[38] Gritti, F.; Felinger, A.; Guiochon, G. *J. Chromatogr. A* **2006**, *1136,* 57-72.

Chapter 6 - Improved particle-packed HPLC/MS microchips for proteomic analysis

1 Introduction

Progress in proteomics requires sensitive, selective analytical methods for high-throughput studies of target analytes. Encountered difficulties include a high sample complexity, limited sample amount, and a wide dynamic range in the concentration of cellular proteins. MS is an important analysis tool in proteomics because of its sensitivity and ability to identify proteins in combination with data base searches. Beside MALDI/MS, HPLC-ESI/MS is the most widely used method, enabling protein identification at high confidence levels [1, 2]. With the development of nanospray and recent progress in microfluidic technologies [3-5], nano-ESI provides an obvious interface between microfluidic chips and mass spectrometers, because the nanoliter to microliter per minute flow rates in microfluidics are a good match for nanoflow ESI sources [6-8].

Compared with conventional instrumentation, microfluidic chip-based systems have several attractive features for high-throughput applications such as proteomics: short analysis times (minutes or seconds), reduced sample consumption, and the possibility of parallelization and automation [9-11]. A critical point in chip-based HPLC-ESI/MS is chromatographic resolution (band broadening) of the device. Attention has been focused mainly on instrumental designs to minimize pre-column and post-column contributions to band broadening like dead-volume free sample injection schemes and a seamless ESI-tip integration [3]. The equally important minimization of the band broadening contribution from the chips separation column, however, has so far often been neglected. We therefore focused on the optimization of packing quality of the particle-packed separation channel in order to reduce the contribution from internal chromatographic band broadening to the overall performance of the chips. Although open-tubular and monolithic columns are in use, the predominating stationary support are packed beds of spherical silica-based particles of 3 to 5 µm diameter. Their popularity is mainly due to the wide range of surface modifications available for these particles.

The dense particulate packings required for high chromatographic resolution are much more difficult to attain with microfluidic chips than, e.g., with the cylindrical fused-silica capillaries used in nano-HPLC. This is partially due to the presence of corners and/or edges in the microchannels, whose noncylindrical cross-sectional geometry is intrinsic to their

fabrication process, but even more to the pressure sensitivity of most chips. High packing pressure and ultrasound are essential to obtain dense particulate beds in fused-silica capillaries as well as microchannels [12-14]. Separation channels of most LC-chips in the past were packed under sub-optimal conditions by applying only low to moderate pressures in order to prevent chip degradation [7, 15-18].

Recently, we have shown by extensive numerical simulation studies of flow and dispersion [19-21] how the density and the cross-sectional geometry of microchip packings affect their chromatographic resolution. The cross-sectional heterogeneity of noncylindrical particulate packings translates to an inhomogeneous flow distribution between the corner regions and the bulk and thus to increased band broadening. Experimentally [12, 14], we demonstrated with the separation of small organic molecules how packing conditions and packing density determine the chromatographic performance of HPLC chips.

With the technical difficulty of attaining densely packed particulate beds on microchips, good chromatographic performance of chip packings is not deemed important for some HPLC-MS applications. In high-throughput HPLC-MS analyses such as the screening of combinatorial chemistry libraries or proteomics, mobile phase gradients are typically applied. Steep gradients inevitably result in narrowed peaks and together with the resolving power of MS, especially MS/MS, the experimental conditions are often thought to compensate for a lack of packing quality. However, recently it was shown that even under these conditions peak shape and chromatographic resolution are much improved by dense chip packings [22]: HPLC/MS-chips packed with 5 μm particles at 150 bar without ultrasound had a bed porosity (interparticle void fraction) of 0.46 – which reflects a very loose packing – and a minimum isocratic reduced plate height of 2.9, whereas HPLC/MS-chips packed with 5 or 3.5 μm particles at 300 bar with ultrasound had bed porosities of 0.41 and 0.39, respectively, and a reduced plate height of 2.1. The quality of the latter chip packings was thus comparable to those of the packed fused-silica capillaries used in nano-HPLC. Furthermore, in gradient elution separations of a simple pharmaceutical drug mixture, for example, a peak width decrease of ~15% and a resolution increase of up to 33% were observed for chip packings with 5 μm particles at changing the packing conditions from 150 bar to 300 bar and ultrasound; with reduction of the particle size to 3.5 μm an additional decrease in peak width of ~15% and improved resolution up to 22% were achieved [22]. The concomitantly reduced slope of the plate height curves towards higher linear flow velocities enabled the application of higher flow velocities without a significant loss of chromatographic resolution, i.e., in effect shorter analysis times.

An increased chromatographic resolution implies increased signal intensities and a higher number of discrete, well-separated peaks, thus reducing co-elution and ion suppression. As a consequence, the number of identified proteins in complex biological

samples should also increase. In the present study, which builds on (and in this regard complements) our previous work [12, 14, 22] we tested this hypothesis with a carefully selected batch of standard Agilent HPLC/MS chips (Figure 1) by systematically varied packing conditions and particle sizes of the stationary phase. For the investigation of chromatographic performance a low-complexity sample of peptides from a tryptic BSA digest was used at different concentrations to evaluate the reproducibility, detection limits, peak capacities, and sequence coverage. The tryptic digest of a human plasma protein fraction (Cohn fraction IV-4) served as high-complexity sample to probe if the number of identified peptides in a proteomics sample depends on the packing conditions of the HPLC/MS chip.

2 Materials and methods

2.1 Chemicals and materials

Stationary phase packing materials Zorbax SB-C18 (C18-functionalized porous silica, non-endcapped) with a nominal particle size of 3.5 or 5 µm and a mean intraparticle pore size of 300 Å were from Agilent Technologies (Waldbronn, Germany). Tetrahydrofuran was from AppliChem GmbH (Darmstadt, Germany) and methanol and formic acid (FA) from Sigma-Aldrich Chemie GmbH (Taufkirchen, Germany). Human plasma protein fraction (Cohn fraction IV-4), dithiothreitol (DTT), acetonitrile, and iodoacetamide came from Sigma-Aldrich (St. Louis, MO, USA). $NaHCO_3$ and HPLC grade water (LiChrosolv®) were from Merck (Darmstadt, Germany) and urea from Roth (Karlsruhe, Germany). Sequencing grade trypsin was bought from Promega (Madison, WI, USA) and tryptic BSA peptides from New England Biolabs (Ipswich, MA, USA).

2.2 Microchip packing

For slurry packing of the separation channel of the HPLC/MS chips suspensions of 50 mg and 75 mg of the dry 5 µm and 3.5 µm Zorbax particles, respectively, were prepared in 1 mL tetrahydrofuran. Unpacked HPLC/MS chips were tightly fixed in a custom-built stainless-steel holder and connected to the packing apparatus as described earlier [23]. Packing pressures of 150 or 300 bar were applied with a WellChrom K-1900 pneumatic pump (Knauer GmbH, Berlin, Germany) equipped with a glass-lined metal tubing (500 µm ID) as slurry reservoir. After filling the slurry reservoir, the microchips were inserted into an ultrasonic bath and the packing procedure started with methanol as pushing solvent [24]. Ultrasound was switched off after 13 min and the system was slowly depressurized for at least 20 min. During the evaluation of the packing process we realized the general importance of ultrasound, but we could not document a clear influence of ultrasound frequency or power on the achieved bed densities. On the other hand, the extended application of ultrasound eventually became destructive for the laminated chip device and

separation channel (e.g., its application for more than 45 min at the pressure limit of about 350 bar within the stainless-steel holder). The enrichment channels on the HPLC/MS chips were subsequently packed with the 5 µm Zorbax SB-C18 particles at 150 bar. Before use, packed HPLC/MS chips were inspected under a microscope for gaps in the packing and damages in general.

2.3 Tryptic digest of a human plasma fraction and sample preparation

10 mg of a human plasma protein fraction were dissolved in 400 µL of 6 M urea. 5.2 µL of 100 mM DTT dissolved in 100 mM $NaHCO_3$ buffer (pH 8.3) were added, and the mixture was heated to 60°C for 10 min. After cooling to room temperature, 5.2 µL of 300 mM iodoacetamide dissolved in 100 mM $NaHCO_3$ buffer (pH 8.3) were added, and the mixture was incubated in the dark at ambient temperature for 30 min. Then, 1.7 mL of 100 mM $NaHCO_3$ buffer (pH 8.3) and 40 µL of 0.25 µg/µL trypsin were added, and the digest was performed at 37°C overnight. The reaction was stopped by adding FA to a final concentration of 0.2%.

For optimal sample preparation the tryptic peptides solution was desalted by reversed-phase chromatography on a micro-preparative HPLC system (SMART; GE Healthcare, Waukesha, WI, USA). After the salt was removed from the column by washing with 0.2% FA, the peptides were eluted with a gradient of 0–60% acetonitrile in 5 min. Peptide elution was monitored at a wavelength of 220 nm. Afterwards, the solvent was removed with a vacuum centrifugal evaporator (Jouan RC 1010, Thermo Scientific, Inc., Waltham, MA, USA). Tryptic peptides were dissolved in 0.2% FA at a concentration of 1 ng/µL, aliquoted, and frozen until analysis.

2.4 Liquid chromatography and tandem mass spectrometry

LC-MS/MS was performed on an Agilent HPLC-Chip-Cube MS interface equipped with a 1100 LC/MSD trap XCT Ultra ESI-ion trap mass spectrometer (Agilent Technologies, Palo Alto, CA, USA). A capillary pump attached to a micro well plate autosampler was used for sample injection. Gradient elution was performed with a nanoflow LC pump (1100 series Nanoflow LC System for MS, Agilent Technologies). Agilent ChemStation and MSD Trap Control software were used for system control and data acquisition.

Mobile phase gradients consisted of 0.2% FA (solvent A) and acetonitrile (solvent B). For analysis of tryptic BSA peptides, 1 µL of a 100 fmol/µL sample in solvent A was injected. For the dilution series, the tryptic BSA peptides sample concentration was diluted to 10 fmol/µL, 5 fmol/µL, and 1 fmol/µL. For analysis of tryptic digest of the human Cohn fraction IV-4, 8 µL of a 1 ng/µL sample in solvent A were injected. Samples were loaded from the autosampler onto the enrichment column of the HPLC/MS chips with a mobile phase of 2% solvent B at a

flow rate of 2 µL/min. The separation was performed with a gradient of 2–40% solvent B in 40 min at a flow rate of 400 nL/min.

Data were acquired in the positive ion mode with a voltage of -1.8 kV at the electrospray inlet capillary, a nitrogen drying gas flow of 4 L/min, and a temperature of 325°C at the transfer capillary for desolvation. The mass spectrometer was operated in a data-dependent mode in which the three most intense ions in the precursor ion scan were subjected to subsequent automated MS/MS. Doubly charged ions were preferably selected for fragmentation. Active exclusion was enabled after three cycles of MS/MS; the precursor ion was released from the exclusion after 1 min. All peptide separations were conducted in triplicates.

2.5 Data analysis

Raw MS/MS data were processed with Data Analysis Software for 6300 Series Ion Trap LC/MS Version 3.4 (Bruker Daltonics, Billerica, MA, USA). Data extraction was performed with the software's default setting except for the following variations: (1) for mass spectrum calculation, additional background subtraction for MS spectra using peak start and end spectra was performed; (2) after extraction of MS/MS data, spectra were deconvoluted using default parameters. Peptide identifications were performed with the Mascot software [25]. MS/MS datasets were used to search spectra against the mammal subset of the Swiss-Prot database [26] with trypsin as digesting enzyme. The search parameters included variable carbamidomethylation on cysteine residues and oxidation on methionine residues. A maximum of one missed cleavage was allowed during searches. The precursor ion mass tolerance was set to 1.2 Da, the fragment ion mass tolerance was ± 0.6 Da.

OMSSA [27] (version 2.1.4), X!Tandem [28] (version 08-02-01-3), and Mascot [25] (version 2.2.04) were used to identify the MS/MS spectra from the separation of the Cohn fraction IV-4 peptides. All human proteins of Swiss-Prot 55.4 were used as sequence database with a reversed version of each protein appended to the database [29]. The protease specificity was set to trypsin, allowing cleavages only after lysine and arginine, but not before proline. At maximum one missed cleavage was allowed during the searches. Oxidation of methionine and carbamidomethylation of cysteine residues were set as variable modifications. Charge states 2–4 were allowed for the precursor peptides. To determine the mass tolerances of the precursor peaks and the product ions, searches with mass tolerances of 3.0 Da for the precursor ion and 0.5 Da for the product ion were used. From the results of these searches, peptides with a false discovery rate (FDR, q-value) of 1% were extracted for each of the search engines separately. For the final searches, the precursor ion mass tolerance was set to 0.8 Da and the product ion mass tolerance to 0.25 Da. FDR statistics were carried out for each of the search engines and HPLC-MS runs separately. All peptides with a FDR of 1% or better were merged for each individual HPLC-MS run. A FDR of less

than 3% is expected for the merged results. In the worst case almost 3% FDR can be reached if the union of peptides of all search engines contains all target peptide sequences and the symmetric difference contains all decoy peptides. For every run, the number of unique peptide sequences was counted with differently modified peptides counting as separate sequences. The complete analysis was carried out using TOPP [30] version 1.6.

2.6 Peak capacity

The peak capacity is defined as the maximum number of peaks that fit in a chromatographic separation with an equal resolution. Recently, the theory of peak capacity has been further expanded to the separation of complex biological samples [31]. In this work, we focus on the conditional or sample peak capacity (n_c) of a specific region in the chromatogram, which can be determined by

$$n_c = \frac{t_{r,n} - t_{r,1}}{W}, \qquad (1)$$

where $t_{r,1}$ and $t_{r,n}$ are the retention times of the first and last peaks of interest and W is the average width of the peaks eluted in the retention window [32, 33]. Often, the first signal of interest is taken from the unretained tracer, whereas the last peak belongs to an analyte eluted under gradient conditions. In this work, we have defined the elution window boundaries and calculated the peak capacity from peaks within the window of retained peaks only [32, 34].

3 Results and discussion

Figure 1 illustrates the design of the standard Agilent HPLC/MS chip. The chip consists of three laminated polyimide foils of 125 µm (outer layers) or 50 µm (central layer) thickness. Microfluidic channels and the integrated ESI-tip were formed by direct laser ablation of the polyimide films (Figure 1B). While the capillary pump loads the sample from the autosampler onto the enrichment column, the nanoflow pump equilibrates the separation column with the starting mobile phase mixture (Figure 1A, enrichment). A motion to the left of the six-port valve starts dead-volume free elution of the analytes from the enrichment onto the separation column (Figure 1A, separation). Stationary phase particles inside enrichment and separation columns are retained by µ-sieves at the inlet and microfabricated frits at the outlet. Figure 1C depicts the packed separation channel cross-section and microfabricated ESI-tip adjacent to the separation column. HPLC/MS chips are positioned inside the Chip-Cube spray chamber between a counter electrode (end cap of the MS) and an additional electrode, orthogonal with respect to the MS inlet (Figure 1D).

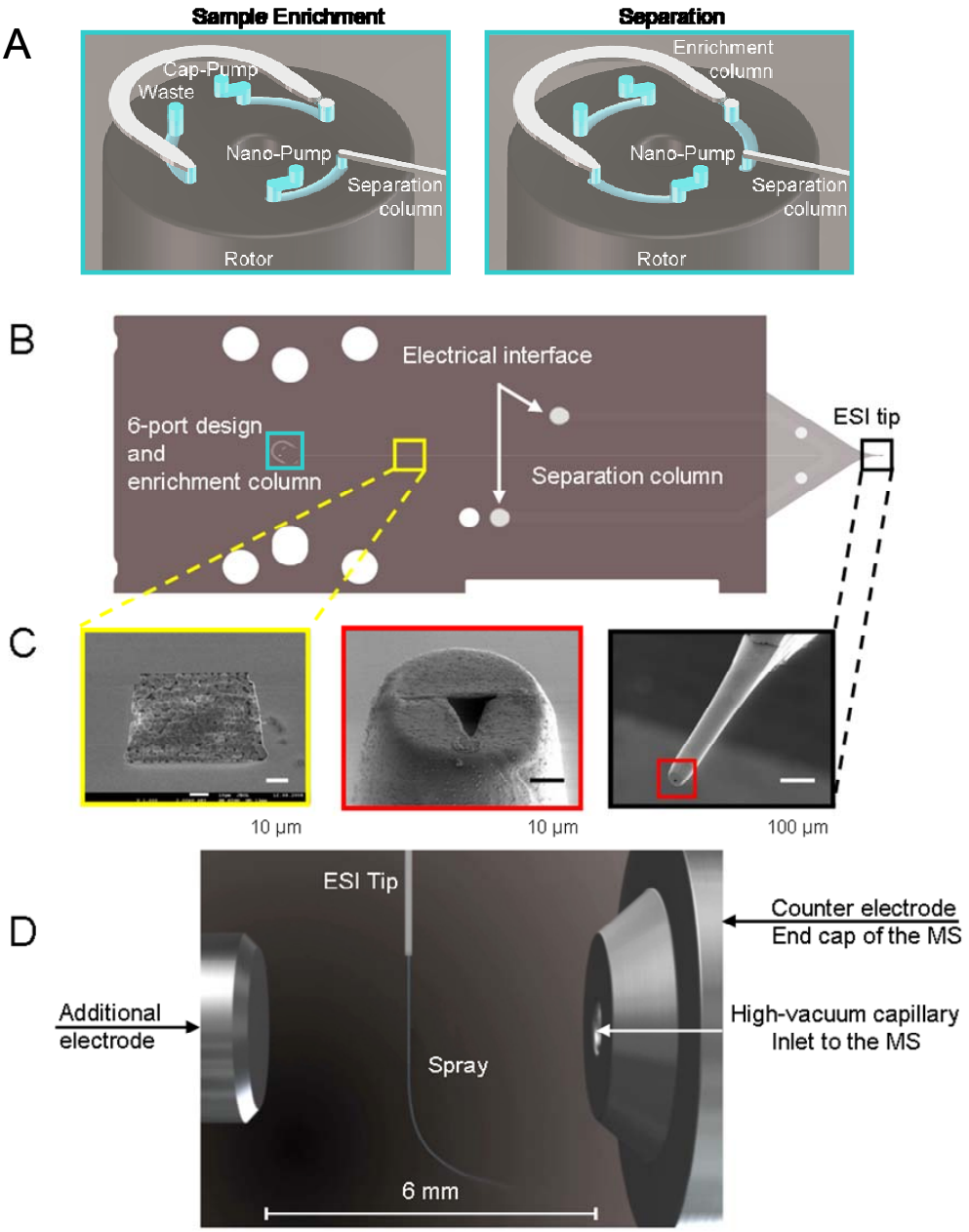

Figure 1: Design of the standard Agilent HPLC/MS-chip. (A) Schematic of the on-chip sample handling. (B) Layout of the polyimide-based microchip, integrating a sample enrichment channel and a 43 mm long separation channel packed with chromatographic material, and two internally grounded electrodes contacting the microfluidic channel near the ESI-tip. (C) Magnification of the packed channel cross section (75 µm x 50 µm), the ESI tip and its outlet. (D) Positioning of the microchip within the MS interface.

The separation channel of these chips was packed with C18-modified silica particles in the following three versions: i) 5 µm particles packed at 150 bar, ii) 5 µm particles packed at 300 bar with ultrasound, and iii) 3.5 µm particles packed at 300 bar with ultrasound. Gradient elution separation of tryptic peptides was detected with an ESI-ion trap mass spectrometer, which performed continuously repeating analysis cycles during the whole

separation period. First, a survey-scan mass spectrum was measured. Then, a precursor ion was selected by the data-dependent acquisition algorithm, isolated, fragmented, and fragment ions detected. In each analysis cycle at maximum three precursor ions were selected for fragmentation. The data from the fragmentation spectra of the peptide ions were searched against a protein database with search engines such as Mascot [25] to identify the corresponding amino acid sequences. The applied strategy is the standard in most proteomics approaches.

To evaluate the chromatographic performance of the different chip packings for biological samples of low complexity, a tryptic BSA digest was chosen. Figure 2 shows the separation of a 100 fmol sample of tryptic BSA peptides with the three different chip packings. For two representative packings each, base peak chromatograms (m/z 300-2000) of two individual separations are shown in an inverted mirror image representation for ease of comparison. The results illustrate excellent reproducibility of the separation for all chip packings. Improved packing conditions, i.e., using higher pressure and ultrasound, yield better chromatographic resolution with sharper peaks and higher signal intensities (Figure 2B compared with 2A). This effect is enhanced by using smaller (3.5 µm) stationary phase particles (Figure 2C).

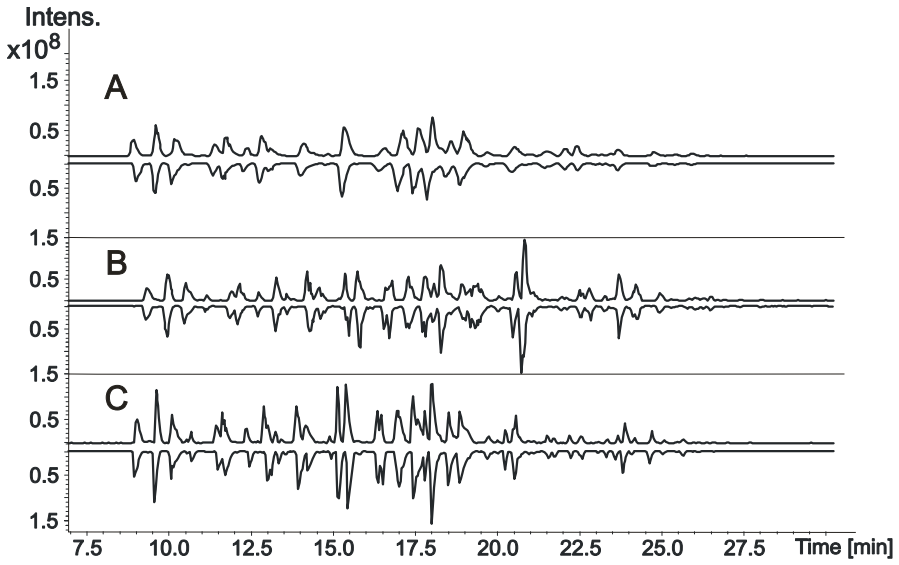

Figure 2: Two representative base peak chromatograms (BPC, m/z 300-2000) from the separation of 100 fmol tryptic BSA peptides with three different HPLC/MS-chip packings: (A) 5 µm particles packed at 150 bar without ultrasound; (B) 5 µm particles packed at 300 bar with ultrasound and (C) 3.5 µm particles packed at 300 bar with ultrasound. Mobile phase: 0.2% formic acid (solvent A) and acetonitrile (solvent B), 2-40% solvent B in 40 min at a flow rate of 400 nL/min.

Figure 3 compares the performance of the best (3.5 µm particles packed at 300 bar with ultrasound) and the worst (5 µm particles packed at 150 bar without ultrasound)

HPLC/MS chip packings with respect to decreasing sample amount. Base peak chromatograms (BPCs, m/z 300-2000) of the separation of tryptic BSA peptides are shown for sample amounts of 1, 5, and 10 fmol. The peaks in the BPCs from the optimized chip packing (right side of Figure 3) are better separated and of higher intensity. Additionally there are several peaks that are absent in the BPCs from the lower-quality chip packings. The latter effect is already apparent for the 10 fmol sample, but striking for the 1 fmol sample, where the optimized chip packing enables detection of a few peaks, whereas no peaks are observed with the lower-quality chip packings. The sequence coverage of BSA was analyzed for the separations shown in Figure 3 by a MASCOT database search (Table 1). With the optimized chip packings the sequence coverage increased by 20% for the 10 fmol sample, by 34% for the 5 fmol sample, and by 94% for the 1 fmol sample. However, a high run-to-run variability can be observed reflecting the stochastic nature of MS/MS data obtained by data dependent acquisition where peaks are automatically selected for fragmentation. As peak intensity underlies slight variations, this procedure may not pick the same peaks within repeated runs. This is of particular importance in the case of very low sample amounts where the peak intensity is low and might therefore fall below the threshold of MS/MS fragmentation or even below the detection limit. Because only a small number of peptides can be identified when using low peptide concentrations, the relative variability can be remarkable.

Figure 3 as well as Table 1 illustrate how much resolution and detection limit are improved by optimal packing conditions, but also demonstrate the *necessity* of optimal chip packings to detect small peaks or analyze low sample amounts, a typical situation in proteomic analysis [35, 36].

Table 1: Sequence coverage of tryptic BSA peptides as analyzed by gradient elution separations with HPLC/MS-chips packed under the indicated conditions.

	1 fmol BSA		**5 fmol BSA**		**10 fmol BSA**	
chip type	Sequence coverage	Average	Sequence coverage	Average	Sequence coverage	Average
5 µm particles packed at 150 bar without ultrasound	22%	11.3%	33%	37.0%	46%	45.0%
	8%		41%		45%	
	4%		37%		44%	
3.5 µm particles packed at 300 bar with ultrasound	21%	22.0%	51%	49.7%	52%	54.3%
	19%		47%		55%	
	26%		51%		56%	
Improvement		94%		34%		20%

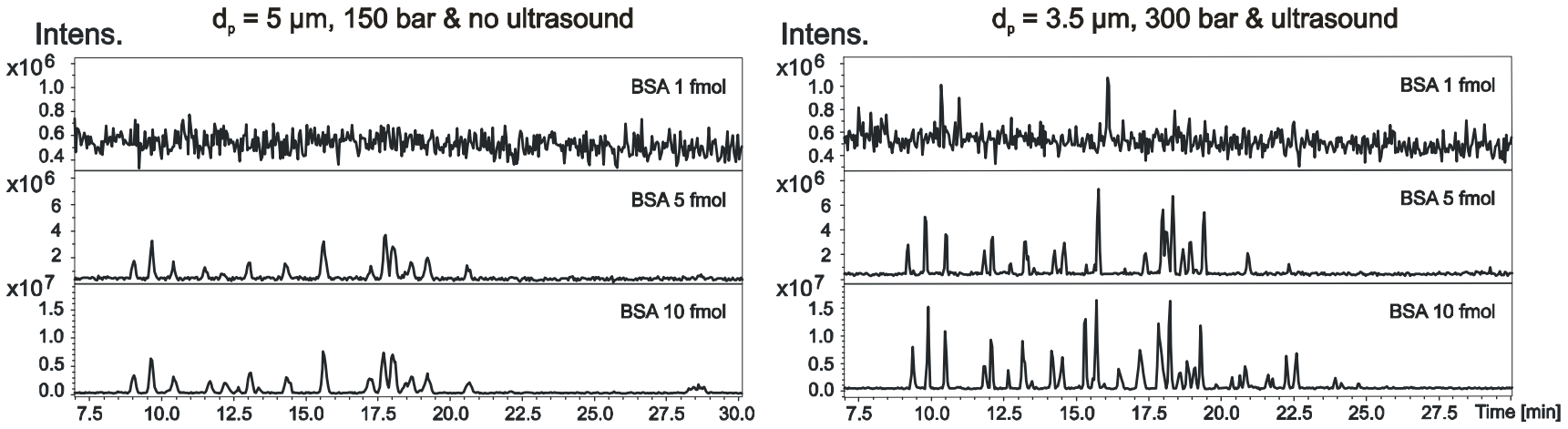

Figure 3: BPCs (m/z 300-2000) of a dilution series with 1, 5, and 10 fmol of tryptic BSA peptides separated with different HPLC/MS-chip packings. Mobile phase composition as indicated in Figure 2.

Apart from small sample amounts, high sample complexity is another challenging problem in proteomics. Complex mixtures of thousands of proteins yield thousands of peptides after the tryptic digestion. Also, the relative abundance of proteins in a sample spans a wide dynamic range, with an order of magnitude of 12 in the case of plasma proteins [37]. The performance of the different HPLC/MS chip packings was therefore evaluated with a proteomics sample of very high complexity, the tryptic digest of a human plasma protein fraction, the Cohn fraction IV-4 [38, 39].

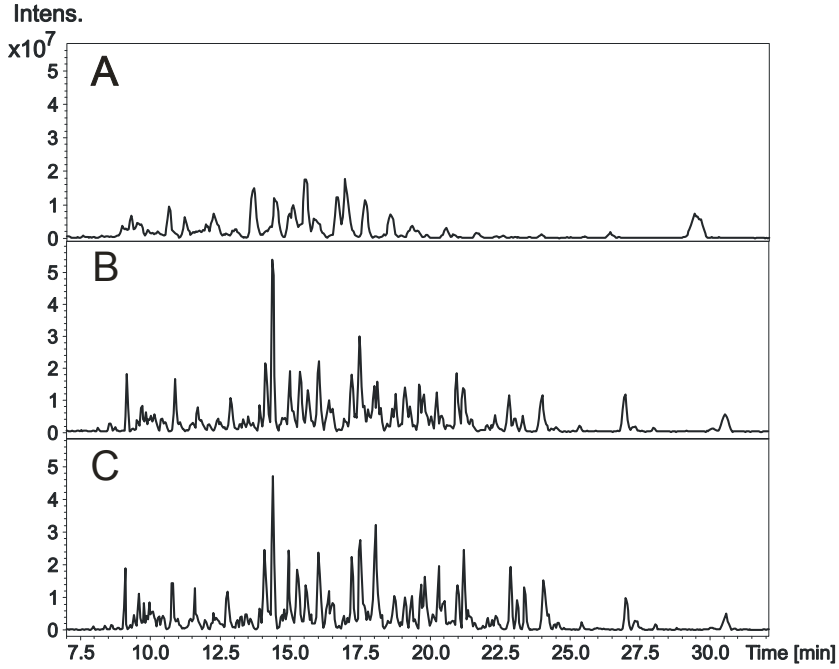

Figure 4: BPCs (m/z 300-2000) of 8 ng tryptic peptides of a human plasma protein fraction (Cohn IV-4) separated with different HPLC/MS-chip packings: (A) 5 µm particles packed at 150 bar without ultrasound; (B) 5 µm particles packed at 300 bar with ultrasound and (C) 3.5 µm particles packed at 300 bar with ultrasound. Mobile phase composition as indicated in Figure 2.

Figure 4 compares BPCs (m/z 300-2000) of the separation of an 8 ng sample of tryptic digest of Cohn fraction IV-4 obtained with the different HPLC/MS chip packings. The BPCs in Figures 4B and 4C show a significantly narrowed peak width and enhanced signal intensity compared with the BPC from the lower-quality chip packing (Figure 4A). The higher chromatographic resolution yields a larger number of discrete peaks and also a higher number of identified peptides, as compiled in Table 2. For each type of chip packing, two representative individual HPLC/MS chips were tested, and each separation was carried out in triplicate. The average of the triplicate is indicated in Table 2 as well as the overall average of all runs for each packing type. The reproducibility of the number of identified peptides for each packing type is within the range for identifications of peptide mixtures by LC-MS/MS with data-dependent acquisition [40]. With lower-quality HPLC/MS chip packings, consisting of 5 µm particles packed at 150 bar, an average of 126 peptides from the tryptic digest was

identified. Increasing the packing pressure to 300 bar and the assistance of ultrasound raised the average number of identified peptides by 13% to 143. Using a smaller particle size of 3.5 µm along with the optimized packing process conditions finally enabled identification of an average number of 175 peptides from the tryptic digest, an improvement by 22% and 39% compared with the former chip packing types, respectively.

Table 2: Number of identified peptides from the tryptic digest of human plasma protein fraction (Cohn fraction IV-4) as analyzed by gradient elution separations with HPLC/MS-chips packed under the indicated conditions.

	Chip number 1		**Chip number 2**			
chip type	Identified Peptides	Average	Identified Peptides	Average	Allover average	Improvement*
5 µm particles packed at 150 bar without ultrasound	106	112	148	140	126	
	101		154			
	129		118			
5 µm particles packed at 300 bar with ultrasound	80	132	161	154	143	13%
	174		158			
	142		142			
3.5 µm particles packed at 300 bar with ultrasound	182	177	171	173	175	39%
	172		170			
	178		178			

*** Improvement compared with chip type: 5 µm particles packed at 150 bar without ultrasound.**

The automatic precursor selection in MS/MS-analyses is algorithm-controlled and usually activated by ion signal intensity levels. These, however, depend on the concentration of the peptides in the sample and the width of the chromatographic peaks [41]. In the separation of complex peptide mixtures from tryptic digestion of proteomes co-elution of peaks is common. Therefore, it is particularly important to improve the separation of the tryptic peptides *before* their injection into the mass spectrometer. A good separation guarantees a higher number of identified peptides. The pronounced increase in the number of identified peptides in the tryptic digest of the plasma protein fraction (Table 2) undoubtedly underlines the relationship between chromatographic resolution and number of identified peptides.

Experimental peak capacities representing the different packing conditions are summarized in Table 3. They were calculated with Eq. (1) by taking the average peak width at 4σ from the extracted ion chromatograms. Table 3 demonstrates reasonable peak

capacities for the analyzed samples under the applied gradient elution conditions. The peak capacities improve significantly with the optimized packing conditions, similar to the sequence coverage and peptide identification data in Tables 1 and 2. With respect to the 5 µm particles packed at 150 bar without ultrasound we find a relative improvement in peak capacity of about 37-41% and 76-94% for the different BSA concentrations and nearly 58% and 89% for the Cohn fraction, when the 5 and 3.5 µm particles are packed at 300 bar with ultrasound, respectively. For 1 fmol of the BSA digest no peak capacity was calculated due to an insufficient number of analyzable peaks (the average peak width would be based on an inadequate number of peaks), especially for the worst packing. The peak capacities reported in Table 3 show good agreement with those from a recent publication which investigated a BSA digest under comparable chromatographic conditions with analytical columns and 3 and 5 µm particles [34].

Table 3. Peak capacities and peak widths as analyzed by gradient elution separations with HPLC/MS chips packed under the indicated conditions.

		BSA digest			Cohn fraction IV-4 digest		
Chip type	Sample amount [fmol]	Peak capacity [-]	Improvement*	Peak width at 4σ [min]	Peak capacity [-]	Improvement*	Peak width at 4σ [min]
5 µm particles packed at 150 bar without ultrasound	100	42.5	n.a.	0.4233	45.4	n.a.	0.4932
	50	46.5		0.3872			
	10	50.1		0.3593			
	5	50.3		0.3582			
5 µm particles packed at 300 bar with ultrasound	100	59.8	40.7%	0.3008	71.6	57.6%	0.3185
	50	64.1	37.8%	0.2810			
	10	68.6	36.9%	0.2625			
	5	71.0	41.2%	0.2537			
3.5 µm particles packed at 300 bar with ultrasound	100	77.3	81.7%	0.2360	85.8	88.9%	0.2676
	50	90.3	94.3%	0.2012			
	10	94.2	88.1%	0.1740			
	5	88.4	76.0%	0.1855			

*** Improvement compared with chip type: 5 µm particles packed at 150 bar without ultrasound.**

4 Concluding remarks

The analysis of complex mixtures of tryptic peptides with the HPLC/MS chips improves when optimal packing parameters and a small particle size of the stationary phase are used for the chip's noncylindrical separation channel. Based on our previous work [12, 14, 19, 21] this improvement can be rationalized by the combination of a reduced transcolumn velocity bias (due to denser chip packings which minimize the effects of wall and particularly corner regions on the bed heterogeneity) and the smaller size of the totally

porous particles, which reduces intraparticle mass transfer resistance and also allows to better fill the corner regions of the chips separation channel. Both effects, i.e., the smaller transcolumn velocity bias and the smaller intraparticle mass transfer resistance reduce the slope of isocratic plate height curves towards higher linear flow velocities and therefore enable higher velocities without significant loss of chromatographic resolution, i.e., in effect shorter analysis times.

For the proteomic samples analyzed in the present work the enhanced chromatographic performance of the separation increases the peak capacity, the number of identified peptides within a tryptic digest, and thus protein identification. The benefits of optimized chip packings are especially important for analysis of small sample amounts. Our results demonstrate that even with *steep* mobile phase gradients and the resolving power of MS/MS as detector, the quality of the chromatographic separation is at the core of a successful analysis of the complex samples typical in proteomics.

References

[1] Lazar, I. M.; Grym, J.; Foret, F. *Mass Spectrom. Rev.* **2006**, *25*, 573-594.

[2] Smith, R. D.; Shen, Y. F.; Tang, K. Q. *Acc. Chem. Res.* **2004**, *37*, 269-278.

[3] Coster, S.; Verpoorte, E. *Lab Chip* **2007**, *7*, 1394-1412.

[4] Lee, J.; Soper, S. A.; Murray, K. K. *J. Mass Spectrom.* **2009**, *44*, 579-593.

[5] Wilm, M. S.; Mann, M. *Int. J. Mass Spectrom. Ion Process.* **1994**, *136*, 167-180.

[6] Liu, J.; Ro, K. W.; Nayak, R.; Knapp, D. R. *Int. J. Mass Spectrom.* **2007**, *259*, 65-72.

[7] Xie, J.; Miao, Y.; Shih, J.; Tai, Y. C.; Lee, T. D. *Anal. Chem.* **2005**, *77*, 6947-6953.

[8] Yin, H.; Killeen, K.; Brennen, R.; Sobek, D.; Werlich, M.; van de Goor, T. *Anal. Chem.* **2005**, *77*, 527-533.

[9] Mair, D. A.; Geiger, E.; Pisano, A. P.; Fréchet, J. M. J.; Svec, F. *Lab Chip* **2006**, *6*, 1346-1354.

[10] Reichmuth, D. S.; Shepodd, T. J.; Kirby, B. J. *Anal. Chem.* **2005**, *77*, 2997-3000.

[11] Ehlert, S.; Tallarek, U. *Anal. Bioanal. Chem.* **2007**, *388*, 517-520.

[12] Ehlert, S.; Kraiczek, K.; Mora, J.-A.; Dittmann, M.; Rozing, G. P.; Tallarek, U. *Anal. Chem.* **2008**, *80*, 5945-5950.

[13] Ehlert, S.; Rösler, T.; Tallarek, U. *J. Sep. Sci.* **2008**, *31*, 1719-1728.

[14] Jung, S.; Ehlert, S.; Mora, J.-A.; Kraiczek, K.; Dittmann, M.; Rozing, G. P.; Tallarek, U. *J. Chromatogr. A* **2009**, *1216*, 264-273.

[15] Gaspar, A.; Piyasena, M. E.; Gomez, F. A. *Anal. Chem.* **2007**, *79*, 7906-7909.

[16] Koesdjojo, M. T.; Koch, C. R.; Remcho, V. T. *Anal. Chem.* **2009**, *81*, 1652-1659.

[17] Lazar, I. M.; Trisiripisal, P.; Sarvaiya, H. A. *Anal. Chem.* **2006**, *78*, 5513-5524.

[18] Shih, C. Y.; Chen, Y.; Xie, J.; He, Q.; Tai, Y. C. *J. Chromatogr. A* **2006**, *127*, 272-278.

[19] Khirevich, S.; Höltzel, A.; Ehlert, S.; Seidel-Morgenstern, A.; Tallarek, U. *Anal. Chem.* **2009**, *81*, 4937-4945.

[20] Khirevich, S.; Höltzel, A.; Hlushkou, D.; Seidel-Morgenstern, A.; Tallarek, U. *Lab Chip* 2008, *8*, 1801-1808.

[21] Khirevich, S.; Höltzel, A.; Hlushkou, D.; Tallarek, U. *Anal. Chem.* **2007**, *79*, 9340-9349.

[22] Ehlert, S.; Trojer, L.; Vollmer, M.; van de Goor, T.; Tallarek, U. *J. Mass Spectrom.* **2010**, *45*, 313-320.

[23] Chen, G.; Pačes, M.; Marek, M.; Zhang, Y.; Seidel-Morgenstern, A.; Tallarek, U. *Chem. Eng. Technol.* **2004**, *27*, 417-428.

[24] Vissers, J. P. C.; Claessens, H. A.; Laven, J.; Cramers, C. A. *Anal. Chem.* **1995**, *67*, 2103-2109.

[25] Perkins, D. N.; Pappin, D. J.; Creasy, D. M.; Cottrell, J. S. *Electrophoresis* **1999**, *20*, 3551-3567.

[26] Boeckmann, B.; Bairoch, A.; Apweiler, R.; Blatter, M. C.; Estreicher, A.; Gasteiger, E.; Martin, M. J.; Michoud, K.; O'Donovan, C.; Phan, I.; Pilbout, S.; Schneider, M. *Nucleic Acids Res.* **2003**, *31*, 365-370.

[27] Geer, L. Y., Markey, S. P., Kowalak, J. A., Wagner, L., Xu, M.; Maynard, D. M.; Yang, X. Y.; Shi, W. Y.; Bryant, S. H. *J. Proteome Res.* **2004**, *3*, 958-964.

[28] Craig, R.; Beavis, R. C. *Bioinformatics* **2004**, *20*, 1466-1467.

[29] Elias, J. E. Gygi, S. P. *Nat. Methods* **2007**, *4*, 207-214.

[30] Kohlbacher, O.; Reinert, K.; Gröpl, C.; Lange, E.; Pfeifer, N.; Schulz-Trieglaff, O.; Sturm, M. *Bioinformatics* **2007**, *23*, e191-197.

[31] Neue, U. D. *J. Chromatogr. A* **2008**, *1184*, 107-130.

[32] Dolan, J. W.; Snyder, L. R.; Djordjevic, N. M.; Hill, D. W.; Waeghe, T. J. *J. Chromatogr. A* **1999**, *857*, 1-20.

[33] Wang, X.; Barber, W. E.; Carr, P. W. *J. Chromatogr. A* **2006**, *1107*, 139-151.

[34] Fairchild, J. N.; Walworth, M. J.; Horváth, K.; Guiochon, G. *J. Chromatogr. A* **2010**, *1217*, 4779-4783.

[35] Shen, Y.; Tolić, N.; Masselon, C.; Pasa-Tolić, L.; Camp, D. G.; Hixson, K. K.; Zhao, R.; Anderson, G. A.; Smith, R. D. *Anal. Chem.* **2004**, *76*, 144-154.

[36] Waanders, L. F.; Chwalek, K.; Monetti, M.; Kumar, C.; Kumar, C.; Lammert, E.; Mann, M. *Proc. Natl. Acad. Sci. U S A* 2009, *106*, 18902-18907.

[37] Anderson, N. L.; Anderson, N. G. *Mol. Cell. Proteomics* **2002**, *1*, 845-867.

[38] Ahrends, R.; Lichtner, B.; Bertsch, A.; Kohlbacher, O.; Hildebrand, D.; Trusch, M.; Schlüter, H. *J. Chromatogr. A* **2010**, *1217*, 3321-3329.

[39] Cohn, E. J.; Oncley, J. L.; Strong, L. E.; Hughes, W. L.; Armstrong, S. H. *J. Clin. Invest.* **1944**, *23*, 417-432.

[40] Tabb, D. L.; Vega-Montoto, L.; Rudnick, P. A.; Variyath, A. M.; et al. *J. Proteome Res.* **2010**, *9*, 761-776.

[41] Liu, H.; Sadygov, R. G.; Yates, J. R. Anal. Chem. 2004, 76, 4193-4201.

Conclusions

This work is explaining the importance of generating a densely packed chromatographic bed to achieve optimum separation efficiency in miniaturized liquid chromatography. The reduction of peak dispersion and enhancement of separation efficiency is the important problem in micro- and nano-separation that is to be solved to generate highly efficient chromatographic systems that can exploit all advantages of miniaturization. Therefore, the influence of the geometrical wall effect in cylindrical nanobore columns and its influence to the obtained packing porosities were determined, by varying the column diameter from 30 µm to 250 µm and constant particle diameter (5 µm) (*Chapter 2*). In addition, two independent porosity data generating chromatographic approaches based on inverse size exclusion and Donnan exclusion chromatography were investigated, to prove the reliability of the porosity data (*Chapter 3*). *Chapter 4* is explaining the optimization of the Agilent chromatographic chip system packing process by varying the packing conditions (pressure and implementation of ultrasound) and provides an experimental analysis and consistent interrelation of the packing procedure, resulting packing density (interparticle porosity), pressure drop over the packed inherent noncylindrical microchannel, and separation efficiency. The data revealed a significant improvement in separation efficiency with improved bed porosity received at different packing conditions. This was evaluated by use of isocratic measure of plate height curves. *Chapter 5 and 6* investigated the enhanced separation efficiencies based on the improved bed porosities under isocratic and gradient elution conditions for small pharmaceutical molecules and more complex biological applications (BSA and Human plasma protein fraction; Cohn fraction IV-4) with the Agilent high performance liquid chromatography mass spectrometry chip system. The data showed that the separation efficiency and identification of peptides is significantly improved, even under gradient elution with continuously improved bed porosities. The improvement in peak width and resolution lead to better identifications and quantification of the more complex biological chromatographic problem.

In particular, this work provides evidence for the operation of a geometrical wall effect in slurry-packed capillaries in a range of capillary diameter (d_c) to particle diameter (d_p) ratios of $5 < d_c/d_p < 50$ (*Chapter 2 - Packing density of slurry-packed capillaries at low aspect ratios*). Packing densities are assessed by a polystyrene standard which is size-excluded from the intraparticle pore space of the packings [1, 2]. It is noted first that, as expected, the values for the intraparticle porosity ($\varepsilon_{intra} \approx 0.29$) remain independent of d_c/d_p because the available intraparticle pore space with respect to the overall particle volume for rigid particles should remain unaffected by the actual density of a packed bed. In contrast, the packed

beds external porosity shows a steady decrease from $\varepsilon_{inter} \approx 0.47$ at $d_c/d_p = 5$ towards $\varepsilon_{inter} = 0.36\text{-}0.37$ at $d_c/d_p = 40\text{-}50$. This systematic increase in ε_{inter} (interparticle porosity) and ε_{total} (total porosity) at decreasing capillary diameter (or in other words decreasing d_c/d_p) lends support to the operation of a geometrical wall effect which affects and even limits the achievable packing density due to the inherent oscillations of interparticle voidage in a transition region between the hard inner surface of the fused-silica capillaries and the bulk, random-close packing of particles, if the latter can be reached at all which depends on the actual d_c/d_p-ratio. When the volumetric contribution of this critical wall region to the overall volume of the packed bed becomes significant, the interparticle porosity is expected to increase. This interplay between a more loosely packed wall region and a more tightly packed core region forms the basis for explaining the improved performance of fused-silica capillaries packed with 5 µm-sized porous C18-silica particles in the work of Jorgenson and co-workers [3, 4] as the capillary inner diameter is decreased from 50 to 12 µm. With such a decrease in aspect ratio the core region ultimately disappears and the packing structure is dominated by the loosely packed wall region; the packing structure becomes effectively more homogeneous.

This thesis also presents a very simple, fast, and reliable approach for the analysis of packing densities by using the interparticle Donnan (electrostatic) exclusion method (*Chapter 3 - Determination of the interparticle void volume in packed beds via intraparticle Donnan exclusion*). Therefore, interparticle void volumes (V_{inter}) and porosities (ε_{inter}) of particle-packed beds within 75 µm i.d. fused-silica capillaries have been determined. The theory of electrostatic exclusion provides a clear, physically sharp definition of the boundary conditions between (charge-selective) mesopore space and (charge-nonselective) macropore space in porous media like packed beds. Hence, a complete intraparticle Donnan exclusion of an unretained co-ionic tracer (nitrate ions) was established and used to determine the porosity of the investigated packed beds with different pore and particle sizes, and with different surface modifications (bare silica, reversed-phase, and strong cation-exchange materials) or surface charge densities of the particles, in dependence of the mobile phase ionic strength (Tris-HCl buffer). This approach allowed the investigation of donnan exclusion of the charged analyte based on the electrical double layer (EDL) overlap under the aforementioned conditions. The determined interparticle porosities agreed well with those analyzed by inverse size-exclusion chromatography (ISEC) [2]. Limitations to the use of Donnan exclusion (electrostatic exclusion) and ISEC (mechanical exclusion) arose from the same principle. Exclusion becomes noticeable in the cusp regions between particles if the particles became very small (3 µm or less) in conjunction with a low bed porosity, and when the intraparticle pore diameter is so large that complete electrostatic and size exclusion is difficult to realize. Nevertheless, this simple and fast technique provides

reliable porosity data and can be used for, e.g., quality control of packed conduits, if the particle packed beds are investigated due to the applicability of this approach.

Based on the findings in *chapter 2 and 3,* this work also provides an experimental analysis and consistent interrelation of the packing procedure, resulting packing density (interparticle porosity), pressure drop over the packed inherent noncylindrical microchannel, and separation efficiency under both isocratic and gradient elution conditions for packed beds employed in microchip-HPLC (High Performance Liquid Chromatography) (*Chapter 4 Chapter 4 - Separation Efficiency of Particle-Packed HPLC-Microchips*). First, a new prototype HPLC/UV-microchip design was developed based on the commercial HPLC/MS (mass spectrometry) microchips, to ensure a suitable porosity measurement of the established beds. This became necessary due to the used ISEC-method [2] which needed an UV-detection mode and was not applicable with MS. The size excluded polystyrene standards reflecting the bed porosity in a chromatographic run, were not able to be ionized with the electrospray ionization (ESI) mode used with the commercially available microchips. Therefore an almost dead volume free on-chip UV-detection was implemented to overcome this issue. Both chip types had a high, comparable ratio of the separation channel volume (packed conduit) to the chip dead volume (on chip external volume) of about 110 for the HPLC/UV chip design and 150 for the HPLC/MS chip design. This allowed investigating the two different chip systems more in detail without remarkable aberrations in external contributions (external band broadening on-chip).

In particular, it is demonstrated that the separation channels of suitable microfluidic analysis systems, which often cannot tolerate the high packing pressures used in conventional column packing and the application of ultrasound, can be packed as densely as the cylindrical fused-silica capillaries commonly used in nano-HPLC (ε_{inter} = 0.42, with 5 µm-size packing materials) (*Chapter 4 - Separation Efficiency of Particle-Packed HPLC-Microchips*). The achieved packing densities were comparable to those in nano-HPLC for capillary columns characterized by similar column-to-particle size ratios as the trapezoidal microchip separation channels when packed with the same particles. A consistent decrease in ε_{inter} of the microchips with increasing separation efficiency was found. ε_{inter} decreased in the following series of packing modes: 150 bar > 150 bar & ultrasound > 300 bar > 300 bar & ultrasound being accompanied by a decrease in plate height by a factor of about three (with 80/20 acetonirtile/water (v/v)) from the microchip packed at 150 bar (ε_{inter} = 0.475) to the one packed at 300 bar and with ultrasound assistance (ε_{inter} = 0.42) for the particles with 5 µm size. These complementary data confirm that the improvement in separation efficiency can be explained by higher packing densities achieved by the increased packing pressure and simultaneous application of ultrasound [5].

For a final comparison of the data determined with the prototype HPLC/UV chips, the HPLC/MS chips were packed in analogy to the developed packing procedure of the HPLC/UV chips (*Chapter 5 - Performance of HPLC/MS microchips in isocratic and gradient elution modes*). The data clearly showed the same trend, as expected. The packing porosity decreased for the MS chips from $\varepsilon_{inter} \approx 0.46$ (150 bar) to $\varepsilon_{inter} \approx 0.41$ (300 bar & ultrasound) for the 5 µm particles. For the investigated 3.5 µm particles, bed porosities of $\varepsilon_{inter} = 0.40$ (UV chips) and $\varepsilon_{inter} \approx 0.39$ (MS chips) were found. The slightly different porosities determined could be explained by the difference in separation channel lengths (UV chips 73 mm and MS chips 43 mm) which generated a different pressure drop over the length during the packing procedure favoring the MS chips. The separation efficiency was investigated by using octanophenone at 50/50 acetonitrile/water (v/v) at a k' = 28 (HPLC/MS) and k' = 35 (HPLC/UV). The decreased retention on the HPLC/MS chips with the same stationary and mobile phases is a consequence of the elevated temperature inside the MS-chip-cube compartment (313 ± 1 K) [6], while the separations with the prototype HPLC/UV chips were carried out at 298 ± 1 K. Both ultrasound and high pressure are crucial during packing to obtain improved separation efficiencies, where the minimum of the plate height curves (H_{min}) is shifted to lower plate heights and higher velocities. For chips packed with 3.5 µm particles at 300 bar and ultrasonication a good chromatographic performance was obtained as reflected by the reduced minimum plate heights of $h_{min} = 2.5$ (HPLC/UV) and $h_{min} = 2.1$ (HPLC/MS). Even more important, the slope of the plate height curves at higher velocities is smaller for the chips packed under optimal conditions, enabling shorter analysis times without significant reduction of resolution. Surprisingly, the separation efficiency for the HPLC/MS chips at low k'-values was significantly reduced compared to the HPLC/UV chips. Both compartments showed a k' dependent separation efficiency, but the HPLC/MS chips revealed a much stronger one at low k' than the HPLC/UV chips. Assuming that the injection process and the separation channel to on chip dead volumes were comparable, the diminished efficiency of the HPLC/MS is explained by extra-column band broadening that occurs after the chromatographic separation. While external contributions to peak dispersion have a constant value, their relative contribution to peak width became less pronounced at high k'-values where the peak is more dispersed due to its longer residence time inside the separation conduit [6].

The trend of increased separation efficiencies with the packing quality is also clearly confirmed under gradient elution conditions. For the investigated pharmaceutical test mixtures the resolution and peak width is remarkably improved with decreased bed porosities. Even for steep gradients, the peak width is decreased by ~15% and the resolution is increased by ~20% after changing the packing conditions from 150 bar without ultrasound to 300 bar and ultrasound for the 5 µm particles. Reduction of particle size from 5

to 3.5 µm decreased the peak width further by ~15% and increased the resolution by ~20%. These findings correspond to the results from the isocratic elution experiments and demonstrate that the analytical performance of the HPLC/MS chip is critically affected by the quality of the chromatographic separation even under gradient elution conditions.

Last but not least, the separation efficiency with a low complexity (BSA tryptic digest) and a highly complex (Cohn4-IV fraction digest) biological samples were investigated (*Chapter 6 - Improved particle-packed HPLC/MS microchips for proteomic analysis*). The improved packing quality led to four trends important for the field application. First, the reproducibility of independently accomplished separation improved with the packing quality, which is favorable for the longtime investigations and process control. Secondly, it was possible to reduce the lower limit of quantification (LOQ) for the BSA digest from 10 fmol for the 5 µm particles packed with 150 bar to 1 fmol for the packings packed at 300 bar and with ultrasound (3.5 µm). The impressive improvement in peak width and resolution led to a significantly reduced co-elution of peaks and therefore to a better quantification due to the detection of discrete (independent) peaks. Thirdly, because the higher chromatographic resolution yields a larger number of discrete peaks it was also possible to identify a higher number of peptides with the complex biological probe (Cohn4-IV fraction digest). However, the optimized packing conditions for the 3.5 µm particles enabled an average number of 175 identified peptides from the tryptic digest, an improvement by 22% and 39% compared with the chips packed with 5 µm and 150 bar and those with 5 µm, 300 bar and ultrasound, respectively. Fourth, the peak capacities improve significantly with the optimized packing conditions, similar to the sequence coverage and peptide identification data. With respect to the 5 µm particles packed at 150 bar without ultrasound it was found a relative improvement in peak capacity of about 37-41% and 76-94% for the different BSA concentrations and nearly 58% and 89% for the Cohn fraction, when the 5 and 3.5 µm particles are packed at 300 bar with ultrasound, respectively.

To conclude, this work demonstrates the fundamental importance to generate a densely packed chromatographic bed to achieve an excellent, reliable and reproducible chromatographic performance. A lower porosity (denser bed) leads to significantly improved separation efficiency especially in inherently noncylindrical conduits. Basically, under gradient elution conditions, widely used in the pharmaceutical industry, the improved peak width and resolution lead to better identifications, peak capacities and quantification mainly for complex matrices. However, it is possible to generate packing densities comparable to widely used cylindrical nanobore columns, the only restriction is made by the stability of the microfabricated conduit, whether it can withstand high packing pressures. The application of ultrasound particularly for low aspect ratio conduits is crucial for the generation of a densely packed separation channel. Taking this as a basis, the effect of miniaturization and

integration of chromatography onto single devices (micro total analyzing systems; μTAS) and all its positive contributions due to reduction of band broadening and traveled distances for the analytes, is more pronounced and promises the best separation on nanoscale chromatography platforms.

References

[1] Ehlert, S.; Rösler, T.; Tallarek U. *J. Sep. Sci.* **2008,** *31,* 1719-1728.

[2] Halász, I.; Martin, K. *Angew Chem. Int. Ed.* **1978**, *17,* 901-908.

[3] Kennedy, R. T.; Jorgenson, J. W. *Anal. Chem.* **1989**, *61,* 1128-1135.

[4] Hsieh, S.; Jorgenson, J.W. *Anal. Chem.* **1996***, 68,* 1212-1217.

[5] Ehlert, S.; Kraiczek, K.; Mora, J.-A.; Dittmann, M.; Rozing, G. P.; Tallarek, U. *Anal. Chem.* **2008**, *80*, 5945-5950.

[6] Guiochon, G. *J. Chromatogr. A* **2006**, *1126,* 6-49.

List of Publications

1.) S. Ehlert, U. Tallarek
High-pressure liquid chromatography in lab-on-a-chip devices.
Analytical and Bioanalytical Chemistry **2007**, *388*, 517-520.

2.) S. Ehlert, D. Hlushkou, U. Tallarek
Electrohydrodynamics around single ion-permselective glass beads fixed in a microfluidic device.
Microfluidics and Nanofluidics **2008**, *4*, 471-487.

3.) S. Ehlert, T. Rösler, U. Tallarek
Packing density of slurry-packed capillaries at low aspect ratios.
Journal of Separation Science **2008**, *31*, 1719-1728.

4.) S. Ehlert, K. Kraiczek, J.-A. Mora, M. Dittmann, G. P. Rozing, U. Tallarek
Separation efficiency of particle-packed HPLC microchips.
Analytical Chemistry **2008**, *80*, 5945-5950.

5.) S. Jung, S. Ehlert, J.-A. Mora, K. Kraiczek, M. Dittmann, G. P. Rozing, U. Tallarek
Packing density, permeability, and separation efficiency of packed microchips at different particle-aspect ratios.
Journal of Chromatography A **2009**, *1216*, 264-273.

6.) S. Khirevich, A. Höltzel, S. Ehlert, A. Seidel-Morgenstern, U. Tallarek
Large-scale simulation of flow and transport in reconstructed microchip packings.
Analytical Chemistry **2009**, *81*, 4937-4945.,

7.) S. Jung, A. Höltzel, S. Ehlert, J.-A. Mora, K. Kraiczek, M. Dittmann, G. P. Rozing, U. Tallarek
Impact of conduit geometry on the performance of typical particulate microchip packings.
Analytical Chemistry **2009**, *81*, 10193-10200.

8.) S. Jung, S. Ehlert, M. Pattky, U. Tallarek
Determination of the interparticle void volume in packed beds via intraparticle Donnan exclusion.
Journal of Chromatography A **2010**, *1217*, 696-704.

9.) S. Ehlert, L. Trojer, M. Vollmer, T. van de Goor, U. Tallarek
Performance of HPLC/MS microchips in isocratic and gradient elution modes.
Journal of Mass Spectrometry **2010**, *45*, 313-320.

10.) M. Trusch, S. Ehlert, A. Bertsch, O. Kohlbacher, D. Hildebrand, H. Schüter, U. Tallarek
Improved particle-packed HPLC/MS microchips for proteomic analysis.
Journal of Separation Science **2010**, accapted.